Fragmentation mechanisms in coaxial two-fluid atomization

Nathanaël Machicoane

Communauté
UNIVERSITÉ Grenoble Alpes

Mémoire

En vue d'obtenir l'HDR

HABILITATION À DIRIGER DES RECHERCHES

ÉCOLE DOCTORALE I-MEP2 - Ingénierie - Matériaux, Mécanique, Environnement, Energétique, Procédés, Production.

Arrêté ministériel : 23 novembre 1988

Présentée par

Nathanaël MACHICOANE

Chargé de Recherche de Classe Normale

UMR 5519 Laboratoire des Écoulements Géophysiques et Industriels, Université Grenoble Alpes - Grenoble INP - CNRS

Fragmentation mechanisms in coaxial two-fluid atomization

Travaux soutenus publiquement le **29/01/2024**,
devant le jury composé de:

Christophe Dumouchel, DR CNRS, CORIA
Rapporteur
Nicolas Rimbert, PR Univ. Lorraine, LEMTA
Rapporteur
Stéphane Zaleski, PR Sorbonne Université, D'Alembert
Rapporteur
Leonie Canet, PR UGA, LPMMC
Présidente du jury
François Gallaire, PR EPFL
Examinateur
Rui Ni, PR Johns Hopkins University
Examinateur
Jean-Philippe Matas, PR Univ. Lyon, LMFA
Examinateur

Contents

CHAPTER 1

Introduction

Motivation

The fragmentation of a liquid phase by a gas flow into a cloud of fine droplets (spray) is a highly complex multiscale and multiphysics problem (Fig. 1.1). Fragmentation is widely used in manufacturing (*e.g.,* spray coating, printing, cooling, cleaning), consumer products (*e.g.,* pharmaceutical, food processing, agricultural), fire safety, and space propulsion (Villermaux 2007). Fragmentation is also important in geological processes and in nature (Troitskaya et al. 2017; Veron 2015). For example, sea sprays contribute to sea-air exchanges, which need to be further understood for climate modeling. The current trial-and-error approaches used to characterize these applications fail at obtaining reliable correlations of spray parameters to injection parameters and must be replaced with physics-based methods. This is well illustrated by aircraft propulsion. The properties of the injected fluids vary with altitude, leading to changes in atomization regimes between take-off and cruising (Lasheras and Hopfinger 2000). This makes it challenging to identify the parameters that govern the physics of fragmentation, which are here also coupled to those of combustion. This has dramatic consequences such as a lack of reliability of engine restart in case of high-altitude failure, reduced fuel efficiency, and increased pollutant emissions.

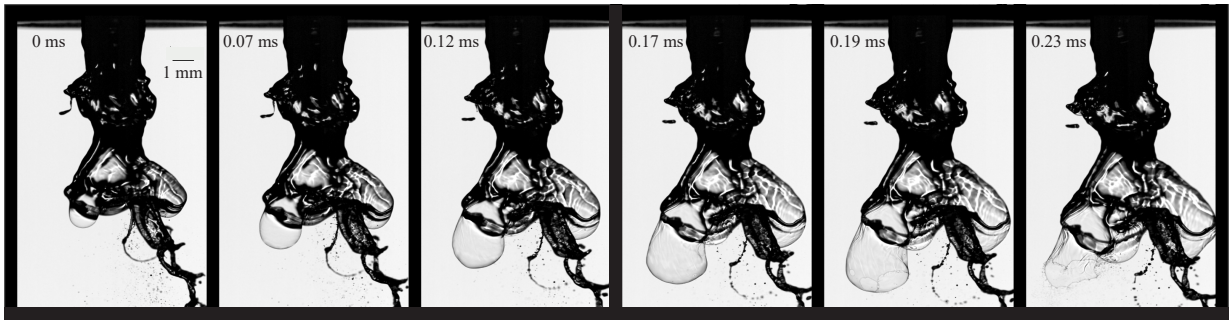

Figure 1.1: Selected snapshots from ultra-high-speed imaging (90 kHz) of the fragmentation of a round liquid jet by a coaxial annular gas jet. In this example, membranes, or bags, form and grow over times much longer (about 0.2 ms) than the time scale associated with their rupture (less than 0.01 ms). In comparison, other liquid structures do not move significantly in the successive images since transport happens over a much slower range of time scales (>1 ms here).

Additionally, the current strategies aimed at reducing emissions (retaining the European ACARE goals) come at the cost of decreased altitude relight capability and combustion stability, largely caused by a lack of detailed knowledge of the flow dynamics (Liu et al. 2017). Yet another illustration of the shortcomings of lack of knowledge of the detailed physics of fragmentation is found in spray cleaning. Spray cleaning is heavily relied upon in the electronic industry to produce microprocessors, as cleaning takes up to two-thirds of the manufacturing time (Snow, Sato, and Tanaka 2015). This field has mainly been addressed at the small scale by considering the impact of a "quantum" of liquid (*i.e.,* a single drop in the spray impact zone) by leveraging the extensive literature of drop impact (Josserand and Thoroddsen 2016). This descriptive framework is only suitable when successive impacts can be isolated, *i.e.,* when the characteristic time and length scales between two drops falling on the same surface are greater than the impact time and droplet size. However, a spray corresponds to a highly turbulent two-phase flow that is inherently multiscale (large liquid size polydispersity and wide velocity distributions). Hence, such "quantum" models do not adequately represent the flow resulting from the impact of a spray on a surface and fail at describing the complexity of the cleaning process (Lallart 2019).

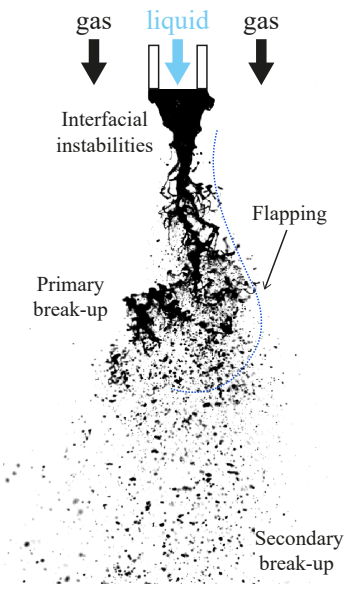

Figure 1.2: Illustration of several mechanisms in the fragmentation cascade, in the example of two-fluid coaxial atomization.

A two-fluid coaxial atomizer (Fig. 1.2) is frequently used to produce a high-quality spray. A round liquid jet is fragmented by an annular gas jet, in a process involving many subsequent mechanisms. A dense turbulent two-phase flow is observed in the region close to the atomizer exit (near-field), while a dispersed cloud of droplets is observed in the region far from the atomizer (far-field). The underlying mechanisms are highly coupled both between and within these two regions; each mechanism strongly affects the subsequent processes further downstream, forming a cascade. Currently, there is no predictive tool able to integrate all the different scales and to address the whole cascade of mechanisms involved in gas-assisted fragmentation. Models exist for isolated parts of this cascade such as jet instability close to the atomizer, the ensuing breakup mechanisms, and the size and velocity of the droplets in the far-field (Aliseda et al. 2008; Delon, Cartellier, and Matas 2018; Marmottant and Villermaux 2004; Singh et al. 2020; Varga, Lasheras, and Hopfinger 2003); however, these models tend to provide contradictory predictions because they do not account for the coupling of the underlying physics. Additionally, no characteristic length based on atomizer geometry and parameters exists to nondimensionalize the droplet size. This is a clear technological barrier for atomizer design and process optimization, as well as a limiting factor for spray modeling (Gorokhovski and Herrmann 2008).

A multiscale cascade of coupled physics

Figure 1.3 presents three coaxial atomization regimes and emphasizes the multiscale and multiphysics nature of this turbulent two-phase flow. In the near-field, the liquid jet can exhibit a large-scale meandering motion called flapping (Charalampous, Hardalupas, and Taylor 2009; Delon, Cartellier, and Matas 2018; Eroglu, Chigier, and Farago 1991; Kaczmarek et al. 2022; Kumar and Sahu 2020; Mayer and Branam 2004). At the small scale, the jet is destabilized due to instabilities at the gas-liquid interface (*e.g.,* Kelvin-Helmholtz, Rayleigh-Taylor, Marmottant and Villermaux 2004), which leads to the formation of liquid sheets, ligaments, and drops. Further breakup events, governed by the gas stresses acting on these liquid lumps and surface tension, yield droplets in the far-field that range in size from a few to a few hundred micrometers. Similarly, time scales range from a few hundred Hz to hundreds of kHz.

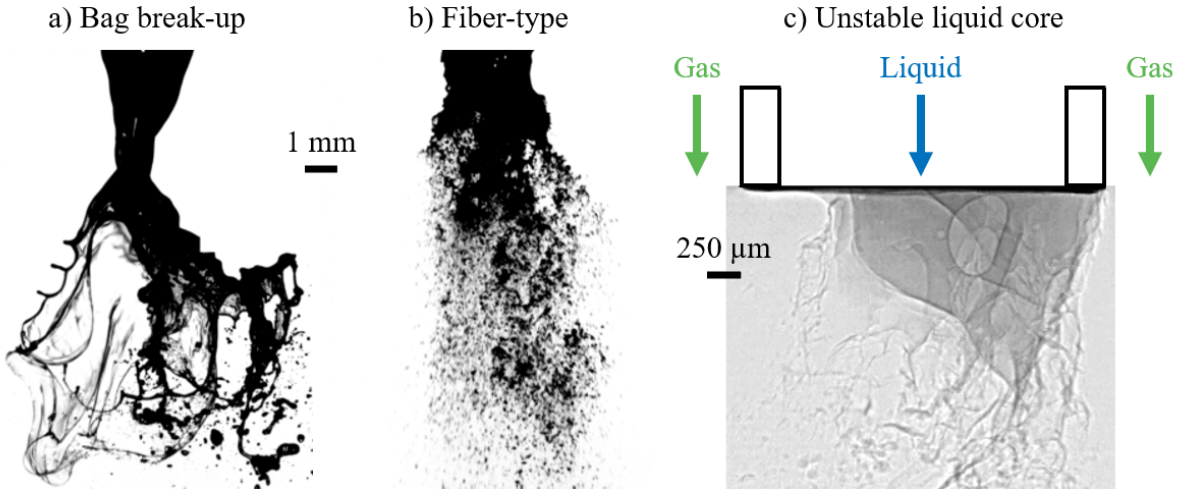

Figure 1.3: Near-field of a coaxial two-fluid atomizer. Images taken using visible light (a-b) and synchrotron X-ray (Machicoane et al. 2019) (c). a) At lower gas velocity, bag (also called membrane) breakup is observed. b) At higher gas velocity, fiber-type atomization occurs. c) At extreme atomization conditions, an unstable liquid core is observed.

Measurements in the far-field of the spray illustrate the coupled nature of the mechanisms involved in gas-assisted fragmentation. The far-field physics are intrinsically coupled to the physics of the near-field. At the large scale, inhomogeneities of the droplet cloud result from the flapping of the liquid jet in the near-field. At the small scale, the droplet size and spatiotemporal distributions change widely depending on atomization regimes. For example, bag breakup typically leads to the formation of both small droplets and large drops, while fiber-type atomization results primarily in small droplets. Additionally, in many applications, the far-field physics are coupled to other complex phenomena (*e.g.,* combustion in aircraft propulsion, evaporation/settling dynamics for airborne disease transmission).

Missing links in fragmentation

In many applications, spray parameters are simplified to only the final droplet size distributions in the far-field, ignoring the parameters in the near-field. Neglecting the near-field and other spray parameters typically leads to unreliable predictions/empirical correlations that relate droplet sizes to injection parameters. For example, the gas boundary layer thickness is proposed to be a determining factor for the droplet size in the far-field (Aliseda et al. 2008; Varga, Lasheras, and Hopfinger 2003); however, linear stability analyses indicate that the interfacial velocity is a better predictor of atomization regimes (Matas, Delon, and Cartellier 2018) but it has not been explored experimentally yet. In a recent study, (Ricard et al. 2021) showed that the changes from the bag breakup to fiber-type regimes may be deduced from changes in the scaling law of the velocity growth of the interfacial perturbations. There remains however a missing link between the studies concerning the near-field (*e.g.,* instabilities, liquid jet morphology, and length) and the far-field (droplet populations): the liquid inclusions (*e.g.,* sheets, ligaments, drops, and droplets) formed by the primary breakup events.

Spatiotemporal linear stability analyses also highlight competing types of instabilities (Matas, Delon, and Cartellier 2018): an absolute instability mediated by surface tension, another one caused by confinement, and a convective viscous shear instability. The wide changes in instability topologies between these regimes could potentially lead to drastic consequences on the whole cascade of mechanisms involved in fragmentation, but this competition remains largely unexplored. Measuring and characterizing the cascade of mechanisms involved in gas-assisted fragmentation is necessary to build prediction tools that reliably link spray parameters to injection parameters. Such tools require the establishment of accurate and quantitative regime maps of physical mechanisms, including the identification of their relevant non-dimensional groups. One can wonder what drives different types of instabilities to be dominant in different regions of the parameter space and how switching their type affects atomization regimes and associated scaling laws. Currently, the available models and predictions do not consider several important fundamental aspects of fragmentation, such as gas turbulence intensities. Varying turbulence intensity is expected to strongly change the spatial and temporal scales involved in the processes.

Role of gas turbulence

Planar two-phase mixing layer configurations (Fuster et al. 2013; Matas et al. 2015) are also used to unravel fragmentation processes emanating from large-scale instabilities of the liquid jet versus processes caused by interfacial instabilities. In this context, gas turbulence has been shown to strongly affect the interfacial instabilities: their frequency more than doubles when turbulence intensity is varied between 2 and 10% (Matas et al. 2015). However, the role of turbulent fluctuations in the remaining fragmentation processes remains unexplored in this ex-

periment. Recent numerical simulations at a moderate liquid-gas density ratio (Jiang and Ling 2021) confirm the effect of turbulent intensity on the primary instability, and extend the analysis to the secondary instability and breakup. In addition to higher longitudinal frequency, the transverse wave number increases with turbulent fluctuations, and a slight decrease in the probability of finding larger drops is found, with however a general decrease in the number of drops formed. While breakup is governed by the Weber number (*We*) comparing the aerodynamic to surface tension forces, its definition remains an open question. Basing aerodynamic forces on the mean versus fluctuating gas velocity can result in an order of magnitude difference in We, which could be the origin of the discrepancies in the literature. In a simplified geometry, (Kourmatzis and Masri 2015) showed the importance of accounting for both the turbulent Weber number and the gas turbulence intensity to build breakup models. Turbulence intensity remains uncharacterized in coaxial atomization configurations. Current scaling laws and models for fragmentation do not consider the turbulence intensity of the gas co-flow. This gap in understanding concerns both spray parameters such as droplet size distributions (Aliseda et al. 2008; Varga, Lasheras, and Hopfinger 2003) and larger-scale metrics such as the length of the liquid jet (Charalampous, Hadjiyiannis, and Hardalupas 2019; Kumar and Sahu 2018b; Machicoane et al. 2020).

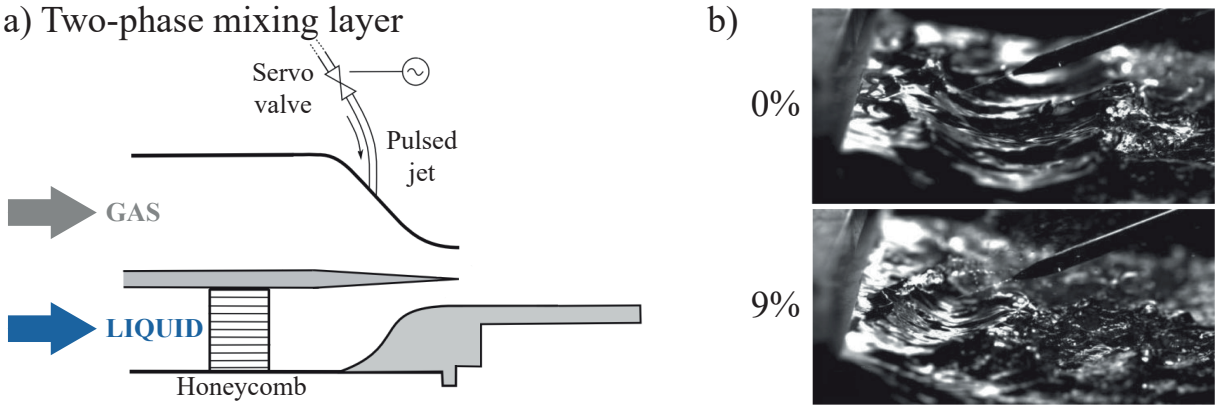

Figure 1.4: a) Schematics of the two-phase mixing layer at LEGI. b) Past study on this setup showing a decrease of the initial instability wavelength (through a frequency measurement) when the turbulence intensity is increased (root mean square over mean inlet velocity, expressed in %, other parameters are kept constant, from Matas et al. 2015). Blue lines highlight the wavelengths.

Fragmentation mechanisms at high gas turbulence intensities are expected to largely differ from the ones studied at low turbulence intensities. For instance, such differences were exhibited in the past when comparing fragmentation with and without angular momentum in the gas jet (swirl; Hopfinger and Lasheras 1996; Machicoane et al. 2020). Additionally, the strong effect of varying gas turbulence on interfacial instabilities was shown recently (Matas et al. 2015). However, liquid fragmentation under varying gas turbulence intensities has not been previously studied in realistic conditions.

Physics extraction and modeling

An additional goal of my research is to help the community advance high-fidelity numerical simulations of liquid fragmentation. These approaches can then further our understanding and help extract physics. Significant advances were made in high-fidelity numerical simulations of turbulent two-phase flows in recent years, such as high-accuracy phase tracking using Volume-of-Fluid methods (Ling et al. 2017; Owkes and Desjardins 2014). However, simulations cannot resolve every fragmentation process at the small scale and must resort to sub-grid models, which lack crucial experimental information. These models mishandle topology events whose thicknesses come close to the spatial resolution. While recently proposed thin-film models can support topologies below the mesh size, such as bags (also called membranes) in gas-assisted fragmentation (Chiodi 2020; Vu et al. 2023), their capability in producing droplets that are based on film physics and aerodynamic forces instead of numerical errors controlled by the mesh size remains to be established. There is also the question of hole formation (or nucleation) when a liquid sheet is stretched by the gas flow, and more generally of what controls the breakup of a liquid sheet by a turbulent gas flow. An example of the gain of using detailed experimental data to inform sub-grid models is found in the capture of contact line dynamics at the nozzle exit (Vu et al. 2023).

The processes of gas-assisted fragmentation found further downstream are likely to be tackled using reduced simulations since the cloud of droplets formed by the spray spreads out over a wide region and becomes too computationally demanding to simulate with high-fidelity approaches. For example, researchers have resorted to a conversion of the droplets into a collection of Lagrangian objects, which can be handled with less complexity using traditional particle tracking methods (Kim and Moin 2020; Ling, Zaleski, and Scardovelli 2015; Tomar et al. 2010).

CHAPTER 2

Fragmentation regimes

This chapter focuses on the spray formation mechanisms and only describes the near-field of two-fluid coaxial atomization. Work conducted on real-time feedback control of atomization (Osuna-Orozco et al. 2019, 2020), spray dispersion regimes (Huck et al. 2022), and electrostatically assisted two-fluid coaxial atomization (Osuna-Orozco et al. 2022) are described in more details in Osuna-Orozco 2021. Similarly, one can refer to Vu 2022 for joint numerical and experimental work on spray formation, highlighting several key mechanisms (Vu et al. 2023). Illustrative videos of every presented aspect can be found at http://www.legi.grenoble-inp.fr/people/Nathanael.Machicoane/research_videos.html

2.1 Motivations

The simplest fragmentation experiment consists of the discharge of a liquid jet from a circular orifice into an ambient atmosphere. Past a certain injection rate, a sustained water jet is observed, unlike dripping found at lower velocities (Clanet and Lasheras 1999), and the jet suffers from the well-known Rayleigh-Plateau instability. When the liquid jet velocity is further increased, the shear between the high-speed liquid and the stagnant ambient gas dominates the breakup, producing broader drop size distributions in what is referred to as the first wind-induced regime. At even higher velocities, the onset of turbulence in the liquid jet produces small-scale corrugations in the vicinity of the nozzle exit, and contributes together with the aerodynamic forces to fragmentation in the second wind-induced regime, before a transition to liquid atomization, where drops much smaller than the liquid jet diameter are peeled off the liquid jet and a spray is produced. When characterizing changes in fragmentation regimes as the liquid jet velocity increases, one can refer to a stability curve, shown in Fig. 2.1. The latter represents the evolution of the average length of the liquid jet until breakup with the velocity, along the various regimes. This length, sometimes called intact length or breakup length, is referred to here as liquid core length and represents the contiguous portion of the liquid jet, i.e. the length of the jet that is still connected to the nozzle. An exhaustive list of references concerning the subsequent regimes of the stability curve can be found in (Dumouchel 2008). The different regimes are characterized by different scalings for this length, which allows for clear quantitative distinctions. Note that the behavior in the liquid atomization regime, or pressure atomization, which is reached for large

values of the liquid velocity and injection pressure, is not sketched as it is out of the scope of this contribution. In this regime, the stability curve is heavily influenced by the geometry of the nozzle and its internal flow (e.g. level of turbulence and cavitation).

This section aims at applying to coaxial two-fluid atomization the concept of one or more stability curves from the fragmentation of a liquid jet into a still atmosphere. In the latter, alternatively known as gas-assisted atomization, the liquid jet fragmentation is due to a high-speed annular gas jet that surrounds the liquid. Coaxial atomization also presents several breakup regimes (Chigier and Farago 1992; Lasheras and Hopfinger 2000), which, when reported in a liquid Reynolds number and gas Weber number parameter space, partly overlap with the stability curve of pressure atomization (Fig. 2.2). The gas Weber number is defined here to compare the liquid jet's surface tension force d_l/σ, where d_l is the liquid nozzle inner diameter and σ the surface tension, to the gas jet aerodynamic stresses $\rho_g U_g^2$, where ρ_g is the gas density and U_g the average exit velocity of the gas jet. For low enough liquid Reynolds number (laminar liquid injection), at zero gas velocity, Rayleigh-Plateau breakup is observed. When the gas velocity increases, breakup is almost identical but the axisymmetry is lost, giving the name to the non-axisymmetric Rayleigh-Plateau breakup regime. This is followed by the shear breakup regime, where the velocity difference between the gas and liquid phase gives rise to a meandering motion of the liquid jet called flapping (Charalampous, Hardalupas, and Taylor 2009; Delon, Cartellier, and Matas 2018; Eroglu, Chigier, and Farago 1991; Juniper and Candel 2003; Kaczmarek et al. 2022; Mayer and Branam 2004), which dominates breakup here. The liquid jet is bent in arcs that stretch and form long and thin ligaments that exhibit capillary instabilities. At higher gas Weber numbers, the gas can flatten the liquid jet, especially in transverse portions created by the bends, and stretch the liquid into thin membranes called bags. This type of shear breakup is hence referred to as bag breakup, and produces very small droplets issued from the membranes, while the bags' rims fragment into larger drops. A further increase of the gas Weber number gives rise to a succession of Kelvin-Helmholtz and Rayleigh-Taylor instabilities at the gas-liquid interface (Aliseda et al. 2008; Marmottant and Villermaux 2004; Matas, Delon, and Cartellier 2018; Varga, Lasheras, and Hopfinger 2003), forming ligaments that are stripped from the liquid jet. This produces very small droplets and is referred to as the fiber-type atomization regime.

Among these regimes, atomization is typically defined as conditions where the most probable droplets formed are much smaller than the liquid jet diameter (*e.g.,* 50 μm or less for a millimetric jet), and where such droplets are at least partially produced close to the atomizer exit from primary breakup events (directly issued from the liquid jet). This is the case in the membrane breakup and fiber-type atomization regimes. For these conditions, the liquid core length has been studied in depth, starting in the early 1990s' (Eroglu, Chigier, and Farago 1991). However, as can be seen in comprehensive studies spanning a wide range of operating parameters (Leroux, Delabroy, and Lacas 2007), no effect from the change in atomization regimes is displayed on the liquid core length: the average value presents a monotonic decrease, with a constant power law of exponent around -0.3 with respect to the gas-to-liquid dynamic pressure ratio M (Ku-

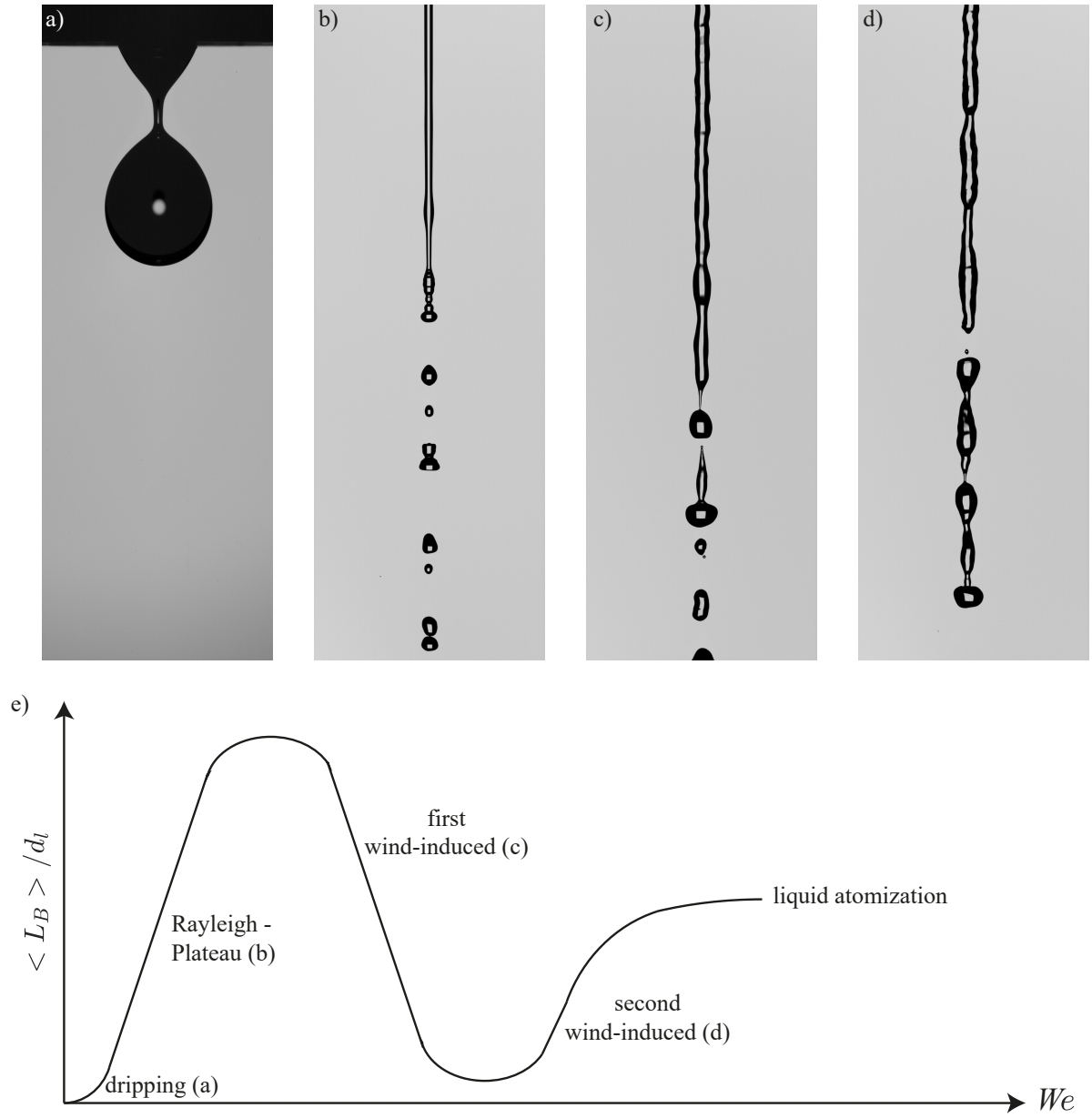

Figure 2.1: Visualizations of the fragmentation of a liquid jet discharged into a stagnant gas in the dripping (a), Rayleigh-Plateau (b), first wind-induced (c), and second wind-induced (d) regimes. e) Schematic stability curve relating the average liquid core length $\langle L_B \rangle$ to the Weber number *We*, increased from (a) to (d) by increasing the liquid flow rate here. d_l corresponds to the liquid nozzle's inner diameter.

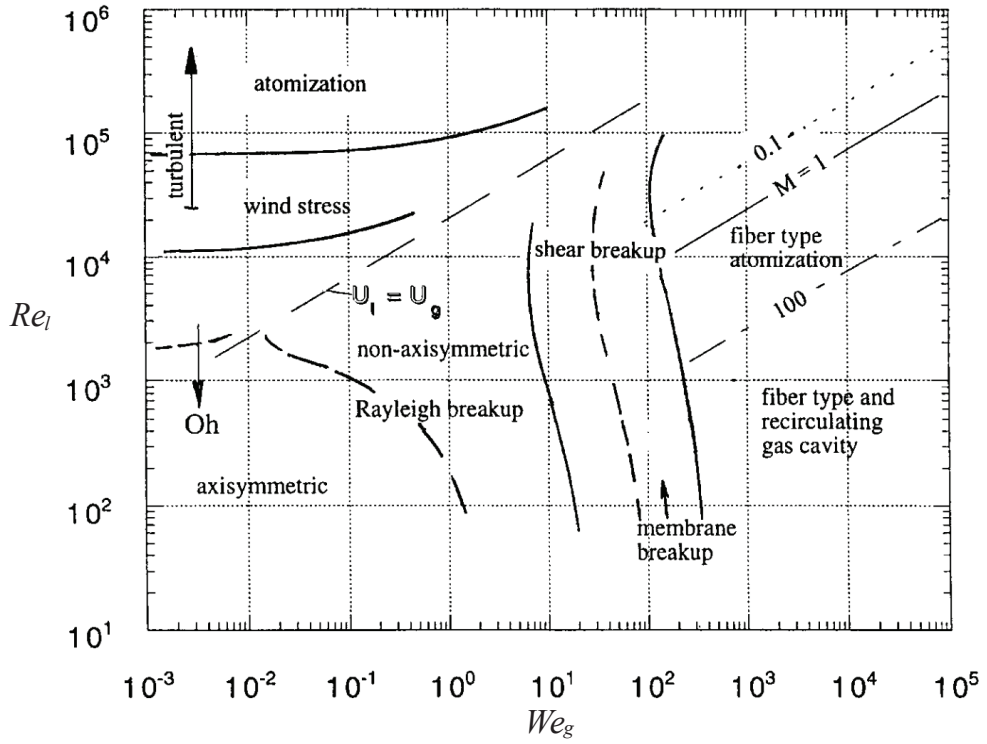

Figure 2.2: Regime map of atomization regimes extracted and modified from Lasheras and Hopfinger 2000. $Re_l = U_l d_l/\nu_l$ and $We_g = \rho_g U_g^2 d_l/\sigma$ respectively denote the liquid Reynolds number and the gas Weber number; $M = \rho_g U_g^2/\rho_l U_l^2$ is the gas-to-liquid dynamic pressure ratio; ν_l, ρ_l, and U_g are the liquid kinematic viscosity, density, and average exit velocity.

mar and Sahu 2020; Leroux, Delabroy, and Lacas 2007; Zhao et al. 2014). The latter is defined as $M = \rho_g U_g^2/\rho_l U_l^2$, where ρ_l is the liquid density, and has been shown to control the average liquid core length. Recent work has focused on a deeper analysis of the liquid core length, encompassing its statistics and temporal dynamics (Charalampous, Hadjiyiannis, and Hardalupas 2019; Fong et al. 2022; Kumar and Sahu 2018a; Machicoane et al. 2020; Singh et al. 2021). The goal of this section is to leverage these approaches to develop a quantitative framework that identifies the signature of changes in coaxial atomization regimes. Such changes play key roles in the droplet size distributions and in the spray dispersion regimes further downstream (Huck et al. 2022).

More details on the work presented here can be found in Kaczmarek et al. 2022; Machicoane, Osuna-Orozco, and Aliseda 2023; Ricard et al. 2021; Tolfts, Deplus, and Machicoane 2023.

2.2 Experimental setup and methods

2.2.1 A canonical two-fluid coaxial atomizer

The experimental setup consists of a canonical two-fluid coaxial atomizer, shown in Fig. 2.3 (more details on the open-source geometry is given in Machicoane et al. 2019). The liquid nozzle is 100 mm long, with an inner diameter $d_l = 1.98$ mm and an outer diameter $D_l = 3.1$ mm. This geometry ensures a Poiseuille flow is fully established before the liquid exits the nozzle when operated in laminar conditions, while a fully-developed plug flow is expected in turbulent conditions. The liquid nozzle is placed at the center of the gas nozzle. The outer wall of the liquid nozzle and the inner wall of the gas nozzle form a cavity that channels the gas into an annular exit plane with an inner diameter D_l and an outer diameter $d_g = 9.985$ mm. Note that d_l, D_l, and d_g are measured with the same accuracy of 1 μm. Both of these walls present a cubic-spline shape ensuring the gas flow is longitudinal when it exits the nozzle. The working fluids are air and water at 25 °C.

The volumetric flow rates of the gas and the liquid, respectively noted Q_g and Q_l, are monitored by flowmeters. A pressurized tank is used to produce the liquid flow. The tank's pressure is regulated to limit the fluctuations in the flow rate. The uncertainty of the liquid flow rate is given by the uncertainty of the associated flowmeter $\Delta Q_l = 0.06$ L/min. Compressed air is used for the gas flow, with a pressure regulator set below the compressor's low-pressure point to ensure a steady gas flow. The uncertainty of the gas flow is dominated by the small variations caused by the feedback control loop that fixes the gas flow rate. This uncertainty, much larger than the flowmeter uncertainty, is calculated for each run and is typically of order $\Delta Q_g = 2.5$ L/min.

We define the gas and liquid mean velocities at the exit plane respectively as $U_g = \frac{Q_g}{A_g}$ and $U_l = \frac{Q_l}{A_l}$, with $A_l = \pi \frac{d_l^2}{4}$ the liquid section and $A_g = \frac{\pi}{4}(d_g^2 - D_l^2)$ the gas section. The liquid Reynolds number $Re_l = \frac{U_l d_l}{\nu_l}$, where ν_l is the kinematic viscosity of water, is varied from 730 to 20 000, encompassing the transition from a laminar to a turbulent exiting liquid jet. The gas Reynolds number $Re_g = \frac{2Q_g}{\sqrt{\pi A_g}\nu_g}$, with ν_g the kinematic viscosity of air, ranges from 10^4 to 10^5.

The Weber number based on the gas velocity and on the liquid inner diameter $We_g = \frac{\rho_g U_g^2 d_l}{\sigma}$ ranges from 14 to 950. Note that with the gas density ρ_g and surface tension coefficient σ being fixed, the gas Weber number and gas Reynolds number can be used equivalently to describe changes in gas velocity. Alternatively, when defined based on a slip velocity between each phase, the Weber number $We_r = \frac{\rho_g (U_g - U_l)^2 d_l}{\sigma}$ range becomes $11 \leq We_r \leq 940$. An important dimensionless parameter for the liquid core length is the gas-to-liquid dynamic pressure ratio (also called

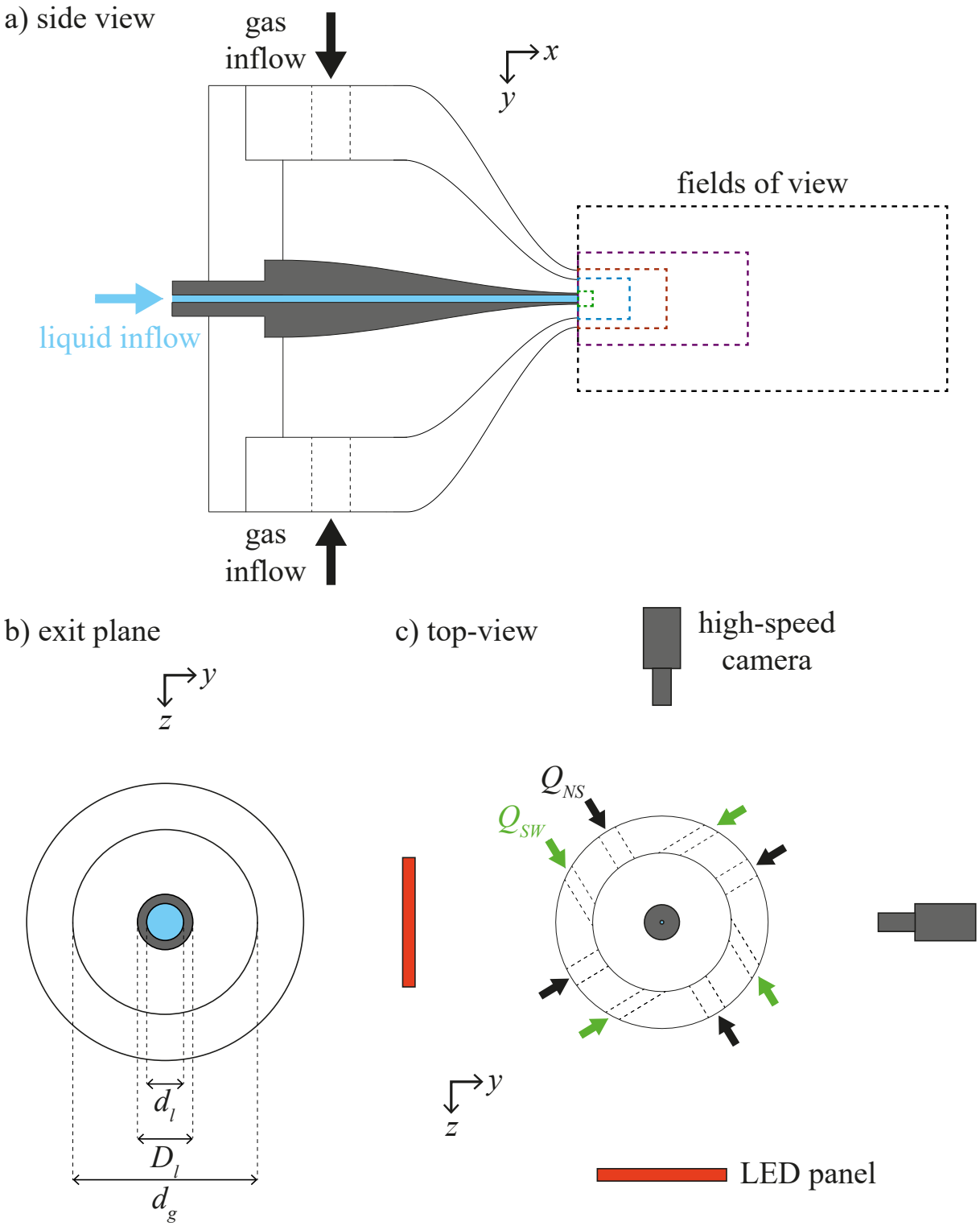

Figure 2.3: Schematic views of the atomizer: a) Longitudinal cut, b) transverse cut at the exit plane, and c) transverse cut at the gas inlet plane. The various sizes of the fields of view used for back-lit imaging are displayed in a) and the arrangement for two orthogonal cameras is shown in c).

U_l (m/s)	U_g (m/s)	M	Re_l	Re_g	m	We_g
10	41.9	**0.019**	20 000	26 000	0.34	53
0.39	177	**230**	730	110 000	0.0031	950
0.39	113	94	**730**	71 000	0.0048	390
11	113	0.13	**20 000**	71 000	0.13	390
2.3	20.9	0.095	4 300	**13 000**	0.15	14
1.6	177	13.3	3 000	**111 000**	0.013	950

Table 2.1: Sample from the 93 investigated operating conditions (reported in the first four subsections of Sec. 2.3), with their corresponding dimensionless parameters. The maximum and minimum values of the gas-to-liquid dynamic pressure ratio $M = \frac{\rho_g U_g^2}{\rho_l U_l^2}$, the liquid Reynolds number $Re_l = \frac{U_l d_l}{\nu_l}$, and the gas Reynolds number $Re_g = \frac{4Q_g}{\sqrt{4\pi A_g}\nu_g}$ are highlighted in bold. $m = \frac{\rho_l U_l A_l}{\rho_g U_g A_g}$ represents the liquid mass loading and $We_g = \frac{\rho_g U_g^2 d_l}{\sigma}$ the Weber number based on the liquid diameter.

gas-to-liquid momentum ratio) $M = \frac{\rho_g U_g^2}{\rho_l U_l^2}$, where ρ_l is the density of the liquid phase. The dynamic pressure ratio varies by over 4 orders of magnitude, from 0.02 to 230. The extrema of the investigated parameter space are summarized in Table 2.1.

Note that Q_g denotes the total gas flow rate, that can be introduced into the nozzle from both on-axis inlet and off-axis inlets (Fig. 2.3c). When all the gas flows through the on-axis inlets, the gas jet is longitudinal, while diverting some flow rate into the off-axis inlets produces angular momentum in the gas jet, called swirl. The additional parameter to characterize swirl is the swirl ratio $SR = Q_{SW}/Q_{NS}$, where Q_{SW} and Q_{NS} are the flow rates going through the on-axis and off-axis inlets respectively. While SR was varied from 0 to 1 in the studies that were conducted, this manuscript mostly considers cases without swirl, with the exception of a few sections where swirl is used to demonstrate the variability of a phenomenon with it.

2.2.2 High-speed back-lit imaging

We use back-lit imaging with a high-speed camera to measure the dynamics of the liquid jet breakup. The imaging parameters are adapted to the temporal and spatial scales of the spray formation mechanisms that vary on the considered parameter space. The frame rate used ranges from a few thousand Hz to 35 000 Hz and the imaging dimension varies from 5 mm^2 to 100 mm^2. As the highest frame rates require reducing the number of pixels used, maintaining the targeted physical size of the imaging window is attained by lowering the magnification. The resulting spatial resolutions hence vary from 5 to 90 μm/pixels. Each movie contains at least 10^4 frames, corresponding to 0.3 - 0.8 s depending on the frame rate, ensuring each acqui-

sition is longer than a hundred times the timescale associated with the liquid jet length variations.

The image processing aims at measuring the liquid core length and motion. Each frame goes through a normalization process, which consists in subtracting a reference background and then dividing by the reference background. The images are then binarized using thresholding to detect the liquid core. More details on image processing can be found in Machicoane et al. 2020.

2.3 Liquid core length

As the liquid jet is fragmented by the gas jet, a portion of it remains hydraulically connected to the liquid nozzle, which will be termed the **liquid core**, while the rest of the liquid phase is broken off this core and forms ligaments, sheets, drops, and other blobs of liquid. The liquid core length is equal to the longitudinal extent of the liquid core, *i.e.,* how far downstream the liquid core reaches (and is not a measure of its bending or tortuosity). When using high-speed back-lit imaging, L_B is measured on each binarized image as the longitudinal extent of the detected liquid core. Time series are produced, and one can study the statistics (using moments and probability density functions) and the temporal dynamics (using auto-correlation functions).

2.3.1 Scaling laws of the first two statistical moments

Figure 2.4 shows the average and the standard deviation of the liquid core length normalized by the inner liquid diameter, $< L_B > /d_l$ and $L_{B,STD}/d_l$, both as a function of the gas-to-liquid dynamic pressure ratio M. In both cases, the data collapse onto a master curve. We perform power-law fits, represented by the red curve in each plot, and find them to be in good agreement with the experimental data. The prefactor and exponent obtained when fitting the normalized average liquid core length by a power-law AM^n are respectively $A_{avg} = 12.8 \pm 0.8$ and $n_{avg} = -0.34 \pm 0.04$. This is consistent with previous results from the literature. Leroux, Delabroy, and Lacas 2007 showed that $< L_B >$ scales with $M^{-0.3}$ on a different range of liquid Reynolds number $45 < Re_l < 300$ and for a wide range of gas-to-liquid dynamic pressure ratio $0.2 < M < 1000$, obtained by changing the density of the liquid. They report a prefactor $A_{Leroux} = 10$. Kumar and Sahu 2020; Zhao et al. 2014 showed that $< L_B >$ also depends on the geometry of the nozzle, explaining the difference in terms of prefactor. The exponents they report are also in good agreement with the value found here.

The scaling of the standard deviation of the liquid core length with M was not reported before. The prefactor and exponent obtained when performing a power-law fit on $L_{B,STD}/d_l$ are respectively $A_{STD} = 2.14 \pm 0.12$ and $n_{STD} = -0.30 \pm 0.03$. The scalings of the average and

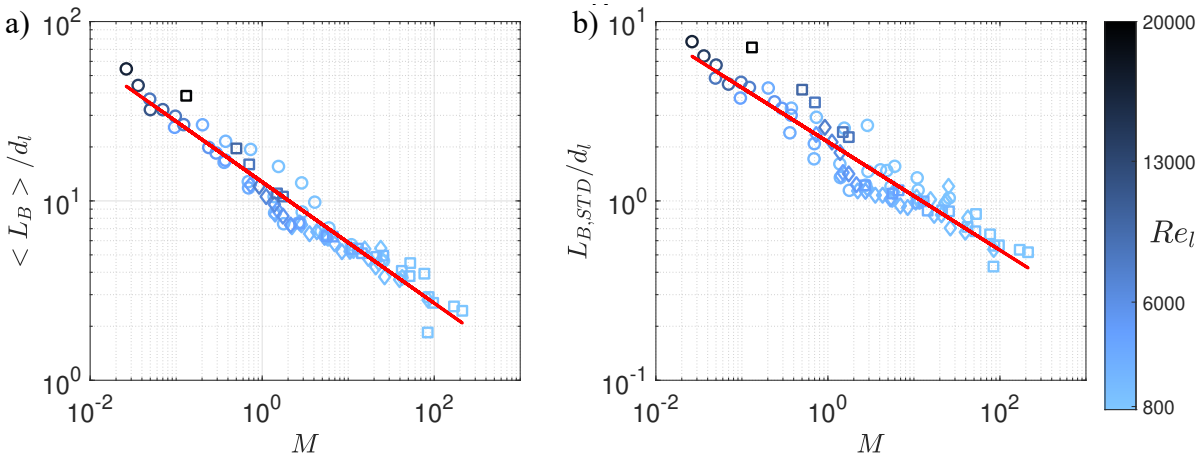

Figure 2.4: Average (a) and standard deviation (b) of the liquid core length normalized by the inner liquid diameter d_l as a function of the gas-to-liquid dynamic pressure ratio M. Membrane breakup, fiber-type atomization, and transitional regimes are represented using circles, squares, and diamonds respectively. Power law fits AM^n are shown in solid red line with A: $A_{avg} = 12.8 \pm 0.8$ and $n_{avg} = -0.34 \pm 0.04$; B: $A_{STD} = 2.14 \pm 0.12$ and $n_{STD} = -0.30 \pm 0.03$.

standard deviation with M are almost identical, only the prefactor of the power-laws are different.

For both plots of Fig. 2.4, the membrane breakup and fiber-type atomization regimes are represented with circles and squares respectively. In addition, diamonds are used for conditions where both membrane formation and fiber-type atomization coexist. The liquid Reynolds number is also indicated with the color bar. No influence of atomization regimes or of Re_l is exhibited in the current dataset. The gas-to-liquid dynamic pressure ratio M is enough to capture variations of the liquid Reynolds number with a single power law, both for the average and standard deviation of the liquid core length L_B. M hence appears to be the sole parameter controlling the first two moments of L_B. In addition, with almost equal power law exponents $n_{avg} \simeq n_{std}$, the ratio of the standard deviation to average liquid core length if found to be constant, and function of no physical quantity, over the range of parameter space explored. This means that the fluctuations of the liquid core can just be approximated by its mean value, as $L_{B,STD} \simeq 0.18 \langle L_B \rangle$

2.3.2 Statistical study

To further investigate the general shape of the probability density function of the liquid core length we use the normalized and centered variable: $\tilde{L}_B = \frac{L_B - \langle L_B \rangle}{L_{B,STD}}$. Figure 2.5a) displays the probability density functions of $\tilde{L}_B$ for every experimental conditions, showing a remarkable collapse. The black curve is a normalized and centered skew-Gaussian function, whose general expression is given in Eq. 2.1. It is solely defined by α, ω, and ξ, the shape, scale, and location

parameters respectively. The expression of the skew-Gaussian distribution is simplified in the case of a centered and normalized distribution where $\mu = 0$ and $\sigma = 1$: the shape, scale, and location parameters depend only on one parameter, the skewness, directly measured from the data. In the case of the black curve in Fig. 2.5a), this parameter is taken as the average of the skewness value of each condition.

$$f(x) = \frac{e^{-\frac{1}{2}\left(\frac{x-\xi}{\omega}\right)^2}}{\omega\sqrt{2\pi}}\left[1+\text{erf}\left(\frac{\alpha(x-\xi)}{\sqrt{2}\omega}\right)\right] \tag{2.1}$$

$$\alpha = \left(\frac{2}{\pi}\left[1+\left(\frac{4-\pi}{2\beta}\right)^{2/3}\right]-1\right)^{-1/2} \tag{2.2}$$

$$\omega = \frac{\sigma}{\sqrt{1-\frac{2\delta^2}{\pi}}} \tag{2.3}$$

$$\xi = \mu - \omega\delta\sqrt{\frac{2}{\pi}} \tag{2.4}$$

where erf is the error function, $\delta = \frac{\alpha}{\sqrt{1+\alpha^2}}$, and μ, σ, and β are respectively the average, standard deviation, and skewness.

The skew-Gaussian is in good agreement with the experimental data, confirming previous observations done in a narrower range of operating conditions Kaczmarek et al. 2022. Despite an apparent collapse of the curves around the average distribution (black line), close examination shows that the shape of the probability density function appears to vary slightly with the gas Reynolds number, as highlighted by the color bar. The latter emphasizes (in green) conditions for $Re_g > 33\,000$, which appear to collapse onto a master curve, while conditions of lower gas Reynolds number values behave differently. Note that in the current study, since changes in non-dimensional groups only occur through changes in mean exit velocities (U_l and U_g), this transition, occurring around $U_g = 53$ m/s, is reported above in terms of gas Reynolds number for simplicity (since $Re_g \sim U_g$) but it can also be expressed with the gas Weber number with $We_g = 75$ and both threshold values will be used hereafter. To further understand these differences in shape we show in Fig. 2.5b) the skewness of the liquid core length as a function of Re_g. The skewness tends to be lower when $Re_g < 33\,000$ and shows an increasing trend although the spread is important. Focusing on the conditions with $Re_g > 33\,000$, we compute their average skewness, $< \beta_{L_B} >= 0.46$, and associated standard deviation, $\beta_{L_B,STD} = 0.07$. The dashed line corresponds to $< \beta_{L_B} >$ and the dashed-dotted lines to $< \beta_{L_B} > \pm \beta_{L_B,STD}$. Despite a moderate spread still present above the transition, most of the data points are found to be less than a standard deviation (of the skewness) away from the average skewness. This indicates that the skewness increases with Re_g up to an asymptotic value at high gas Reynolds number, with no further dependency on other dimensionless parameters. Since the probability density functions collapse at high Reynolds numbers, higher-order statistical moments are not investigated.

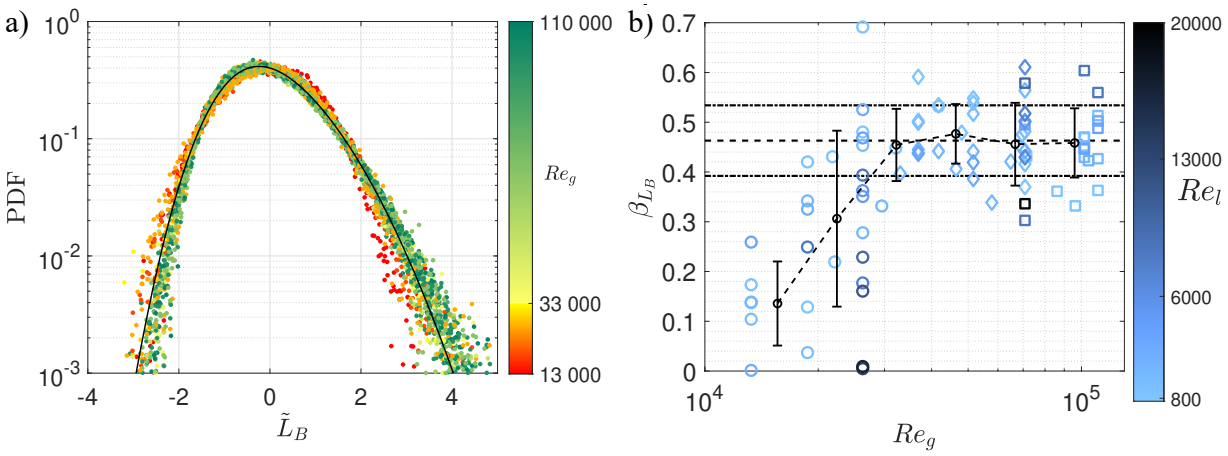

Figure 2.5: a) Probability density functions of the centered and normalized liquid core length $\tilde{L}_B = \frac{L_B - \langle L_B \rangle}{L_{B,STD}}$ for every operating condition. The black curve corresponds to a skew-Gaussian function with zero average, unit standard deviation, and whose skewness is computed by averaging the skewness obtained for every experimental condition. b) Skewness of the liquid core length as a function of the gas Reynolds number Re_g. For conditions with $Re_g > 33\,000$, alternatively $We_g = 75$, we compute the average skewness $< \beta_{L_B} >= 0.46$ and the standard deviation of the skewness, $\beta_{L_B,STD} = 0.07$. The dashed line corresponds to $< \beta_{L_B} >$ and the dashed-dotted line to $< \beta_{L_B} > \pm \beta_{L_B,STD}$. The x-axes are divided into bins to compute averages and standard deviations of β_{L_B} to form box-and-whisker plots. Membrane breakup, fiber-type atomization, and transitional regimes are represented using circles, squares, and diamonds respectively.

2.3.3 Temporal dynamics

Figure 2.6 shows the auto-correlation functions obtained for each condition as a function of the normalized time-lag τ/τ_c. The correlation time τ_c is obtained by an integration of the auto-correlation function up to reaching 75% decorrelation (see Machicoane et al. 2020). The color bar highlights in red and green the conditions with low and high gas velocities respectively. The solid black curve of Fig. 2.6b) corresponds to the exponential function $\exp\left(-\frac{\tau}{1.33\tau_c}\right)$ and captures the auto-correlation functions for conditions with low gas velocities (Re_g in the vicinity of 15 000, alternatively $We_g \sim 20$). The coefficient 1.33 comes from the computation of τ_c: the time defined by the integral of a decreasing exponential function up to the crossing of 0.25 is equal to 1.33 times its exponential decay rate. Auto-correlation functions for conditions at higher gas velocities are found to initially decrease faster than an exponential function, and the initial decrease rate appears to be an increasing function of Re_g in the intermediate range of gas velocities (orange to yellow symbols). This is visible by the initial ordering of the curves (for $\tau/\tau_c < 1$) where increases of Re_g (red to orange to green) yield a given decorrelation over shorter time periods. For $Re_g > 33\,000$, the rate seems to reach an asymptotic value and all functions (green symbols) collapse onto a master curve. The change of shape of the auto-correlation functions

of the liquid core length also highlights the transition discussed in the previous section for the distributions of L_B (around a transition value of $Re_g = 33\,000$ or $We_g = 75$): conditions at low gas velocity are exponentially decreasing, and increases of U_g yield faster-decreasing functions, until reaching a constant decay rate after the transition, when represented along the normalized time lag τ/τ_c.

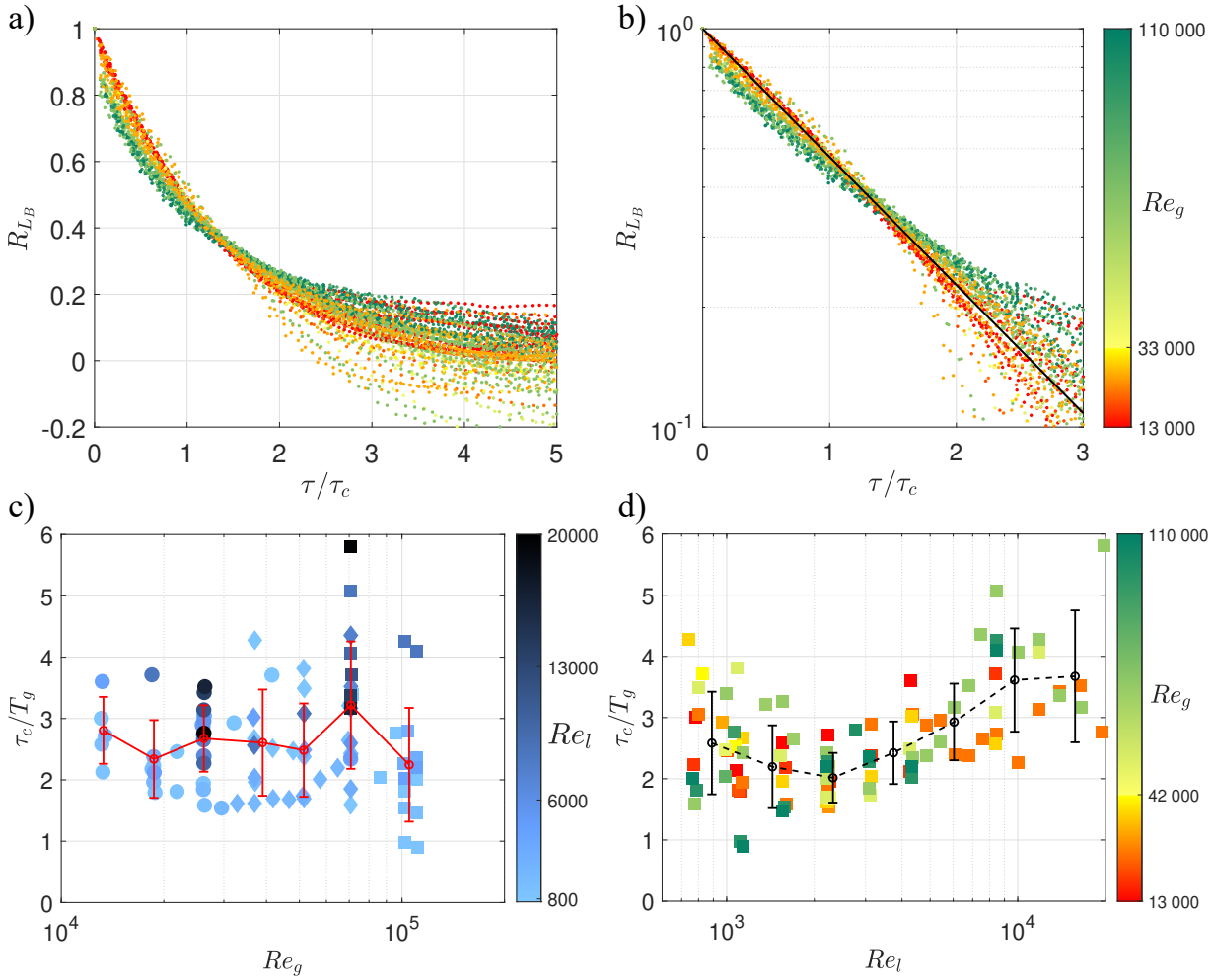

Figure 2.6: Auto-correlation functions of L_B as a function of the normalized time lag $\frac{\tau}{\tau_c}$. a): linear ordinate. b): logarithmic ordinate. The black curve corresponds to $\exp\left(-\frac{\tau}{1.33\tau_c}\right)$.) Correlation time τ_c normalized by the timescale of the gas jet T_g as a function of Re_g (c) and Re_l (d). The x-axes are divided into bins to compute averages and standard deviations of $\frac{\tau_c}{T_g}$ to form box-and-whisker plots.

To characterize the evolution of the correlation time τ_c, we introduce a large-scale timescale of the gas jet $T_g = \frac{d_g}{U_g} \propto Re_g^{-1}$. Figure 2.6c) shows the correlation time normalized by the gas jet timescale $\frac{\tau_c}{T_g}$ as a function of the gas Reynolds number. We divide the range of gas Reynolds

number into 7 bins and compute the average and standard deviation of $\frac{\tau_c}{T_g}$ in each of these bins. The red dots correspond to the average and the errorbars to twice the standard deviation. Despite some spread, the average values do not appear to depend on the gas Reynolds number, when normalized by T_g. This shows that the correlation time τ_c scales with Re_g^{-1}, with a proportionality coefficient of approximately 16.3 s.

Figure 2.6d) shows the correlation time normalized by the timescale of the gas jet $\frac{\tau_c}{T_g}$ as a function of the liquid Reynolds number. We divide the range of Re_l into 7 bins and compute the average and standard deviation of $\frac{\tau_c}{T_g}$ in each of these bins. The black dots correspond to the average and the errorbars to twice the standard deviation. The normalized average values appear constant at lower liquid Reynolds number values and find higher values in the range of high Re_l (where a growing or constant trend remains indefinite with the current range explored). We compute the average and standard deviation for all conditions with $Re_l < 4000$ and find $\frac{\tau_c}{T_g} = 2.3 \pm 0.7$, while $Re_l > 8000$ yields $\frac{\tau_c}{T_g} = 3.6 \pm .9$. The change between both behaviors being gradual along Re_l and moderate in amplitude, we cannot establish a clear threshold value of liquid Reynolds number for this transition. The averaged trend highlighted by the black dashed line shows an increase starting between $Re_l = 2000$ and 4000, which may reach an asymptotic value for $Re_l \geq 10000$.

We suspect that the change of behavior of the correlation time is related to the transition to a turbulent state of the liquid jet. Confirming this however would require velocity measurements within the liquid jet, which are challenging to implement in such setup. Lacking a clear quantitative indicator of the transition to turbulence of the liquid jet, we turn to the qualitative visualization of the liquid jet interface, as an indirect proxy to the measure of the agitation in the liquid jet. Figure 2.7a) shows the liquid jet exiting the nozzle with no added gas flow. In the vicinity of the nozzle exit (i. e. at longitudinal x far from the region where the breakup due to the Rayleigh-Plateau instability occurs) the interface of the liquid jet remains undisturbed for $Re_l = 2000$. We interpret this as a laminar liquid jet exiting the nozzle. The gas-liquid interface becomes slightly disturbed when $Re_l = 4000$, with localized corrugations of approximately the same size. These disturbances are a signature of a deviation from a fully laminar state of the liquid jet, translating for instance the presence of turbulence spots. The situation is much different at $Re_l = 8000$, as the jet is heavily disturbed by corrugations of a broad range of scales, right from the nozzle exit, a clear signature of a turbulent liquid jet. These visualizations strongly suggest that the departure from a laminar jet occurs for a value of the liquid Reynolds number found between these two bounds $2000 < Re_l < 4000$, and would be the cause of the change of behavior of the liquid core length timescale. In addition, when an established turbulent state is reached so that disturbances of various sizes are observed over the whole jet, i. e. in the vicinity of $Re_l = 8000$, the increase of τ_c/T_g with Re_l is seen to either saturate or become less steep (Fig. 2.6c). Nevertheless, this change of regime with Re_l does not influence the moments of the probability density function. In the range currently explored, the effect of the onset of turbulence in the liquid jet seems to be limited to a secondary effect on the value of the correlation time.

2.3.4 Onset of fiber-type atomization

For low values of Re_g, small values of β_{L_B} are systematically found, while close to the transition, values can be found anywhere between 0 and approximately 0.5. On the contrary, for high gas Reynolds numbers, most of the values of the skewness are found within one $\beta_{L_B,STD}$ of the asymptotic value $\langle\beta_{L_B}\rangle$. In opposition to the skewness, the auto-correlation functions of L_B are very well converged in the range of short time lags. The high-speed imaging measurements besides well resolve that range so that even slight changes in function shape can be interpreted. Both auto-correlation functions and statistical distributions of L_B show very similar behaviors in the evolution of their shape. Starting from a decreasing exponential function at low gas Reynolds number (highlighted by the dashed line representing $\exp\left(-\frac{\tau}{1.33\tau_c}\right)$), the decay rate increases slightly with Re_g (i. e. auto-correlation functions decreasing faster than an exponential) until reaching a master curve for conditions with $Re_g > 33\,000$. We conclude that the reported transition separates two regimes: i) for $Re_g < 33\,000$, the liquid core length presents correlations and statistics with a lower decay rate and skewness than at higher gas Reynolds number, and ii) for $Re_g > 33\,000$, the statistics of L_B are described by a constant skewness while presenting correlations that decrease faster than an exponential with a fixed decay rate. With the constant ratio of the standard deviation to the average liquid core length, the statistics of L_B are described by a single parameter in the second regime, and hence solely driven by M.

The transition between two regimes for the distributions and auto-correlation functions of L_B below and above the value of $Re_g = 33\,000$ (alternatively $We_g = 75$) is an unexpected finding, especially considering the reported behaviors of $< L_B >$, $L_{B,STD}$ and τ_c, each showing a single scaling with respect to a sole non-dimensional parameter (respectively M and Re_g) over the whole range of parameters explored. A possible origin for this transition could be a change in the behavior of the gas jet. Dimotakis 2000 showed that a turbulent round jet exhibits a mixing transition when the gas Reynolds number is around $Re_g \approx 10^4$. Beyond this transition, the gas jet efficiently entrains the surrounding fluid around it (ambient air in our case) and the jet's turbulent properties become drastically different. The instabilities of the liquid jet's interface originate from interactions with the turbulent gas jet surrounding it. For instance, Matas et al. 2015 showed that increasing the gas turbulence intensity leads to interfacial instabilities presenting higher frequencies, in a planar configuration. In the same configuration, high-fidelity simulations also show faster growth and destabilization of the instabilities when the gas turbulence is increased (Jiang et al. 2019). These interactions are thus expected to differ below and above the mixing transition of the gas jet, which in turn can be expected to play a role in the liquid core length. However, this idea would need further exploration of the parameter space and thorough characterization of the gas jet to accurately define the mixing transition here. A better candidate to explain the change of behavior of L_B stems from the change in atomization regimes (whose potential link to changes in the gas jet behavior could prove to be interesting work).

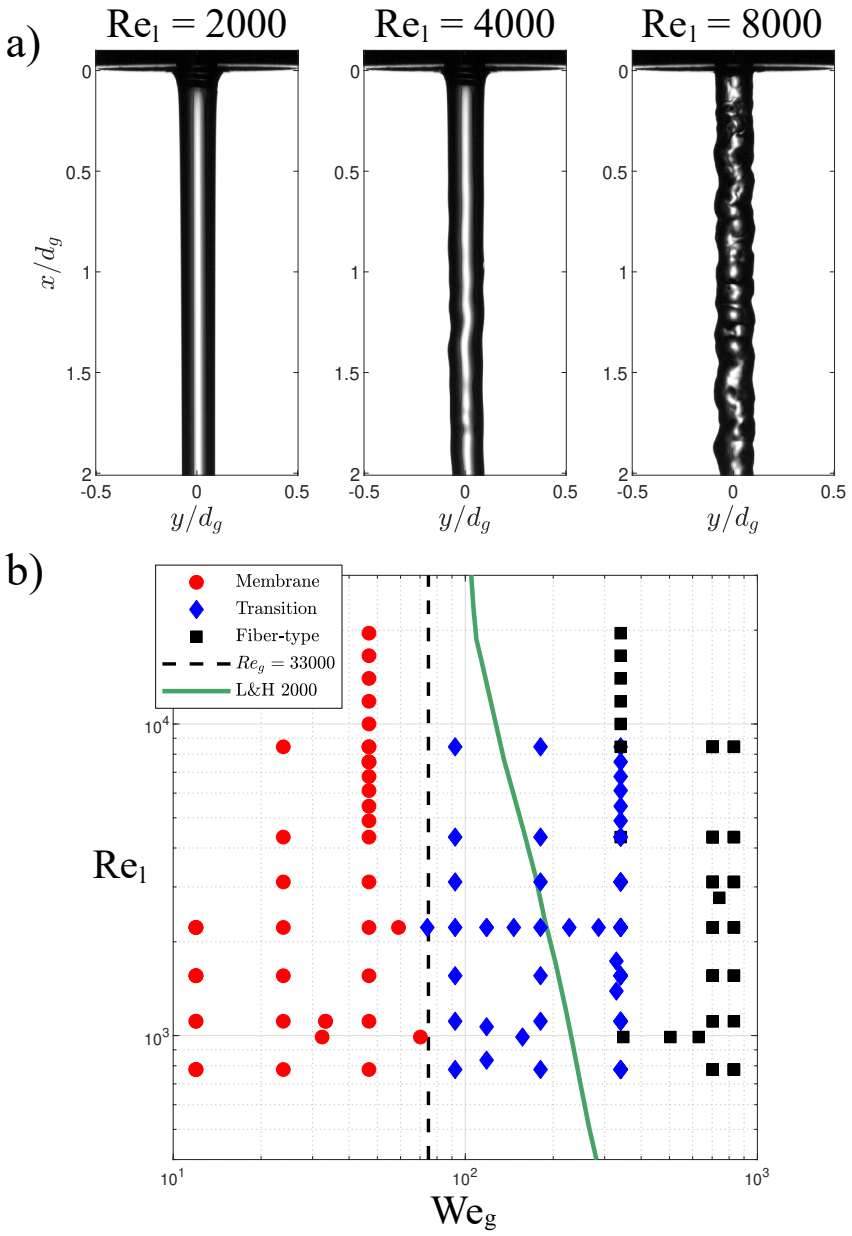

Figure 2.7: a) Snapshot of the liquid jet exiting the nozzle in a still gas environment. For $Re_l = 2000$, the interface of the jet remains unperturbed in the vicinity of the nozzle and the liquid jet is laminar. For $Re_l = 4000$, the interface of the jet only suffers from large-scale disturbances, which suggests that the liquid jet exiting the nozzle is laminar but presents some local flow perturbations. For $Re_l = 8000$, the interface of the jet presents small-scale corrugations, suggesting that the liquid jet exiting the nozzle is turbulent. b) Qualitative phase diagram of breakup regimes in the $\{Re_l; We_g\}$ parameter space. Red circles, black squares, and blue diamonds respectively correspond to membrane breakup, fiber-type atomization, and conditions where both of these breakup mechanisms coexist. The dashed line shows $We_g = 75$ (equivalently $Re_g = 33000$) and the green solid line corresponds to the transition reported by Lasheras and Hopfinger 2000.

We investigate this by looking at a qualitative phase diagram, obtained by visual inspections of the breakup phenomena over the range of explored parameters. Fig. 2.7b) reports in the $\{Re_l; We_g\}$ parameter space membrane breakup, fiber-type atomization, and the transitional regime where both processes coexist. In this representation, the reported transition at $Re_g = 33\,000$ corresponds to a vertical line at $We_g = 75$. Thanks to the many Reynolds numbers sampled, the value of $Re_g = 33\,000$ is tightly surrounded by experimental conditions. It is in good agreement with the change in atomization regimes found here, and with the transition boundary sketched by Lasheras and Hopfinger 2000. It appears that the change of behaviors presented here for $We_g = 75$ occurs at the onset of fiber-type atomization but with coexistence to the membrane formation process. Note that the boundary appears to be (almost) vertical in this diagram in the $\{Re_l; We_g\}$ parameter space. This means that the gas Weber number and not the relative Weber number stands as the good indicator for these transitions since they appear to be almost independent of the liquid velocity U_l. Drawing the phase diagram in the $\{Re_l; We_r\}$ parameter space ($\sim \{U_l; \mid U_g - U_l \mid\}$ parameter space) would only result in a less straightforward view with oblique transitions. While a relative Weber number defined on the phase slip velocity is commonplace in multiphase flow, it seems not to be suited here, as probably noted by Lasheras and Hopfinger 2000 since they use both We_g and We_r but draw the phase diagram in the $\{Re_l; We_g\}$ parameter space. The situation may be different and We_r may be more suited for the fragmentation of a liquid jet by a gas when the velocities of both phases are closer together, as may be interpreted by the curving of the boundary sketched in Lasheras and Hopfinger 2000, as it nears the $U_g = U_l$ line. This is the case for instance in the numerical investigations of Zandian, Sirignano, and Hussain 2019; Zandian, Sirignano, and Hussain 2018, where We_r is used for the regime maps describing the destabilization of a planar liquid sheet segment and a transient liquid jet within a low-speed gas jet respectively. In the case of a liquid jet surrounded by a high-speed gas jet, however, the close inspection of the statistics and temporal dynamics of the liquid core length appears as a good candidate to provide a quantitative framework to describe the transition from membrane breakup to fiber-type atomization.

2.3.5 Scaling along increasing gas velocity: a set of stability curves for gas-assisted atomization

The use of L_B's statistics and temporal dynamics to define quantitatively changes in atomization regimes is a promising finding. This section explores this idea at a fixed liquid Reynolds number $Re_l = 1200$ but in a wider range of gas velocity ($0 \leq We_g \leq 525$), from no gas flow, similarly to the stability curve of pressurized atomization. More details can be found in Machicoane, Osuna-Orozco, and Aliseda 2023. The fragmentation regimes nomenclature is the one proposed by Lasheras and Hopfinger 2000 and sketched in Fig. 2.2. The corresponding regimes are illustrated in Fig. 2.8. The gas Weber number We_g is used throughout, instead of a Weber number based on the velocity difference between both phases, for two reasons: *i)* the previous section

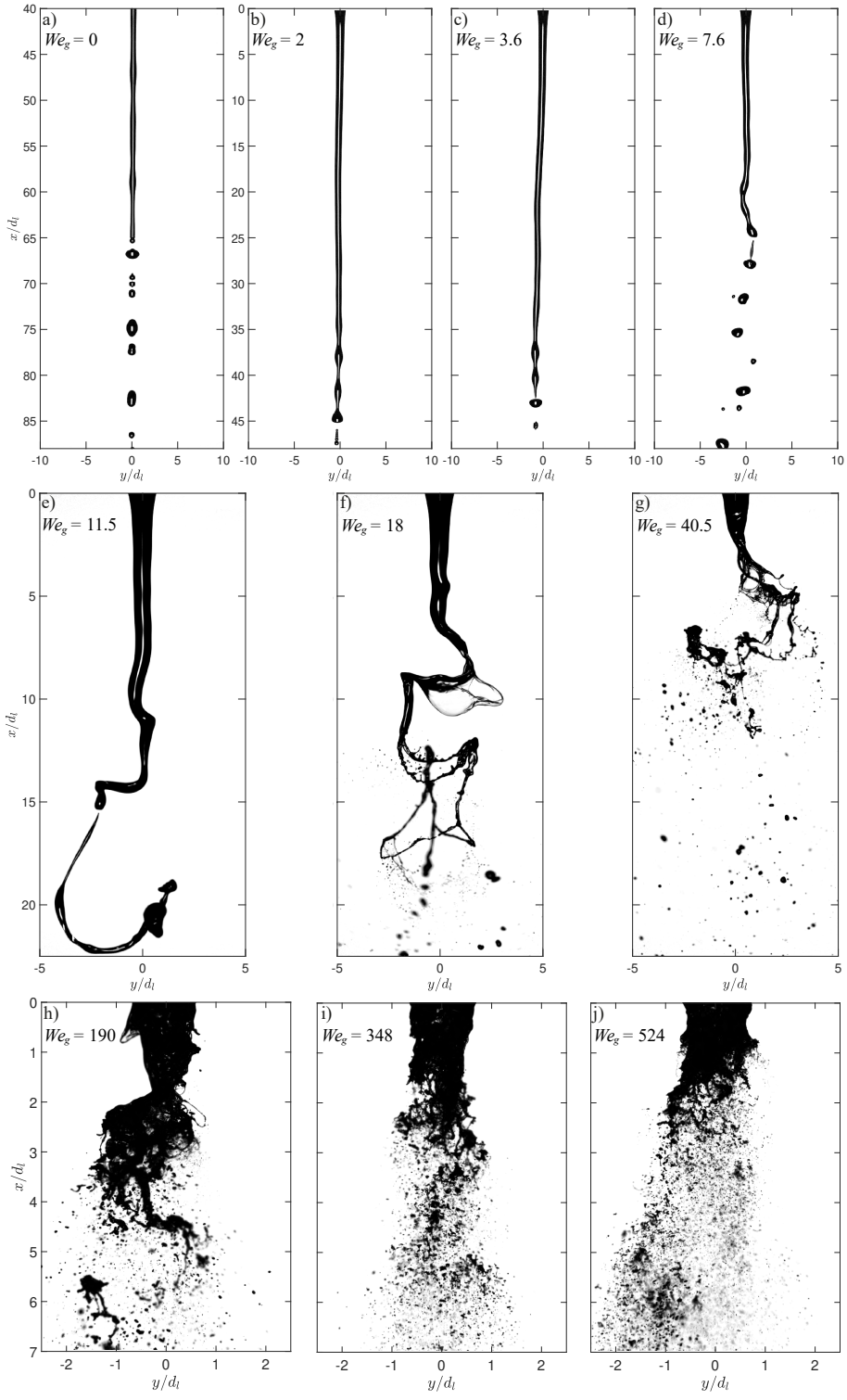

Figure 2.8: Snapshots from high-speed back-lit imaging at different magnifications, highlighted by the growing apparent size of the liquid jet at the exit of the atomizer as We_g is increased from (a) to (i), where $We_g = \rho_g U_g^2 d_l/\sigma$ is the gas Weber number based on the liquid jet inner diameter. a-b) Axisymmetric Rayleigh-Plateau breakup; c-d) Non-axisymmetric Rayleigh-Plateau breakup; Shear breakup without (e) and with bag formation (f-g); Fiber-type atomization, coexisting with bag breakup (h-i) or as a sole fragmentation regime (j).

and Lasheras and Hopfinger 2000 indicate that this seems to be a better parameter to separate fragmentation regimes, and *ii)* power laws with We_g yield the same exponent as with M when Re_l is kept constant and half this exponent with Re_g, making trends simpler to discuss. The scaling laws found are described below, while the main findings are discussed in the conclusion (Chap. 4).

Up to $We_g = 2$, the liquid jet, while presenting shorter liquid core lengths, is fragmented in a manner that is qualitatively unaffected by the gas flow, and axisymmetric Rayleigh-Plateau breakup is observed. For $2 < We_g \leqslant 7.6$, deviations from axisymmetry place these conditions in the non-axisymmetric Rayleigh-Plateau breakup regimes. As illustrated in Fig. 2.8d), the liquid jet is slightly meandering at $We_g = 7.6$ due to the possible onset of the shear instability caused by the difference in velocity between the gas and liquid phases. However, as breakup still happens similarly to that at lower Weber number values, i.e. resulting in typical drops and satellite droplets from a Rayleigh-type breakup, it is not classified as shear breakup regime, and may also be seen as a transitional value. Beyond this value, shear breakup occurs, yielding more polydisperse droplet size distributions. As bag (or membranes) start forming at the end of the liquid jet as early as for $We_g = 18$, the range of bag-less shear-break up is defined as $7.6 < We_g < 18$. At $We_g = 190$, while some bags can still be formed regularly, droplets are stripped from the liquid jet in fiber-type atomization, so bag breakup (without stripping) is observed for $18 \leqslant We_g < 190$. For $We_g \geq 525$, no bag formation is observed and only fiber-type atomization occurs.

Figure 2.9 presents the first two statistical moments of the liquid core length as functions of the gas Weber number. The values at zero gas velocity are represented by black horizontal lines, to appear on the logarithmic scale. For the average liquid core length, a power-law fit of exponent -0.27 ± 0.04 is reported (Fig. 2.9a) as a best fit for $We_g \geqslant 87$, but the values found around $We_g = 40$ are also well captured by it. The scaling of the average liquid core length found at high Weber numbers, which is in good agreement with the literature, seems to apply only for a certain range of the membrane breakup regime and for fiber-type atomization.

A similar scaling is found for the standard deviation of the liquid core length, as demonstrated above, but the data is in agreement with the power law for Weber number values as low as $We_g = 3.6$. It then appears that this scaling applies even in the non-axisymmetric Rayleigh-Plateau breakup regime, while axisymmetric Rayleigh-Plateau breakup yields much higher values of L'_B (the values found at $We_g = 0$ and 2 are approximately 3 times larger than the value of L'_B for $We_g = 3.6$).

Unlike the standard deviation, $\langle L_B \rangle$ displays a clear change of regime between the low and high-velocity range. The lower range of bag-break ($17 \leqslant We_g < 39$), shear breakup, and Rayleigh-Plateau breakup regimes are not captured by the classical $We_g^{-0.3}$ scaling and display a steeper decrease with the Weber number. The best fit provides a power law exponent that is about doubled: -0.61 ± 0.14.

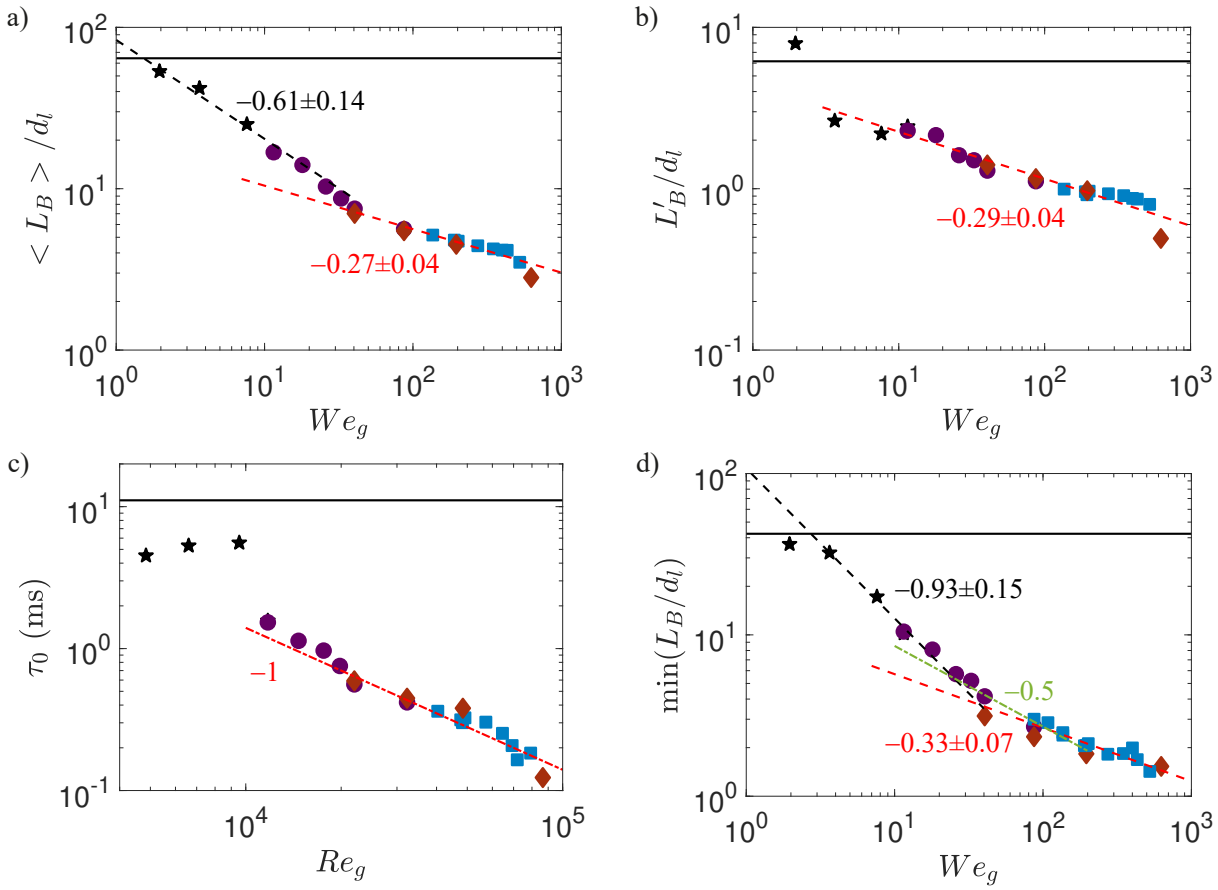

Figure 2.9: Liquid core length mean (a), standard deviation (b), and minimum value (d): $\langle L_B \rangle$, L'_B, and $\min(L_B)$, normalized by the liquid inner diameter d_l and plotted along the gas Weber number based on the liquid jet inner diameter $We_g = \rho_g U_g^2 d_l/\sigma$. c) liquid core length timescale τ_0 plotted along the gas Reynolds number Re_g.
The black continuous lines indicate the values for $U_g = 0$. Black and red dashed lines in a), b), and d) are power-law fits of the data in the low and high range of Weber numbers respectively. The adjacent values are the power-law exponents and their uncertainties, given by the 95% confidence intervals of the fits. A power law of exponent -0.5 is added as a green dash-dotted line in d) to compare to the prediction from Lasheras and Hopfinger 2000.

The minimum value of the liquid core length is also reported in Fig. 2.9d). This is used as a proxy to what is referred to as the liquid cone length, by analogy to the potential cone in a turbulent round jet. This corresponds to the region where liquid is always present and is usually obtained through the processing of average intensity maps from high-speed imaging. To avoid this image processing step that is not standardized among research groups, the liquid core length measurements are leveraged to estimate the cone length. The best fit for $We_g \geqslant 87$ reveals a power-law scaling with an exponent of -0.33, which is in good agreement with the decay of the first two statistical moments. At lower Weber number values, a steeper decrease following $We_g^{-0.93}$ is reported. Conditions in the vicinity of $We_g = 40$ seem to be in the transition between these regimes and are intersected by both fits. Note that while the decay of $\min(L_B)$ is approximately the same as $\langle L_B \rangle$ at high Weber numbers, it is approximately 1.5 times steeper in the lower range of values. The decay of the cone length at high Weber numbers is much less steep than the prediction made from conservation of mass flux arguments resulting in $M^{-0.5}$ at high gas velocities (Lasheras and Hopfinger 2000). A power law of exponent -0.5 is found in the intermediate range of Weber numbers, where moderate agreement could be argued within this restricted range. However, this range appears more likely to be a transition between power laws found at low and high Weber numbers.

The timescale τ_c extracted from the auto-correlation functions of the liquid core length is reported in Fig. 2.9c) as a function of the gas Reynolds numbers. At low gas velocity, this timescale is constant but smaller than in the absence of gas flow (approximately 5 ms versus the value of 11 ms at zero gas velocity). At the onset of the shear breakup regime, i.e. for $We_g \geqslant 12$, a monotonic decrease is observed as the gas velocity increases following Re_g^{-1}, as presented in the previous section.

2.4 Instabilities of the liquid core

The study of the statistics and temporal dynamics of the liquid core length is not giving an indicator for the onset of bags in shear breakup and for the disappearance of bags in fiber-type atomization. A certain view that can be adopted from reading the literature of coaxial atomization, is that the peeling of the ligaments along the liquid core that gives the name to the fiber regime is due to a Rayleigh-Taylor instability. The ligaments, formed by a Kelvin-Helmholtz instability originating from the difference of velocity between each phase, form interfaces that are accelerated, roughly perpendicularly, by the gas flow are can hence be subjected to Rayleigh-Taylor instabilities, leading to their breakup. In this scenario, small droplets are directly peeled off the liquid core (and secondary atomization is most likely negligible, happening mostly on the rim of bags when bags are still present), while without Rayleigh-Taylor instability, the ligaments undergo capillary instabilities and break into large drops that may further break in the gas jet. Note that the situation is much clearer in planar atomization, where joint experimental and numerical work established a Kelvin-Helmholtz (longitudinal) instability forming wave-like patterns, followed by a Rayleigh-Taylor (transverse) instability creating a fingering pattern and ligaments, that then undergo capillary instabilities (Fuster et al. 2013; Ling et al. 2019; Marty, Matas, and Cartellier 2013).

In what follows, the instabilities of the liquid core are studied for a fixed liquid Reynolds number $Re_l = 1200$ and at increasing gas velocity, to investigate potential signatures of changes in fragmentation regimes. First, the large-scale Kelvin-Helmholtz instability, the meandering motion of the liquid core called flapping, is presented, with a focus on its spatial characteristics (the frequency aspects being tackled by Delon, Cartellier, and Matas 2018. Second, the interfacial perturbations, resulting from small-scale instabilities, and their transport along the gas-liquid interface by the gas jet are discussed. Note that there is a slight overlap in both studies, as small-scale Kelvin-Helmholtz instabilities are observed to affect the flapping dynamics. More details can be found in (Kaczmarek et al. 2022; Ricard et al. 2021).

2.4.1 Flapping

Similarly to the two-view approach of Matas and Cartellier 2013, two high-speed cameras are used to obtain back-lit imaging of the spray along two perpendicular projections. This is done by placing two bright sources of light behind the spray, each pointing toward a camera. The cameras are positioned in a horizontal plane and are orthogonal to each other (see Fig. 2.3c). Both cameras are synchronized and are triggered by the same input signal. A frame rate of 10 000 Hz with a duration of 1 s, an exposure time of 7 μs, a resolution of 52 μm/pixel, and a field of view of 42×34 mm^2 are used in the data collection. Both cameras capture orthogonal projections of the spray, leading to the ability to measure the 3D position of imaged objects, via

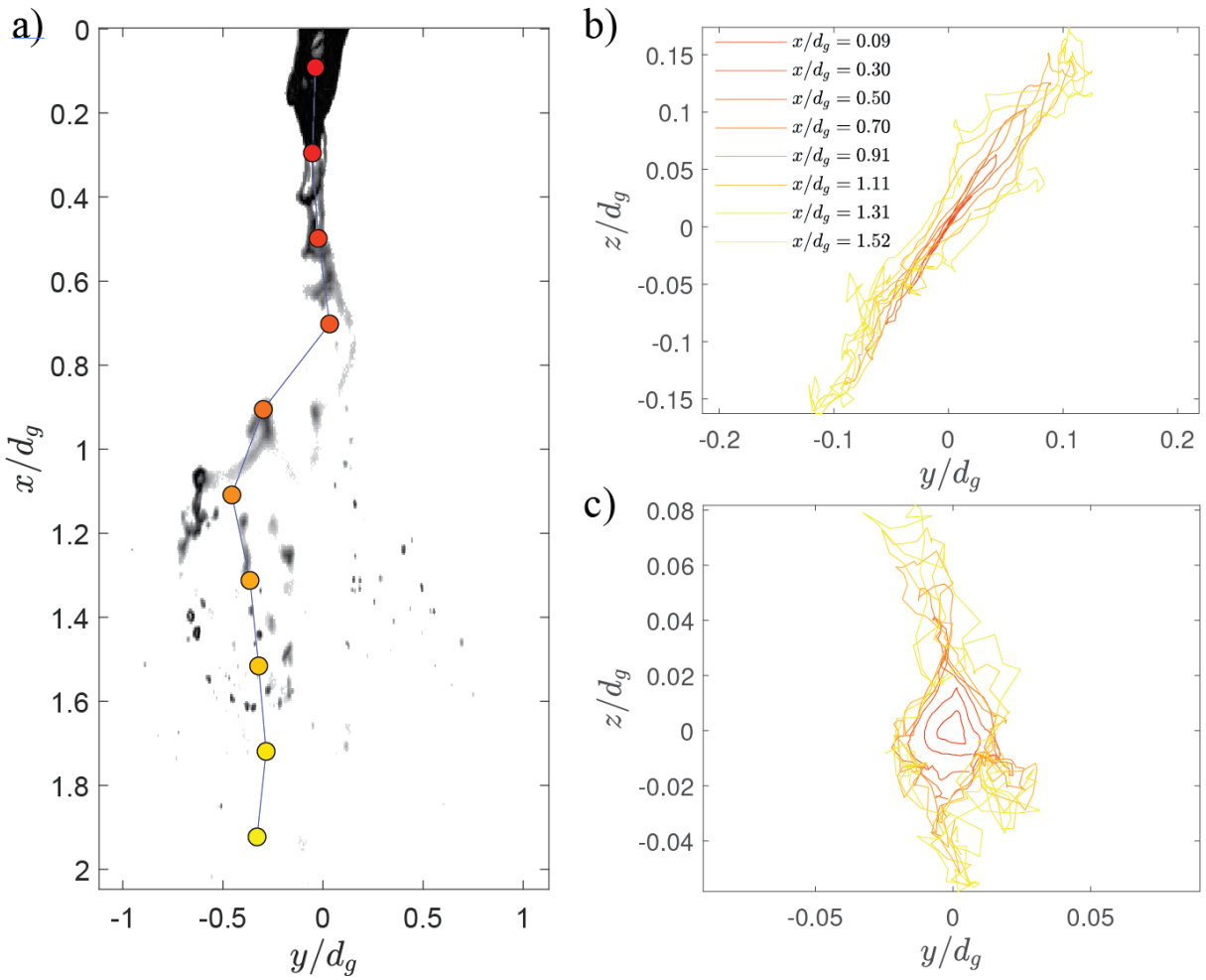

Figure 2.10: a) Typical snapshot from one view with associated detected liquid barycenters. b) Flapping orbits displaying different shapes obtained for $We_g = 16$ (b, planar), $We_g = 40$ (c, ellipsoidal).

a calibration step.

The method proposed here is based on a simplification of the spray structure in the near-field, as only the movements of the bulk of the liquid are studied and not the movements of individual features (e. g. ligament, drop). Therefore, the spray images are divided into 10 equal overlapping horizontal windows on which the barycenters of grey shades are calculated in order to determine the mean position of the liquid presence in each window (Fig. 2.10b). As a shadowgraph only gives information about the presence or absence of liquid, and not about the quantity of liquid present, the barycenters are calculated by giving the same weight to all pixels assigned to contain liquid (see Machicoane et al. 2020) instead of taking into account the grey intensity of each pixel. Moreover, an overlap between two consecutive windows of 33% is used to act as a sliding average

over the variation of the barycenters' positions versus longitudinal distance x, while increasing the effective sampling resolution. The position of the barycenter of each window is computed on each view (for any window at a downstream distance x, view 1 and 2 respectively yield y and z) and is then used to obtain the 3D position of the liquid barycenters (x, y, z). This simplified three-dimensional representation of the spray is used to study the spatial and temporal evolution of the liquid jet flapping (including both its liquid core and some detached liquid inclusions without distinction).

Note that the liquid presence barycenter method with two-view back-lit imaging, while representing well the spatiotemporal dynamic of the bulk of the liquid phase in the near-field of a two-fluid coaxial atomizer, would not be adequate to describe the spray mid and far-field or phase objects of complex shape such as large deformed bubbles. In the former, the presence of small liquid droplets far from the centerline could for instance lead to overestimate weights in the barycenter computation compared to much larger drops close to the center. In the latter, projected areas can be drastically overestimated, especially for non-convex shapes (see Masuk, Salibindla, and Ni 2019 for an in-depth discussion).

In order to identify the flapping frequency, the power spectral densities (PSD) of the y-axis and z-axis position of each barycenter can be calculated from their time series obtained with this method. Note that for high values of the dynamic pressure ratio (i. e. for high gas velocities here), flapping happens at high frequency (Delon, Cartellier, and Matas 2018). Beyond $We_g = 87$, the peak in the PSD that corresponds to flapping is found in the high-frequency range where a decaying power law is observed beyond 300 Hz for instance), and a faithful determination of the dominant frequency becomes challenging. This was also the case for the determination of the shedding frequency based on the liquid core length time series in Machicoane et al. 2020, where a typical timescale was retrieved using auto-correlation functions instead. Such determination would be easier using higher spatial and temporal resolutions, which were not obtainable in the present work. In the following, the study hence focuses on the flapping morphology transition in the shear breakup regime of coaxial atomization for $We_g \leq 87$.

Once the main frequency f_0 is determined as the PSD maximal peak, the 3D positions of all the barycenters (for each x position) are phase-averaged over many periods $nT = n/f_0$ ($n \geq 50$ and $n \in \mathbb{N}$) and studied over an average complete flapping motion of duration T (Fig. 2.10b-c). This yields closed orbits, by definition, that correspond to the average motion of the liquid bulk along one flapping period T. As expected, the orbit extent increases with downstream distance as the flapping motion gains amplitude. The shape of the orbits does not appear however to change with downstream location.

The case $We_g = 16$ leads to a seemingly planar flapping, while the case $We_g = 40$ results in a transitional state between planar and circular flapping (observed at higher gas velocity or when swirl is added to the gas jet), referred to as elliptical here (see Fig. 2.10b-c). This transitional elliptical state is characterized by a circular motion of the barycenters close to the nozzle of the

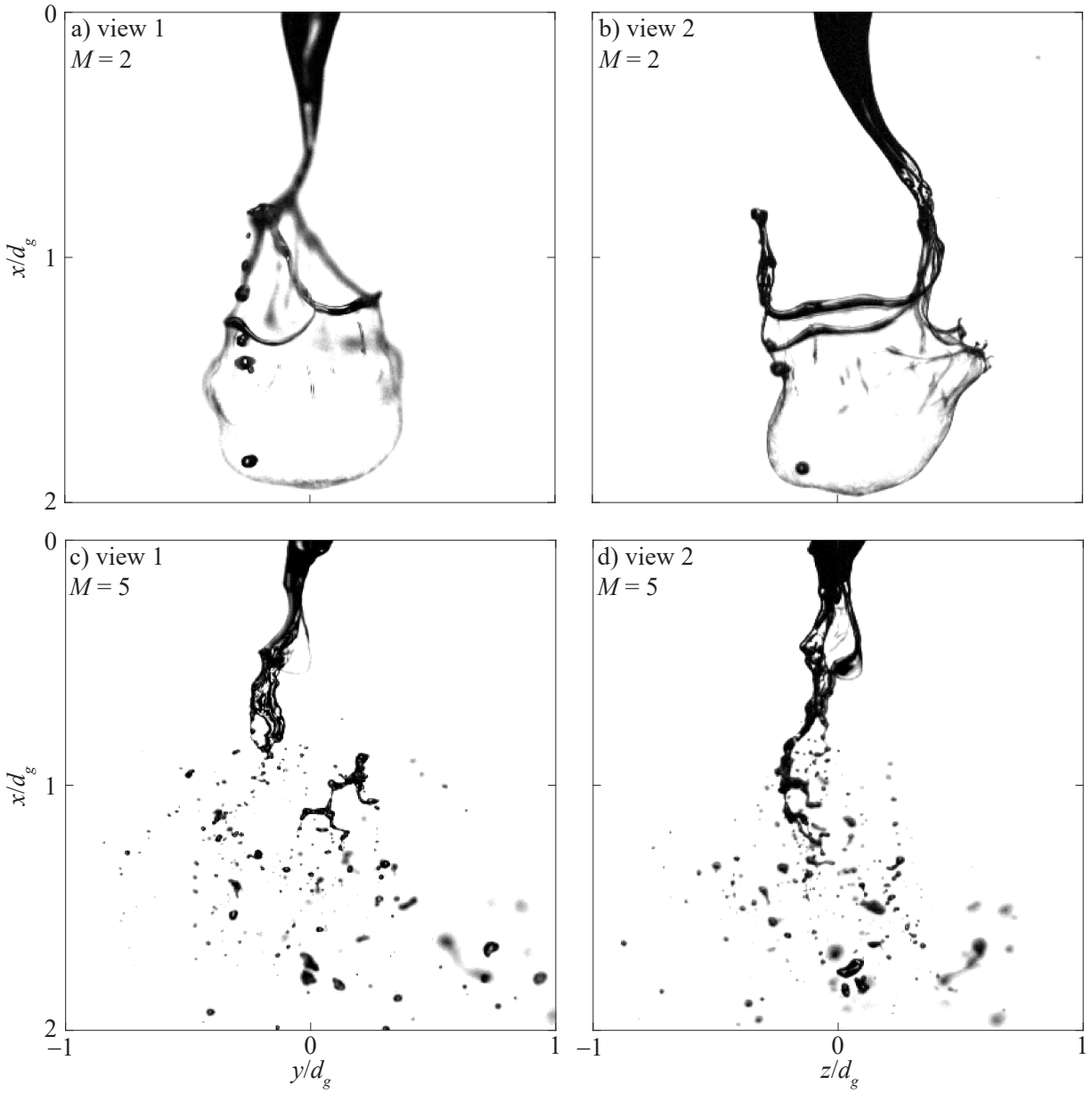

Figure 2.11: Snapshot displaying bag formation originating from the large-scale flapping instability at $We_g = 16$ (a-b) and from a small-scale interfacial instability at $We_g = 40$ (c-d).

atomizer, which tends toward a planar motion as they move away from it (or at least with a clear preferential direction, along z in this example). Note that for transitional orbits, there is a change in orbit shape as the downstream distance increases, as orbits close to the exit plane are found to be almost circular. Typical studies in the literature generally use only one camera. This work shows that this would lead to biased measurements of the flapping amplitudes in cases where planar or transitional 2D-3D flapping is occurring. In the case of $M = 5$, the mean flapping amplitude along z can be estimated to be about 3 times larger than along y (which is where the largest error in flapping amplitude that could be made if a one-view measurement was performed along y.

The shape of the flapping orbits can be characterized quantitatively (Kaczmarek et al. 2022), and the transition in flapping shape is reached for $We_g = 40$ here, with the shape parameter falling below 1.5. While this operating condition corresponds to a Weber number, is very close to the one reported for transition between shear breakup and membrane breakup by Lasheras and Hopfinger 2000 for the laminar liquid Reynolds number $Re_l = 1200$ (Fig. 2.2). However, in the current range of operating conditions for this atomizer, bags are observed even at the lower Weber number value explored of $We_g = 16$ (see Fig. 2.11a-b). In this case, as the liquid core meanders due to the flapping instability, bags are blown in the last portion of the jet, where the liquid resembles a hook shape. The bottom of this hook presents a region that is transverse to the gas jet which stretches it into a thin membrane that is referred to as a bag. On the other hand, for $We_g \geq 40$, another mechanism leads to the formation of bags. Small-scale interfacial instabilities, namely shear-driven Kelvin-Helmholtz, produce interfacial perturbations that once elongated by the gas stresses, can be blown into bags that are attached to the side of the liquid core (see Fig. 2.11c-d). These bags coexist with the ones originating from the large-scale flapping instability (Fig. 2.11c-d is for instance taken right after the rupture of such a bag, and the larger drops resulting from the rim are visible on the snapshots. It appears that the described transition between (bag-less) shear breakup and (shear) bag breakup described in Lasheras and Hopfinger 2000 onsets earlier here and that the prescribed transition around $We_g = 40$ is more closely related to the relative role between large-scale and small-scale instabilities becoming more or less comparable in bag formation. The difference in the transition value of We_g between the present work and the proposed transition in Lasheras and Hopfinger 2000 could be due to subtle dependencies in the atomizer geometry. In particular, while the inlet liquid diameter d_l is expressed linearly in We_g, the ability of the gas to stretch the elongated liquid jet could depend non-linearly on this quantity. This hypothesis would however need to be further investigated in a liquid Reynolds number - gas Weber number parameter space that also includes variable atomizer geometry.

The transitional elliptical shape indicates a strong preferential direction, here along z, with deviations along y only when the liquid bulk is located closer to the centerline (at small radial distances). In the absence of bag formation along the liquid jet (i. e. bags only originating from flapping and located approximately in the last third of the liquid core), at $We_g = 16$, the liquid bulk flaps back and forth in a plane. The liquid core mostly corresponds to a twisted

liquid column which experiences regular fragmentation associated with bag breakup. The rupture at the most stretched portion of the bag propagates up to the rim and breaks the liquid jet tip altogether. In contrast, at $We_g = 40$, bag formation can also originate from small-scale interfacial instabilities, and partial breakup of the liquid jet happens before the end of the liquid jet. While a bag is inflated, despite representing a very small portion of the liquid mass as the membrane is very thin, it offers a large increase in the aerodynamic drag experienced by the liquid jet (acting like a spoiler). The formation of bags from small-scale interfacial instabilities tends to be associated with a liquid core and detached liquid bulk mostly aligned with the centerline. On the other hand, the bags happening at the extrema of the flapping period are associated with twisted liquid jets, that remain thin up to their tip where the bag is formed. The presence of bags close to the nozzle (at a few liquid diameters), offers a thick liquid column that is suspected to yield additional drag, which could oppose large-amplitude flapping in a preferential direction. It is likely that the emergence of this added drag around $We_g = 40$ is what leads to the transition in flapping dynamics. This phenomenon results in the region of $r < 0.02 d_g$ in Fig. 2.10c) which bounds all of the flapping orbits at the downstream distances sampled. At low Weber number (planar flapping) or with swirl (circular flapping), such region does not exist as the liquid core's main direction strongly deviates from the centerline.

2.4.2 Interfacial perturbations

Different experimental challenges arise in observing instabilities along the intact part of the liquid jet. The length of the liquid core, where instabilities might appear, is of the order of several millimeters and they only exist during a time of the order of milliseconds. High spatial and temporal resolution shadowgraphy addresses these challenges and aims at better describing the growth and acceleration of interfacial perturbations in coaxial two-fluid atomization. The resolution used varied between 6 and 26 microns/pixel, depending of the magnification considered, allowing a maximum frame rate of 10 kHz, which is well suited to track the interface motion. Due to the fast temporal scales of the process studied, a low exposure time was chosen (285 ns) to prevent blurred motion.

To study the different instabilities of the interface, as they develop along the surface of the liquid jet, we chose a Lagrangian approach, tracking their position with time. We use a tracking method similar to Gutteridge 2019 and Singh et al. 2020. This tracking analysis is applied independently on both cross-sections of the interface (as the image focal plane intersects the liquid jet it defines two contours). First, the location of the edge of the jet is found using the binary image. Then, the interfacial perturbations are located by finding the local maxima of the line from edge detection. A nearest neighbor tracking code is applied to the image sequences, due to the sparse nature of this tracking problem, yielding the coordinates of the interfacial

perturbations over time. Finite difference is applied to the trajectories to obtain the velocities of the interfacial perturbations.

Two examples of the Lagrangian trajectories obtained are represented in Fig. 2.12 for $Re_g = 21,300$ (a) and $Re_g = 69,400$ (b), respectively $We_g = 40$ and 400. As the characteristic timescales widely differ between these conditions, some frames in the sequence are skipped in (a), for better visibility. One can observe that for high values of Re_g the spatiotemporal scales of the process are much smaller than for low values. This illustrates the need for a multiscale analysis, as is conducted in this study.

The interfacial perturbations travel along the intact length of the jet as they are advected by the high-speed gas. The average velocity at each location along the longitudinal axis of the liquid jet is computed by Eulerian conditioning of the tracks $\left\langle \mathbf{v}^E(x) \right\rangle$. The Lagrangian location along the spray axis is discretized in bins, where x corresponds to the center of a bin. $\left\langle \mathbf{v}^E(x) \right\rangle$ is then computed as the average of the velocities for interfacial perturbations measured at the locations contained in the bin centered on x (Fig. 2.12c). Velocities increase along x, which means that the interface accelerates downstream. Increasing the gas velocity U_g increases the slopes of $\left\langle \mathbf{v}^E(x) \right\rangle$.

One observation from this study is that both the perturbation velocity evolves linearly with the downstream distance x. Typical interfacial perturbations have been observed to travel at a constant velocity, namely the convective velocity: $U_c = \frac{\sqrt{\rho_l}U_l + \sqrt{\rho_g}U_g}{\sqrt{\rho_l}+\sqrt{\rho_g}}$ (Fuster et al. 2013; Marty, Matas, and Cartellier 2013). This situation corresponds to waves, created by instabilities, that propagate downstream at a given celerity. However, here, for coaxial atomization at high gas Reynolds numbers, once the perturbations are formed, their crests seem to be immediately exposed to strong hydrodynamical forces and they should be treated as Lagrangian objects: the crests get accelerated, leading to a growing velocity along the liquid core length. This increase of velocity has already been reported by Marmottant and Villermaux 2004, using double exposure imaging to compute instantaneous velocity measurements, and by Gutteridge 2019, who averaged interfacial velocities in a 3 mm window using an image correlation method.

The evolution of $v_x(x)$ is fitted using a linear function from the data of Fig. 2.12c), restricted to the range where it is linearly accelerated (excluding the large deformation/breakup events). This velocity gradient is made dimensionless using $\frac{d_l}{U_g}$, and plotted versus the gas Reynolds number in Fig. 2.12d). Two regimes appear: when $Re_g < 45,000$ (equivalently $We_g = 190$, reached for $U_g = 76$ m/s), we can observe that $\frac{\partial \langle v_x^E \rangle}{\partial x}\frac{d_l}{U_g}$ evolves linearly with Re_g, whereas when $Re_g > 45,000$ it reaches a plateau. This corresponds to a quadratic then linear evolution along the gas velocity U_g. Marmottant and Villermaux 2004 also observed a regime where the spatial velocity gradient of the longitudinal velocity grows with Re_g. Despite a very similar coaxial jets configuration, they found that $\frac{\partial \langle v_x^E \rangle}{\partial x} \propto U_g^3$ so that $\frac{\partial \langle v_x^E \rangle}{\partial x}\frac{d_l}{U_g} \propto Re_g^2$, in the range they explored (five operating conditions with gas velocities from 15 to 30 m/s). The plateau reached at high gas Reynolds number is reminiscent of scaling laws found for fully-developed high Reynolds

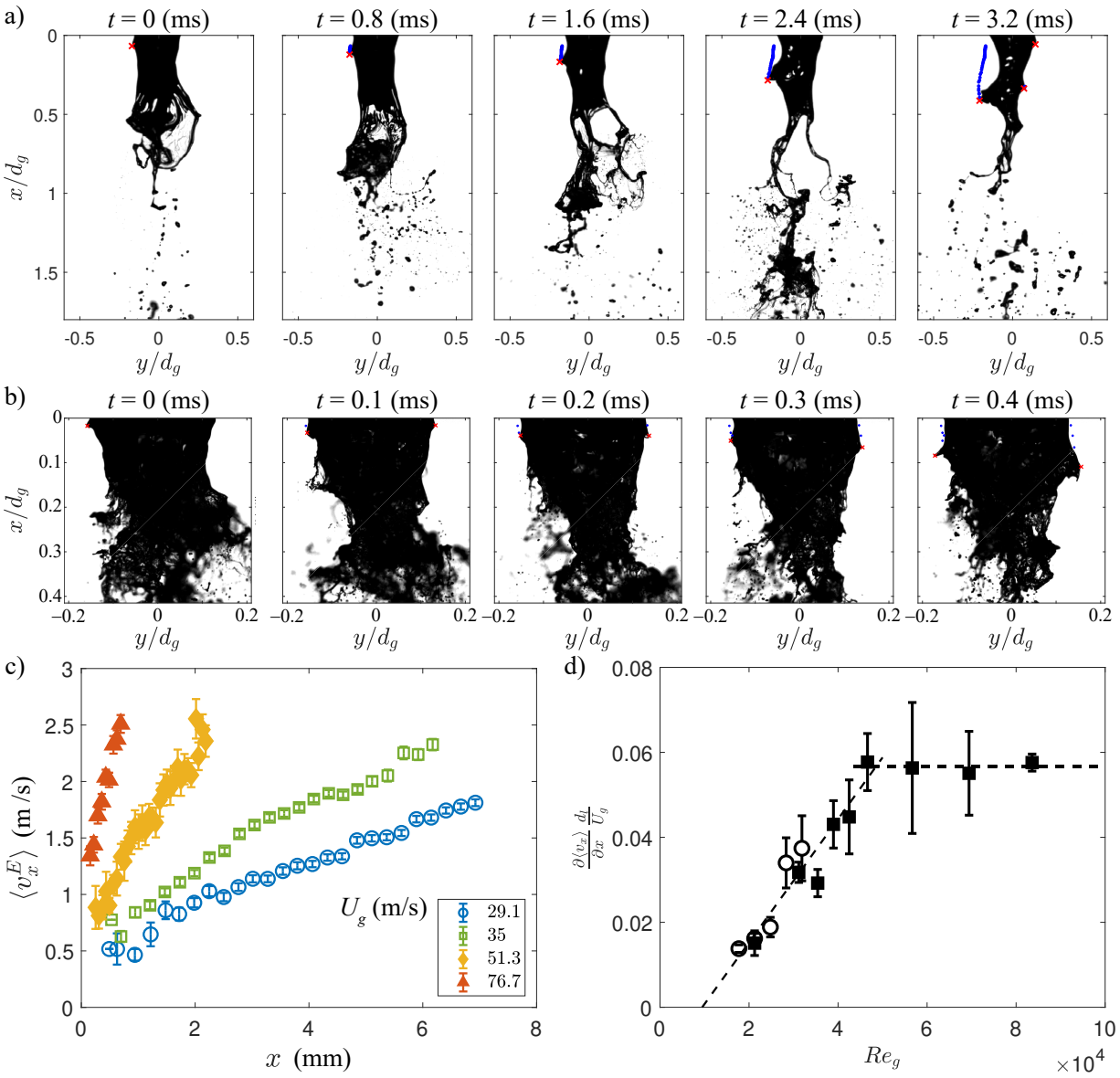

Figure 2.12: Two images series displaying the tracking of interfacial perturbations along the liquid jet, with $Re_g = 21,300$ (a) and $Re_g = 69,400$ (b), respectively $We_g = 40$ and 400, obtained at different magnifications. The red crosses represent the perturbations found on the displayed frame, while the blue dots correspond to the locations detected on previous frames, highlighting the trajectories. c) Evolution of the local time-average longitudinal velocity of the interfacial perturbations advected along liquid core (standard deviations as error bars). d) Non-dimensionalized spatial velocity gradient. The empty symbols are obtained using a magnification of 0.77, and the filled symbols using a magnification of 3.3.

number fluid mechanics (e. g. asymptotic values of turbulent velocity fluctuations normalized by a mean or forcing velocity in turbulent flows at high Reynolds numbers), hinting that they are purely driven by the fully turbulent gas jet. Scaling laws were presented in terms of Re_g for that reason and for comparison with Marmottant and Villermaux 2004, but can simply be converted in terms of We_g since $We_g \sim Re_g^2$ here.

CHAPTER 3

High-speed sprays

After studying fragmentation regimes and instabilities in coaxial two-fluid atomization at low to moderate gas velocities (up to Mach numbers of $Ma = 0.5$), what follows is dedicated to high-speed sprays ($Ma \sim 0.95$), approaching velocities that can be found in propulsion or metal powder production applications.

3.1 Motivations

Gas-assisted atomization is a process which, while largely used in propulsion applications (*e.g.,* low regime LOX-CH4 engines) is still impossible to model reliably given its complexity, which causes safety issues. In addition, it is difficult to limit the strong NOx pollution caused by large droplets in turboreactor applications. While cryogenic benches using liquid oxygen (LOX) are available at Pennsylvania State University, at ONERA in Paris (Mascotte facility), and at DLR in Lampoldshausen (P8 bench, they have been designed to investigate combustion and the effect of pressure on the flame structure, its stability, its propagation during ignition. In most experiments, combustion was activated so that drops were subject to strong evaporation within sharp temperature gradients (as discussed in Ladam et al. 2001; Ladam 2000 in a fundamental context). Very few cold flow conditions have been considered mainly because of the excessive running costs of such facilities and of strong technical constraints. The corresponding test conditions happen to be quite scattered both in terms of flow rates and injector geometries so that no systematic sensitivity analysis has been performed so far. In particular, the typical recorded mean drop sizes vary from 20 to 120 micrometers and could result from large-scale instabilities as well as from stripping. Clearly, such benches are inappropriate for a refined investigation of atomization mechanisms. The strategy proposed here to tackle this issue is to target very high gas velocities.

When studying the atomization of a liquid jet by a high-speed gas jet, the resulting turbulent two-phase flow cannot be probed accurately using visible light as it becomes optically dense. X-ray, unlike visible light, suffers from only weak scattering by gas-liquid interfaces and has been shown to be among the best candidate to probe such two-phase flows (Aliseda and Heindel 2021), due to its penetrative nature and high energy. This is particularly true when using Synchrotron

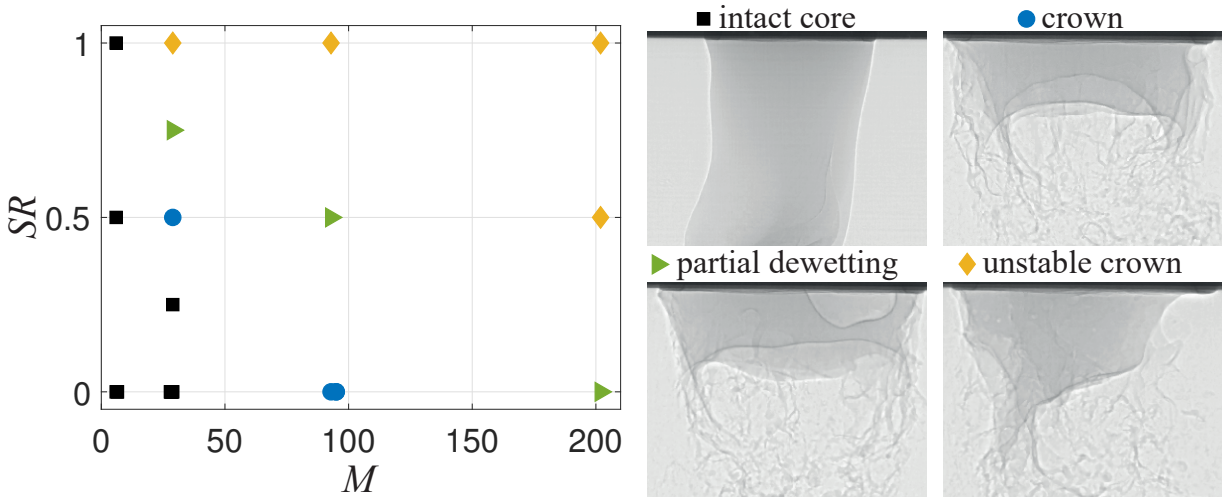

Figure 3.1: Phase diagram of the liquid core morphology. The intact jet corresponds to a liquid column, which can be deformed in sinusoidal or varicose modes, forming bags or ligaments. The crown refers to a liquid core with a hollow center that can extend up to inside the water needle. Partial dewetting implies that the liquid crown detaches on part of the liquid needle perimeter, but the liquid crown is still found downstream of the detachment, forming a full 360° liquid sheet. An unstable crown corresponds to the detachment of the liquid for the larger part of the liquid needle perimeter, where the gas recirculation cavity invades the liquid needle, preventing the liquid core from reaching the full azimuthal liquid needle perimeter.

X-ray sources, and pioneering work was conducted on sprays at the Advance Photon Source of the Argonne National Laboratory (APS-ANL) in the early 2000s (Cai et al. 2003; Powell et al. 2000). The focus of this work, conducted in the context of diesel sprays, was on the liquid mass distributions in the near-field, which was retrieved by shooting a focused monochromatic X-ray beam (half a dozen μm across) and measuring absorption along that line-of-sight with a diode. Shortly after, Wang, Im, and Fezzaa 2008 imaged coaxial atomization using X-ray for the first time and showed ligament breakup around a liquid jet by a high-speed gas flow. This was achieved using a broader and polychromatic X-ray beam (half a dozen mm across; the increase in cross-section requires more energy which is attained by letting the full spectrum of the Synchrotron-produced X-ray at APS-ANL, while previous work filtered it to a narrow bandwidth*). The X-ray beam is absorbed by a scintillator crystal, that reemits visible light that can be captured by a camera. In the work of Wang, Im, and Fezzaa 2008, either single independent snapshots were captured, or the superposition of a few snapshots on the same image (multi-exposure), due to camera limitations.

More recently, Machicoane et al. 2019 were able to perform time-resolved imaging of

*More detail about both techniques can be found in (Bothell et al. 2020; Kastengren et al. 2012; Kastengren et al. 2010; Li et al. 2019).

the atomization process of a coaxial gas-assisted atomizer using the same approach but taking advantage of the advances of modern high-speed cameras. Some features of the internal details captured with such techniques are described in a Gallery of fluid motion video https://doi.org/10.1103/APS.DFD.2017.GFM.V0026. A semi-quantitative analysis is employed to classify the morphology of the liquid core (Fig. 3.1). The gas recirculation behind the liquid core is imaged for the first time: ligaments are pulled from the periphery of a hollowed-out liquid core (the "crenelations" terming this morphology as a liquid crown). When gas swirl is employed, the gas recirculation is able to penetrate inside the liquid nozzle, and the liquid can only exit through a reduced cross-section. Similarly to the recirculation behind a blunt body (Grandemange, Gohlke, and Cadot 2013), the gas recirculation is unstable and switches position within the liquid nozzle cross-section, driving the motion of the liquid crown (hence termed unstable crown).

In what follows, recent work building upon these past studies is presented, in particular with a focus on the role of the liquid Reynolds number in high-speed spray formation and with efforts to obtain quantitative results out of Synchrotron high-speed X-ray imaging.

3.2 Synchrotron X-ray phase-contrast imaging

Figure 3.2 compares back-lit and Synchrotron X-ray imaging for two example conditions taken in the membrane breakup and fiber-type atomization regimes. While, for the former, access to some internal details, such as bubble capture by the reattachment of interfacial perturbation (similar to bubble capture by non-breaking waves at the ocean surface), or the potential access to film thickness assessment, can be appreciated, Synchrotron X-ray imaging may not be as suited for such two-phase flows. In particular, the size of the imaging window, limited by the beam radius, is much smaller than the typical liquid core length, requiring the capture of successive imaging windows at different positions along the spray formation region, in an unsynchronized manner. This explains why the conditions taken at ESRF follow iso-M lines in the (Re_l, We_g) parameter space (presented later in Fig. 3.4). From the prior knowledge of the scaling laws of the statistics of the liquid core length with the gas-to-liquid pressure ratio, a minimum value of M was chosen so that the maximum liquid core length would remain below 16 mm, limiting the number of imaging locations to 3 along the longitudinal distance x (totaling 5 windows for such condition with an addition of 2 off-centered windows to capture the flapping motions of the liquid core).

In the case of high Weber number conditions, in the fiber-type atomization regime, the low to moderate liquid Reynolds number values explored yield much lower M so that most conditions can be captured with only one imaging window at the exit of the nozzle and a few are probed using two on-axis windows. Note that in addition, for a few conditions in the unstable

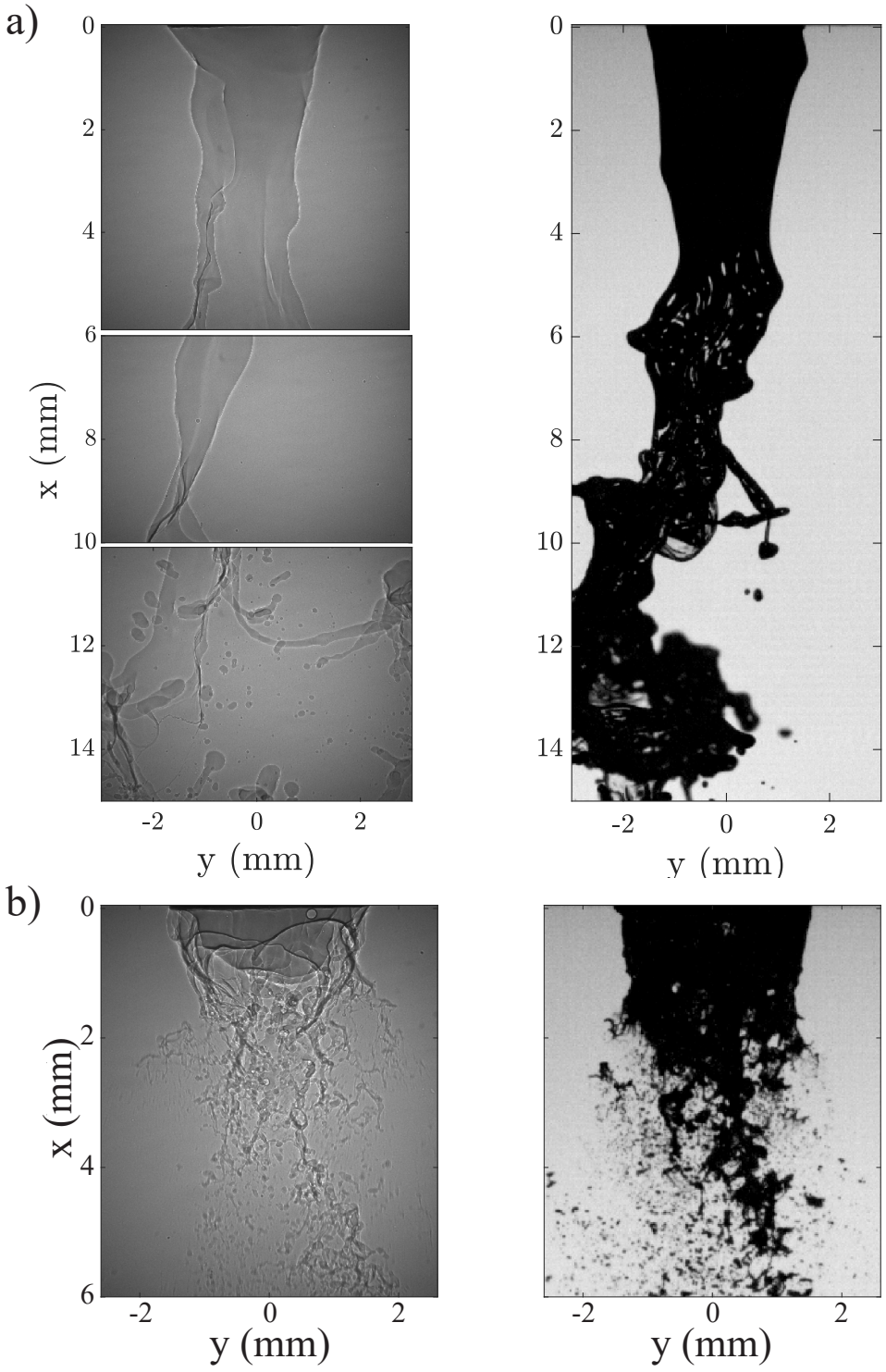

Figure 3.2: a) Membrane breakup at $Re_l = 780$ and $We_g = 24$, captured using X-ray radiography (using several windows captured at different times) and back-lit imaging. b) Similarly at $Re_l = 780$ and $We_g = 340$, in the fiber-type atomization regime.

crown regimes, imaging of the flow within the liquid nozzle was also conducted. Beyond that unique capacity of imaging through metallic non-transparent walls, Synchrotron X-ray high-speed imaging reveals all the gas-liquid interfaces produced at high gas Weber numbers which remain inaccessible using visible light (Fig. 3.2). While the interfaces tightly overlap in their X-ray projections, they are still discernible and the morphology of the liquid core becomes observable. This is not the case using back-lit imaging, where even with a very narrow probe volume (depth of field of the order of the mm), visible light cannot penetrate the dense turbulent two-phase flow found in the vicinity of the liquid jet, which appears as a connected dark region. In this case, the measure of the liquid core length is biased beyond any thresholding consideration or any other experiment error, and such conditions were excluded from the study of Chap. 2.

3.3 Morphology of the liquid core

Compared to the mentioned previous work, the current study presents a few technical advantages. The total acquisition time is much longer and in the form of a continuous 1 s recording (instead of several 30 ms recordings spaced by 300 ms due to the presence of a chopper wheel preventing heating up of the scintillator caused by the broader beam spectrum). In addition, using prior knowledge of the observed liquid core morphologies (Fig. 3.1), a tighter sampling of the parameter space was conducted. Finally, limiting the study to conditions of a moderate liquid core length (to limit the number of acquisition windows), the effect of the liquid Reynolds number could be studied.

Figure 3.3 presents successive snapshots (skipping frames for visibility) of the atomization of a liquid jet at $Re_l = 780$ by a gas jet at $We_g = 180$, where both membrane breakup and fiber-type atomization coexist. In this case, the liquid core looks alternatively like an intact core and a crown. However, the gas recirculations, indirectly visualized by the local deformation of the gas-liquid interface and by the path of the detached drops, are not a large-scale vortex stably located behind the liquid core, but rather in the form of many small-scale gas recirculations of short lifetimes, creating many dimples in the interface. In the case of higher gas Weber number, this newly-identified transitional regime between intact core and crown is also observable, but for larger values of the liquid Reynolds number, displaying highly corrugated liquid cores (Fig. 3.4).

In addition to highlighting a transitional morphology, the exploration of the high-We_g low-Re_l region results in very high values of the gas-to-liquid dynamic pressure ratio ($M \geq 180$) where an unstable liquid crown was observed in the absence of swirl (only reached for $SR \leq 0.5$ in Machicoane et al. 2019). The resulting phase diagram is presented in Fig. 3.4, with example morphologies illustrated by a snapshot of the intact core ($Re_l = 780$, $We_g = 47$), transitional

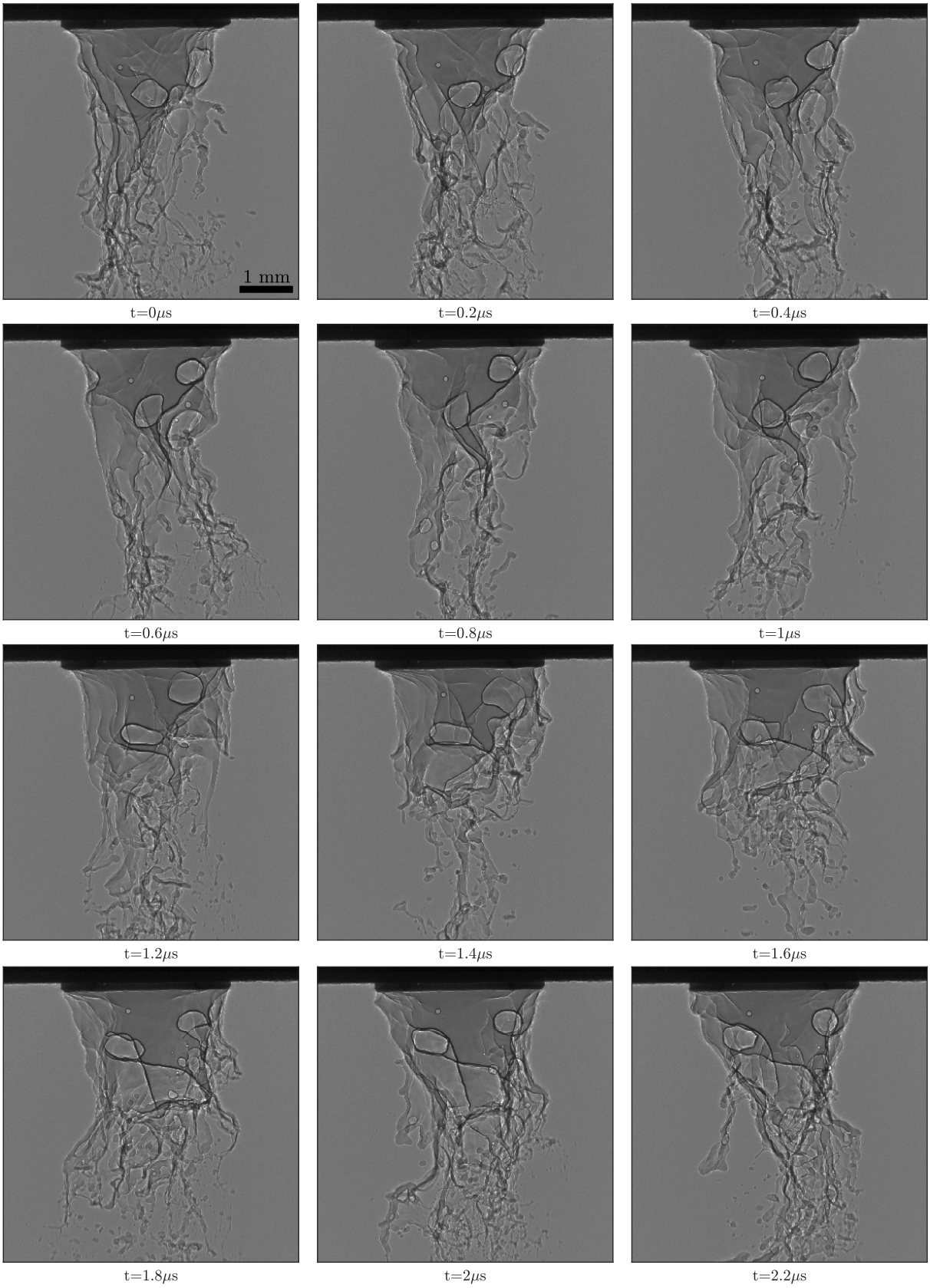

Figure 3.3: Time series of radiographs of the atomization process at the exit of the nozzle at $Re_l = 780$ and $We_g = 180$.

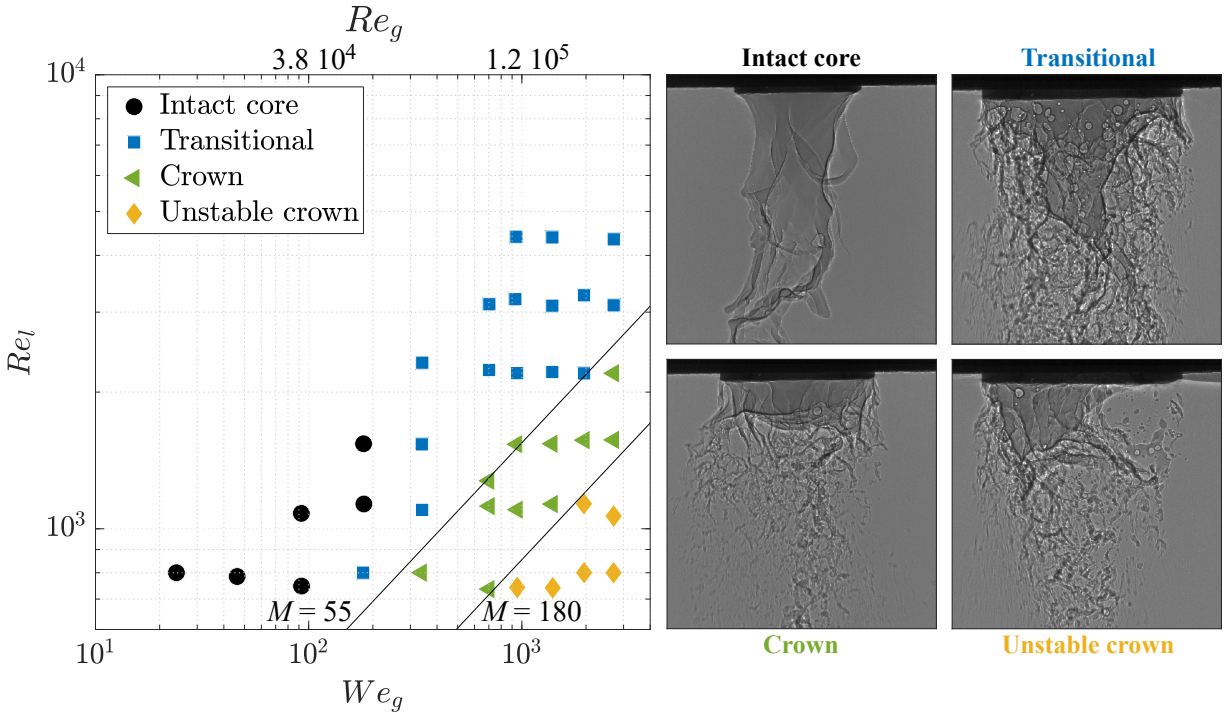

Figure 3.4: Phase diagram of the morphology of the liquid core in the liquid Reynolds number Re_l, gas Weber number We_g parameter space, with example pictures of the four identified morphologies. The gas Reynolds number Re_g is indicated on the top axis, and iso-values of the gas-to-liquid dynamic pressure ratio $M = 55$ and 180 are displayed.

regime ($Re_l = 2200$, $We_g = 340$), crown ($Re_l = 780$, $We_g = 340$), and unstable crown ($Re_l = 780$, $We_g = 945$). While the transition between the first two regimes is unclear with the sampled conditions, the subsequent transitions appear to be in good agreement with iso-M lines of values $M = 55$ and 180.

3.4 Retrieving Equivalent Path Length maps

When a monochromatic X-ray wave $\Psi(z)$ goes through a medium of thickness t with a complex refractive index $n = 1 - \delta + i\alpha$, it is described by $\Psi(z) = E_0 e^{inkz}$, where k is the wavenumber of the X-ray and E_0 its initial amplitude. Note that in a general context, the medium can be dispersed into many elements i of thickness t_i and any element that the beam passes through contributes to the total thickness $t = \sum t_i$, referred to as the equivalent path length (EPL). The propagation of the X-ray wave leads to an exponential decay of the amplitude by a factor $\int_0^t e^{-k\alpha(z)z}$, related to the complex part of the refractive index of the medium, and a phase shift $\Delta\varphi = k\int_0^t \alpha(z)dz$. If the medium has a homogeneous composition and density, the phase shift is simplified to $\Delta\varphi = kt\alpha$ (which is the classical Beer-Lambert law). Note that the refractive index is wavelength-dependent, making the computation of the phase shift more difficult for a polychromatic beam.

In addition, curved interfaces result in a weak scattering of the incoming collimated X-ray beam that yields interference patterns. This is at the origin of the phase-contrast denomination of this X-ray imaging technique. With the moderate distance between the object and the detector plane (the scintillator), the interferences only extend to a small region surrounding the interface, with typically only half a wavelength that simply highlights the interface location with a bright line. While this aspect may be useful as it leads to sharp edges and eases the identification of objects, even when many are overlapping, a direct inversion of Beer-Lambert law that ignores the presence of such interference patterns would result in strong biases. Weitkamp et al. 2011 developed an algorithm called ANKAphase to overcome this challenge. Using the raw radiograph image and the associated background, ANKAphase computes the phase-shift maps at each position of the radiograph and outputs an image of $\Delta\varphi(x,y)$ referred to as a phase map. In the following, the phase shift will be noted φ and referred to as the phase for simplicity. ANKAphase implies that the following hypotheses are satisfied

- The object consists of a single homogeneous material;
- The X-ray beam used is monochromatic;
- The distance L in between the object and the detector fulfills the near-field condition of Eq. 3.1, where d is the size of the smallest imaged object and λ is the wavelength of the X-ray beam.

$$L \ll d^2/\lambda \tag{3.1}$$

While the incoming beam used is not strictly monochromatic (more experimental details are given in Tolfts 2023), the energy of the photons is assumed to be $e_{photon} = 18.2$ keV, corresponding to a wavelength $\lambda_{photon} = 6.8 \times 10^{-5}$ nm. The last hypothesis constitutes a limitation to the resolution of the imaging technique: $d \gg 5.22 \times 10^{-1}$ μm, ten times smaller than the effective pixel size of the imaging system of 6.7 μm. The third hypothesis is therefore respected. In addition, Weitkamp et al. 2011 noted that respecting two out of three hypotheses is sufficient to yield accurate results.

In theory, the relationship between the phase map and the EPL is supposed to be a linear function with a single known coefficient and a zero y-intersect. The measurements biases and the slight deviations from the hypotheses of ANKAphase make this untrue in practice, and a linear relationship $\varphi = \alpha EPL + \beta$ as is assumed, where α and β depend on the sample and on the X-ray wavelength. To calibrate for these coefficients, conditions with a laminar liquid jet are captured. In this case, at a given distance x, the jet's cross-section is circular, and the thickness of liquid that the X-ray passes through, h, follows equation 3.2 along the transverse coordinate y:

$$h(y) = 2R\sqrt{1 - \left(\frac{y}{R}\right)^2} \tag{3.2}$$

This approach is illustrated in Fig. 3.5a), where the fit of a transverse phase profile yields a value of R, that can be compared to a direct measurement of the jet's radius from the radiograph. This process is then conducted for many x locations, at every time step, and for various liquid Reynolds numbers (within laminar conditions). Figure 3.5b) shows the time series of α and β for a given conditions and x location. While α appears to be stationary, β shows a decreasing trend with large temporal fluctuations. This could be explained by the heating of the scintillator throughout the movie. β acting as an offset for the phase, a natural metric to consider to explain the variations observed in the time series of β is the value of φ on the edges of the phase-retrieved image, where no liquid is found, acting as the background phase. For simplicity and a better implementation for spray conditions, this background phase is simply estimated as the minimum value of the phase profile $\varphi(y)$, for a given value of x and t, and written $\min_x(\varphi)$. Once normalized by this value, the temporal variations of β are mostly mitigated and are limited to a few standard deviations around the average value. In addition, the spatial variations are found to be negligible for α and β (when normalized instantaneously and locally by $\min_x(\varphi)$), and values are consistent within different conditions (not shown here for conciseness, but discussed in Tolfts 2023). In the following, $\alpha = 0.91$ mm^{-1}and $\beta = 1.12\min_x(\varphi)$ will be used to convert the phase maps into EPL maps.

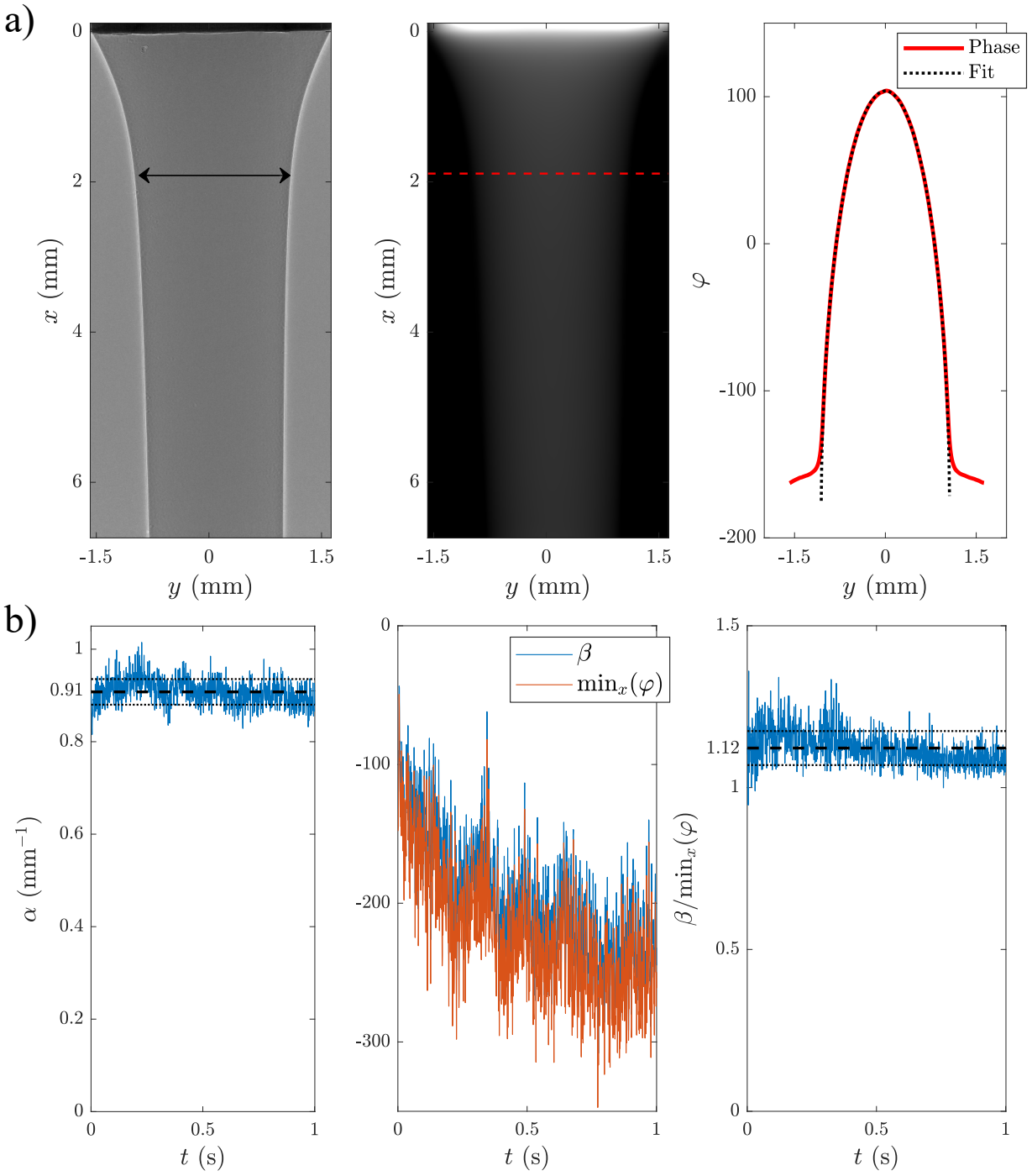

Figure 3.5: a) Normalized radiograph of the liquid jet, corresponding phase retrieved map obtained with ANKAphase, and transverse phase profile taken at the x location indicated by the dashed line. The fit of the phase profile ($r^2 = 0.9999$) yields a radius $R_{fit} = 1.06$ mm while a direct detection (black arrow) on the radiograph yields $R_{mes} = 1.045$ mm. b) Time series of the fitting coefficients α and β relating phase to EPL. $\min_x(\varphi)$ stands as the minimum value of φ on the pixel line found at a given x location, evaluated at each time step and for each longitudinal x. The dashed and dash-dotted lines indicate the average and average $\pm$ standard deviation (with respect to t) of the plotted quantity.

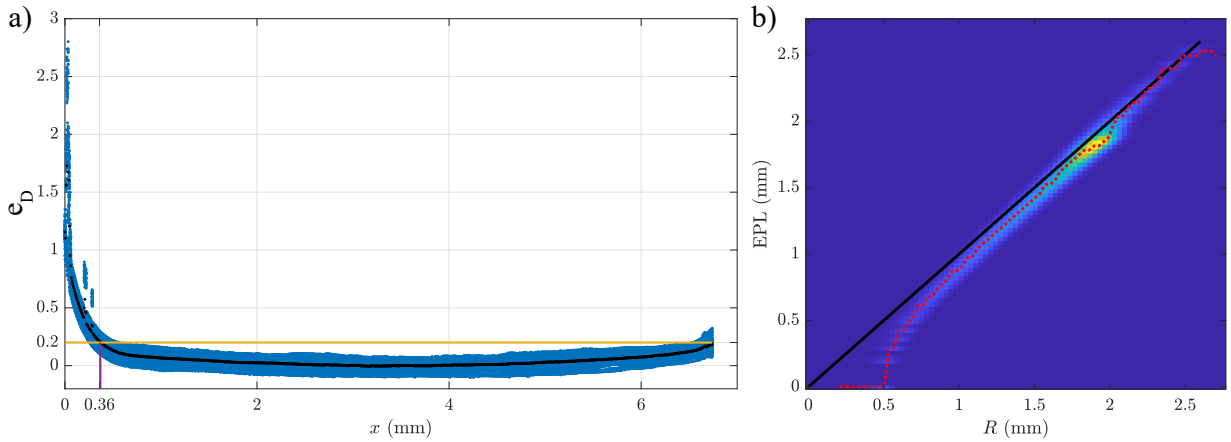

Figure 3.6: a) Relative error e_D between the measurement of the diameter of the liquid jet via determination of the EPL and the expected diameter D_{mes}, obtained through a longitudinal cut (along x) along the liquid jet. b) Joint probability density function of the calculated EPL and the actual local thicknesses (estimated from direct measurements and geometrical considerations). The maximum probability for each column is displayed in red.

It is important to point out that the aluminum nozzle is visible in the images. This means the first hypothesis of ANKAphase, stating the object consists of a single homogeneous material, is not fulfilled. Having aluminum in the field of view results in local variations of the phase map calculation, leading to an increase of the phase close to the injector, and biasing surrounding measurements of the equivalent path length. This is directly observable when estimating the relative error between the radius obtained from the calculated EPL and the direct measurement (Fig. 3.6a). The EPL is erroneous for $x < 0.36$ mm ($0.2d_l$), while it is always within 20% error otherwise. Locations located before this limit are ignored in any use of the EPL maps in what follows.

By using the direct measurements of the jet's radius on the radiograph, together with Eq. 3.2, a map of the jet thickness is computed within the liquid jet, to serve as a true value to estimate the error in the EPL map computation. Figure 3.6b) shows the resulting joint PDF. The measured EPL is close to the expected value of the liquid thickness on a wide range of liquid thicknesses (with a relative error lower than 20% for $R > 0.73$ mm, and lower than 10% for $R > 0.96$ mm) and starts to undervalue measurements for lower liquid thickness. Note that this assessment of the quality of the EPL measurement may be biased (toward larger errors) due to the lack of representation of small thickness in the comparison data set. Due to interferences caused by X-ray diffraction near curved interfaces (white edges around the liquid jet on the raw radiographs), some regions of the flow are not as well resolved. In spray formation measurements, these locations strongly fluctuate across time and space, and may not necessarily prevent measurements of smaller liquid thicknesses. However, in the current assessment, these regions only concern the

edge of the liquid columns, which stand as the only locations that present small thicknesses. Since this study has a strong focus on the liquid core, it does not present a strong issue, but it is a caveat worth resolving if one wants to study the small-scale structures of spray formation or the primary breakup populations.

3.5 Dynamics of the liquid crown

The instantaneous EPL maps are used to compute the time series of the center of mass of the liquid jet. Since liquid mass is already integrated along the beam direction (z) by the X-ray projection onto the sensor, the transverse motion of the liquid jet is analyzed by studying the center of mass along y, $Y_M(t)$. This means that the azimuthal motions are perceived as in-plane left-right motions. Figure 3.7 presents the time series and associated probability density functions. A condition per morphology was chosen to represent its dynamics, at increasing gas Weber number and for a fixed value of the liquid Reynolds number $Re_l = 780$. In addition, a condition with azimuthal momentum in the gas jet (swirl) is included, with $SR = 0.8$ and the other parameters kept constant, to discuss the effect of swirl on the motions of the unstable crown.

The time series and PDF appear roughly similar for the intact core, transitional, and crown regime. While the fluctuations seem to happen on faster timescales as We_g increases, their levels are the highest in the transitional regimes ($Y'_M = 0.026R_l$, versus approximately $0.02R_l$ for the two other cases). This may be due to the transitional nature of the regime where the morphology of the liquid core strongly varies in time, unlike the crown that is stabilized by the large-scale gas recirculation, and the intact core that remains only weakly perturbed in the vicinity of the nozzle's exit plane. Another explanation comes from the flapping of the liquid jet, which bears a clear signature on the motion of the liquid core (the temporal dynamics is discussed below, see Fig. 3.8), which, while its amplitude decreases with decreasing liquid core length (Kaczmarek et al. 2022), plays a large role in the fluctuations of Y_M unlike the case of the liquid crown, but in addition to small-scale fluctuations, that are barely present for the intact core. However, those variations are much smaller than the large deviations of the center of mass found in the unstable crown regime ($Y'_M = 0.056R_l$ without swirl, and $0.058R_l$ for a swirled unstable crown), whose bimodal PDF stands as a clear quantitative signature of this regime. Once again note that this left-right bimodal shape in this axisymmetric configuration, where the unstable crown is anchored along a portion of the liquid nozzle and moves along its circumference, is only caused by the projection along the beam direction, and highlights the fact that the center of mass is almost never centered on the nozzle's axis (low probability of having $Y_M = 0$, which is the situation created by the three other morphologies, where the jet is anchored along the whole periphery of the liquid nozzle). That shape can simply be modeled by geometrical arguments (Tolfts 2023), and the lack of symmetry here is due to a lack of data convergence. The difficulty in retaining

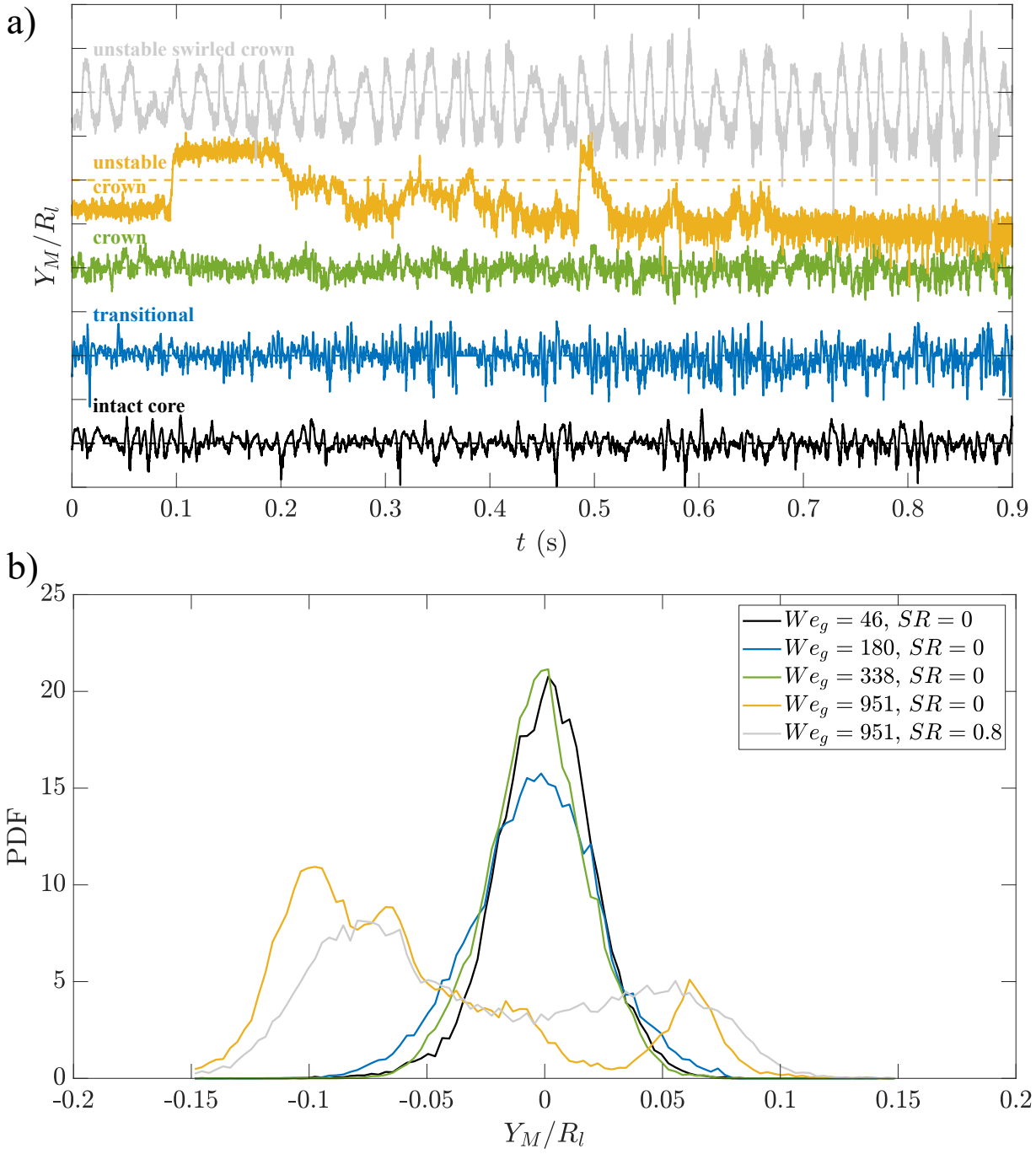

Figure 3.7: Time series (a) and probability density functions (b) of the center of mass of the liquid jet along y, normalized by the liquid nozzle outer radius, Y_M/R_l. The liquid Reynolds number is kept constant at $Re_l = 780$ and the gas Weber numbers is increased from $We_g = 46$ to 951 to span the four morphology of the liquid core. At the highest value, a condition with the same total gas flow rate, but with swirl in the gas jet at $SR = 0.8$ is also considered. The time series (a) are successively shifted by $0.2R_l$, but the ranges of variations of Y_M is visible in the PDF (b).

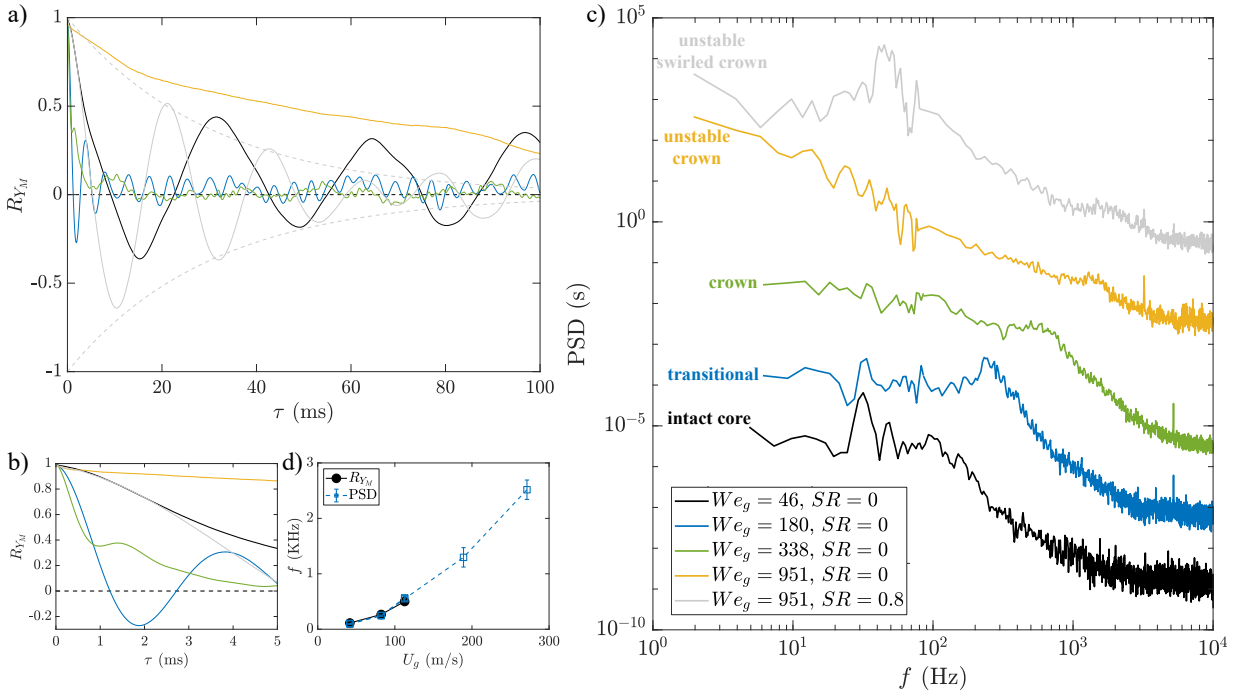

Figure 3.8: Auto-correlation functions (a, with zoom in b) and power spectral densities (c) of the liquid jet's center of mass Y_M/R_l dashed line b). The liquid Reynolds number is kept constant at $Re_l = 780$ and the gas Weber numbers is increased from $We_g = 46$ to 951 to span the four morphology of the liquid core. At the highest value, a condition with the same total gas flow rate, but with swirl in the gas jet at $SR = 0.8$ is also considered. The PSD are successively shifted by a factor 100, and are computed in two parts using the *pwelsh* method with two different sets of arguments to denoise the low and high-frequency range respectively. The dashed line in a) is the envelope obtained by fitting the function $\cos(t/2\pi f_{fit})\mathrm{e}^{-t/\tau_{fit}}$ for the swirled unstable crown case. d) Flapping frequency extracted from the PSD or auto-correlation function.

symmetries in the experimental measurements of such multistable systems is a well-documented challenge, that is very common in the general contexts of physics, chemistry, or biology (Kramers 1940; Van Kampen 1981), and has been many times reported in fluid mechanics with fluctuation-driven bi-stable systems (*e.g.,* Benzi 2005; Berhanu et al. 2007; Constable 2000; Grandemange, Gohlke, and Cadot 2013; Torre and Burguete 2007 as well as other particle-laden flows, Climent, Simonnet, and Magnaudet 2007; Djeridi et al. 1999; Machicoane et al. 2016; Machicoane and Volk 2021; Maxey 1987).

The changes highlighted here on the statistics of the liquid core center of mass through transitions in its morphology are also visible in its temporal dynamics. Figure 3.8 presents the auto-correlation functions and power spectral densities of Y_M. In the intact core and transitional regime, flapping dominates the temporal dynamics, marked by oscillations of the auto-correlation

functions and a peak on the power spectra, located within the plateau found in the low-to-moderate frequency. In the crown regime, flapping remains noticeable but is much weaker, since the flapping frequency is found within the high-frequency power-law decay that corresponds to the small-scale fluctuations. This corresponds to a trough and hump feature in the decay of the auto-correlation function. In the unstable crown regime, the erratic motion of the liquid core along the nozzle's circumference results in the emergence of long-time dynamics, highlighted by the power law found in the low-frequency range. This results in an auto-correlation function that retains correlated dynamics over very long times. The slight change of slope at short times (around 15 ms) highlights the small difference in scaling in the low and high-frequency range that is less noticeable on the PSD. The long-time dynamics of the unstable crown regime would require much longer acquisition to be further investigated, with for instance the extraction of residence times and their distributions.

The peak that corresponds to the flapping of the liquid jet is reported along the gas velocity in Fig. 3.8d) with error bars associated with the frequency resolution for the first three points (up to the crown regime), and to the broad nature of the peak found for higher gas Weber number. The points for the two highest velocities are in the unstable crown regime (PSD not shown here for $U_g = 271$ m/s, corresponding to $We_g = 1950$) are conditions where the flapping peak falls within the high-frequency range and associating a unique frequency become more challenging, so the width of the peak is given as error bars. The flapping frequency is also extracted from the oscillation period of the auto-correlation functions, only measurable for the first 3 points, which, as expected, agrees well with the frequencies from the PSD. The scaling of the flapping frequency with the gas velocity observed here seems to be slightly steeper than the linear relationship proposed by Delon, Cartellier, and Matas 2018.

When swirl is added to the gas jet, a strong periodicity is observed on the time series, which results in oscillations of the auto-correlation functions and a broad peak at low-frequency, centered around $f_{peak} = 49$ Hz. No signature of long-time dynamics is present, and this is confirmed by the auto-correlation functions, whose envelop follows a much faster decay than the one observed in the absence of gas swirl. This can be characterized by fitting R_{Y_M} by the function $\cos(t/2\pi f_{fit})\mathrm{e}^{-t/\tau_{fit}}$ up to $t = 50$ ms, which yield $f_{fit} = 47$ Hz and $\tau_{fit} = 30$ ms ($\pm\mathrm{e}^{-t/\tau_{fit}}$ is represented by dashed lines in Fig. 3.8a), while the first zero-crossing happens around 5 ms. Note that, for every condition presented here, the decorrelation of the liquid core center of mass is orders of magnitude slower than that of the liquid core length. When using the scaling law found for the liquid core length (Sec. 2.3.3), the correlation time scale for $We_g = 951$ is $\tau_c \simeq 0.14$ ms (obtained by integration, bringing the first-zero-crossing time to approximately 0.05 - 0.07 ms).

CHAPTER 4

Conclusion

Liquid core and fragmentation regimes

We performed high-speed back-lit imaging of the breakup of a liquid jet by a turbulent coaxial gas jet, over a wide range of liquid and gas Reynolds numbers, encompassing laminar and turbulent conditions of the liquid jet as well as different regimes of jet breakup. We focus on the liquid core, which is the portion of the liquid jet that is still hydraulically connected to the liquid nozzle. We report the statistics and temporal dynamics of its length (longitudinal extent of the liquid jet, noted L_B) and study its small and large-scale instabilities.

Using auto-correlation functions of the liquid core length, we showed that the correlation time τ_c scales linearly with Re_g^{-1}. In opposition, the statistics are observed to be governed by the gas-to-liquid dynamic pressure ratio M. The average and standard deviation of the liquid core length both follow a power law with M. In addition, we find the ratio of these two statistical moments $< L_B > /L_{B,STD}$ to be constant, effectively reducing the number of parameters needed to describe the statistics of L_B. The skewness on the other hand does not present a clear scaling with M but appears to have a non-monotonous evolution with the gas Reynolds number Re_g. Nonetheless, thanks to a representation of the distributions of L_B with skew-Gaussian functions, we can fully describe its statistics using only two parameters: the average and skewness of L_B. The skewness is found to be constant for high Re_g, therefore further reducing the description to a single parameter in that case.

We identified a change of behavior of the statistics and temporal dynamic of the liquid core length above and below the value of $Re_g = 33\,000$ (alternatively $We_g = 75$) (conditions at $Re_g < 33\,000$ show exponentially decaying auto-correlation functions and lower skewness whereas for conditions with $Re_g > 33\,000$ the decay is faster than an exponential and the skewness reaches an asymtotic value around 0.46. The proposed framework, studying the distributions, auto-correlation functions, and their transition, appears as a candidate for a quantitative tool to describe the transition in breakup regimes, from membrane breakup to fiber-type atomization.

Building upon this framework, we studied the associated scaling laws in the low gas velocity range for a fixed liquid Reynolds number $Re_l = 1200$ and found that the standard deviation

Onset of	Indicator
Non-axisymmetric Rayleigh-Plateau breakup	L'_B
Shear breakup	τ_0
Shear breakup with bags	No indicator found
Shear breakup with Kelvin-Helmholtz bags	$\langle L_B \rangle$, $\min(L_B)$, and flapping
Fiber-type atomization with bags	Skewness and auto-correlation functions of L_B
Fiber-type atomization without bags	Transport of interfacial perturbations

Table 4.1: Proposed quantitative indicator for the onset of the different fragmentation regimes identified for a liquid jet surrounded by a gas jet. $\langle L_B \rangle$, $\min(L_B)$, and L'_B are the average, minimum value and standard deviation of the liquid core length L_B, while τ_0 is its correlation time.

and the correlation time of the liquid core length present a unique power law with We_g and Re_g respectively (with exponents about -0.3 and -1) as soon as We_g is greater than the threshold found for non-axisymmetric Rayleigh-Plateau breakup and shear breakup respectively. The average and minimum value of L_B present different power laws in the low or high range of gas Weber numbers, and the change of behavior correspond to the onset of Kelvin-Helmholtz bags.

This sub-regime of the membrane regime (itself a category of shear breakup) was clearly identified as a major player in the transition from planar sinusoidal flapping (found to occur when bags are not present, or when they only occur at the tip of the jet, in the hook-like shape formed by the meandering of the liquid core), to more complex 3D motions that display elliptical mean flapping orbits. This study of the spatial characteristics of the large-scale instability of the liquid jet was possible thanks to two-view high-speed back-lit imaging, complementing the work done on the scaling of the flapping frequency by Delon, Cartellier, and Matas 2018.

At a smaller scale, the interfacial perturbations, that originate from the instabilities of the liquid-gas interface, were studied using Lagrangian tracking to study their transport as they are advected and stretched by the gas jet. The normalized spatial gradient of the perturbations' longitudinal velocity was shown to exhibit a change of scaling with Re_g, from a linear growth to a asymptotic value. This change occurs for $Re_g = 45\,000$ (alternatively $We_g = 190$, reached for $U_g = 77$ m/s) $Re_g = 45000$, $We_g = 190$, while the change of behavior of the statistics and temporal dynamics of L_B is at $Re_g = 33\,000$ (alternatively $We_g = 75$, reached for $U_g = 53$ m/s). While the latter corresponds to the onset of fiber-type atomization, this means that the transport of interfacial perturbation could indicate the disappearance of bags in the atomization process.

Table 4.1 summarizes the study of the liquid core length and instabilities by listing the quantitative indicators that best highlight the signature of the transitions among the fragmentation regimes. This in-depth study of the liquid core found no indicator for the onset of bags at the tip of the jet for shear breakup found no indicator in the behavior. They remain easily identifiable when one takes an interest in the onset of small droplets.

Towards high-speed sprays

Following the characterization of the liquid core dynamics and its link to fragmentation regimes, some exploratory work was conducted to investigate that behavior in high gas velocity conditions, targeting the high Weber number range typically found in aeronautical propulsion and approaching the range of aerospace applications.

Despite the wide range of operating parameters for which the breakup process can be studied using visible light, conditions with high gas velocities yield a dense two-phase flow which prevents proper identification of the liquid-gas interface. Synchrotron X-ray high-speed imaging was hence used to study the dense two-phase flow of the near-field of coaxial gas-assisted atomization at high gas velocities (up to Mach numbers of 0.95). Thanks to a tight sampling of the parameter space (102 operating conditions distributed on a parameter space with $19\,000 < Re_g < 200\,000$, alternatively $20 < We_g < 3000$, and $780 < Re_l < 4300$), a phase diagram of the morphology of the liquid core in the (Re_l, We_g) parameter space was established, reporting 4 morphologies for the breakup of the liquid core:

- The intact core regime, characterized by an intact central bulk whose surface is destabilized by ligaments and sheets of liquid (the term intact is used to express the fact that no gas reciculation is penetrating within the liquid core).
- The crown regime, where the liquid core is hollowed out by a large gas recirculation and ligaments are directly stripped on the edge of the liquid core.
- The transitional state between the intact core and the crown regime, where many small gas recirculations are observed in the liquid core.
- The unstable crown regime where the gas recirculation penetrates the liquid nozzle and pushes the liquid crown to a smaller region of the liquid nozzle (exiting through a smaller cross-section).

This showed for the first time that the unstable crown regime was reached for high values of M, without adding swirl in the gas jet, and demonstrated the existence of a transitional regime, occupying a wide region of the parameter space, between the intact core and crown regime. The previous study of Machicoane et al. 2019 only reported unstable crowns for conditions with gas swirl, since the slightly higher liquid Reynolds number value prevented to reach higher M values at a similar gas Weber number, and missed the transitional regime since only four values of the gas Weber number were explored (the focus being on swirl addition).

Considering a simple kinetic energy balance argument, the gas-to-liquid dynamic pressure ratio can be expected to capture the transitions between liquid core morphologies. This was

Onset of	Domain of existence
Fiber-type atomization with bags	$75 \leq We_g \leq 340$
• Intact core	unclear, but potentially $75 \leq We_g \leq 200$
• Transitional core	unclear, but potentially $200 \leq We_g \leq 340$ and $M \leq 55$
• Liquid crown	$55 \leq M \leq 180$
Fiber-type atomization without bags	$We_g \geq 340$
• Transitional core	unclear, but potentially $200 \leq We_g \leq 340$ and $M \leq 55$
• Liquid crown	$55 \leq M \leq 180$
• Unstable crown	$M \geq 180$

Table 4.2: Domain of existence of atomization regimes of high-speed sprays, with the associated morphology of the liquid core.

empirically verified on the phase diagram and successfully described the transitions from transitional to crown regimes and from crown to unstable crown regimes. While this argument should still hold for the transition between the intact core and the crown regimes, both regimes can be observed along iso-M lines (Fig. 3.4), and a threshold value as $We_g \simeq 200$ may seem more appropriate. It should however be taken with a grain of salt, since a limited amount of conditions was captured in the vicinity of this transition, as low values of M yield long liquid core lengths, which are not suited for synchrotron X-ray imaging considering the small beam diameter (half a dozen mm, while $\langle L_B \rangle \simeq 6 d_l$ over the $M = 11$ iso-line which is approximately the smallest value of M explored using X-ray, so at least 3 imaging windows are necessary to asynchronously capture the liquid core). Table 4.2 summarizes these findings. It should be noted that there is not apparent link with the transitions in liquid core morphology and in fragmentations regimes, since the former are separated by diagonals and the latter by verticals in the (Re_l, We_g) parameter space.

A framework to perform quantitative measurements of the liquid's mass spatial distribution from the X-ray radiographs was developed, adapted from a pre-existing post-processing method (Weitkamp et al. 2011). Despite evident limitations, the coordinate of the center of mass of the liquid core was measured on individual frames. The time series of this center of mass was shown to be a quantitative indicator of the transition from the crown to the unstable crown regime. The associated timescales of the motion of the unstable crown are orders of magnitude longer than that of the breakup of the liquid jet and gas swirl has a strong influence on the dynamics of the liquid core in the unstable crown regime. Up to now, the dynamics of mechanisms involved in the breakup of a liquid jet in coaxial gas-assisted atomization have been shown to depend on the properties of the gas jet only, here for instance with the liquid core correlation time, but also for other mechanisms of gas-assisted atomization (Delon, Cartellier, and Matas 2018; Matas, Delon, and Cartellier 2018; Matas et al. 2015; Raynal 1997). However, the transition to the unstable crown regime was shown to be triggered by variations of M, suggesting that the liquid velocity at injection has a strong influence on the stability of the liquid core, and therefore influences the

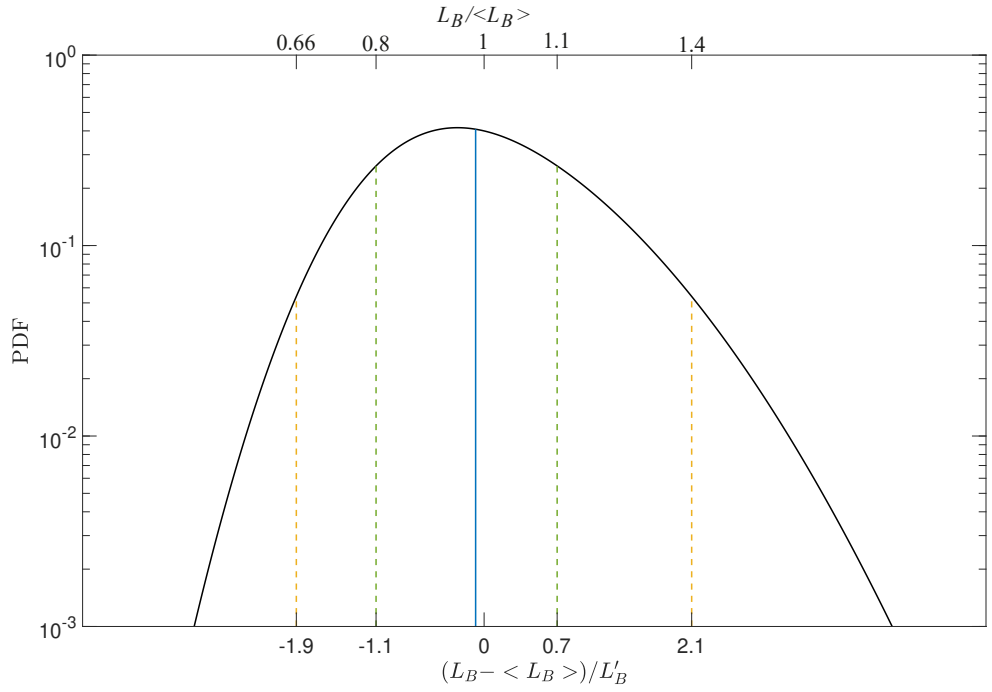

Figure 4.1: Skew Gaussian distribution of the normalized and centered liquid core length for $Re_g > 33\,000$. The solid blue line indicates the median, found at $\tilde{L}_B = 0.08$, which corresponds to $L_B = 0.98\,\langle L_B \rangle$. The green and yellow dashed lines respectively highlight the range of liquid core length values containing 64.2 and 95% of the distribution. The correspondence of the indicated values displayed for $\tilde{L}_B$ (-1.9, -1.1, 0, 0.7, and 2.1) in term of $L_B/\langle L_B \rangle$ are 0.66, 0.8, 1, 1.1, and 1.4 when using the constant value of the ratio $L'_B/\langle L_B \rangle$.

associated dynamics.

Practical outcomes

We list below some practical outcomes of the results presented here, for applications or in other fundamental work.

- The knowledge of the scaling laws of the timescale and statistical moments of the liquid core length with operating parameters results in an increase of the predictive power of that metric. Since most engineering applications are found at moderate to high gas velocity, since membrane breakup as a sole fragmentation mechanism is typically detrimental as the bag's rims result in very large drops, one can assume that $Re_g > 33\,000$. In that case, the skewness reached its asymptotic value, and the distribution of L_B is sketched in Fig.

4.1. Combined with a constant ratio of standard deviation over average value, the statistics of L_B are fully parametric by its average value, a sole function of M. This means that the range of value explored by the liquid core length reached in a given application can all be an output of a very simple model. The fact that the results can all be expressed in terms of $\langle L_B \rangle$ makes its use trivial since accurate correlations of the average liquid core length have been available for decades. Figure 4.1 displays the range that will be encountered over a 64.2% probability as an example: $-1.1 < \tilde{L}_B < 0.7$, while taking ± 1 standard deviation around the mean corresponds here to 69% of the values. This range can be expressed as $0.8\langle L_B \rangle < L_B < 1.1\langle L_B \rangle$. Similarly, 95% of the values will be found in the range $0.66\langle L_B \rangle < L_B < 1.4\langle L_B \rangle$. In addition, the timescale associated with these variations of the liquid core length can also be predicted from the operating parameters, using the relationship $\tau_c \sim 16.3/Re_g$ (valid from the onset of shear breakup and up to high-speed sprays).

- The framework proposed here, which uses the statistics and temporal dynamics of the liquid core length to determine changes in scaling laws and deduce quantitatively changes in fragmentation regime in relationship to operating parameters may be of some use in certain applications (to ensure membrane breakup is not explored in any circumstances for instance), but it may be of more interest to the fragmentation community. It could benefit to be applied in other coaxial atomization experiments, possibly with different fluids, and be complemented with other techniques (as was the case with the analyses of the instabilities of the liquid core), and would be interesting to extent as well as to other atomization configurations.

- The study of the morphology of the liquid core in high-speed two-fluid coaxial atomization offers a refined mapping of the phase diagram for the atomization community, which can allow the investigation of the consequences of such dynamics on the subsequent mechanisms in the spray formation process. In addition, furthering the understanding of the origin of these changes in morphologies and behaviors could help to clearly identify the relevant non-dimensional groups governing coaxial atomization.

- While extracting quantitative measurements have been tackled for a while now in several aspects of multiphase flows (*e.g.,* extracting void fraction maps in cavitation, Coutier-Delgosha et al. 2007; Ganesh, Mäkiharju, and Ceccio 2016; Khlifa et al. 2017; Maurice et al. 2021), its implementation for two-fluid atomization seems to still be work in progress. This may come from the very large number of small-scale interfaces densely found in the close vicinity of the liquid core and the unbounded nature of the flow (that prevents simple calibration of the equivalent liquid length). The work presented here is a first step in that direction, which can be improved in future studies and benefit from other X-ray users in multiphase flows.

Perspectives and future work

- The multiscale nature of spray formation typically prevents using a single approach to study every underlying mechanism of the fragmentation cascade. The liquid core length cannot be sufficient to fully describe gas-assisted atomization, in particular at high Weber numbers. Future work could hence encompass for instance the study of the signature of the change of atomization regimes and the onset of liquid turbulence highlighted here on other mechanisms, *e.g.,* flapping instability, interfacial instabilities, breakup processes, and up to the droplet populations in the spray. For instance, the work conducted on the instability of the liquid core and of its changes in behaviors in the low to moderate gas Weber number range was conducted only for a fixed liquid Reynolds number $Re_l = 1200$. Future investigations considering variations of the liquid exit velocity would help to confirm the results and to properly identify the relevant non-dimensionless groups. In addition, no investigation of secondary breakup processes and of the resulting droplet size in the spray was conducted so far. Finally, confirming the changes of behaviors, that were observed here by varying the velocities of the fluids, but through modifications of the properties of the fluids as well would be crucial to validate (or invalidate) the non-dimensional groups that were proposed here as governing parameters.

- Note that finding quantitative indicators for the onset of bags in the shear breakup regime as well as for the disappearance of bags in fiber-type atomization remains an open question. No clue was found so far for the former, and the change in scaling of the transport of the interfacial perturbation may be an indicator for the latter. However, this remains to be confirmed, as Ricard et al. 2021 proposed a thresholds value of $We_g = 190$, while the qualitative observation of the disappearance of bag in fiber-type atomization is observed for $We_g = 320$ by Tolfts, Deplus, and Machicoane 2023. While the work was not conducted in the same nozzle, with slight changes in exit diameters that may play or role since basing the Weber number on the inner liquid diameter d_l is a proxy that may not be suitable, and with fluid properties that may slightly differ, this potential finding deserves further studies to be confirmed.

- Further investigations, at higher temporal and spatial resolutions, for larger gas-to-liquid dynamic pressure ratios, should be conducted to determine what is the evolution of the flapping shape from bag breakup to fiber-type atomization. Measurements of the droplet population in the far-field throughout the cross-section of the spray should be considered to assess the spatial heterogeneities in the presence of non-axisymmetric flapping. An additional open question is the origin and potential reproducibility of the preferential flapping direction. Note that the exhibited preferential direction is observed to be different at different operating conditions (Kaczmarek et al. 2022). Besides consequences on the far-field spray statistics, this could be important to evaluate real-time spray features, such as is done when implementing atomization feedback control (Osuna-Orozco et al. 2019, 2020).

- The study of flapping for high-speed sprays may be well suited for future synchrotron X-ray imaging experiments. Similarly, complementary studies at high gas Reynolds numbers, in the unstable crown regime of the liquid core, as well as transitional and turbulent regimes of the liquid jet would enable a more complete understanding and modeling of the interfacial advection velocity and, ultimately, atomization mechanisms. This work could help complement the study of the morphology of the liquid core, and particularly of its dynamics, as a function of Re_l, We_g, and SR.

- The technique introduced in this manuscript to retrieve liquid mass distributions from radiographs showed some promising results, despite its limitations. To improve this analysis technique, a few key points that could be improved in future work have been identified. The X-ray beam production had a periodic cutoff during the experiments. With the exposure time of the camera set to a different (but close) value than the time between two cutoffs, fluctuations in the background intensity are observed from one frame to another. Even though they were partially taken into account, these fluctuations could have been avoided if the acquisition parameter of the camera was synchronized with the beam production. A different way of taking these fluctuations into account could be to have a calibration object on all the images. The calibration object could then be used to correct spatial and temporal changes in intensity. Before retrieving the EPL maps, ANKAphase conducts a flat-field correction of each image which consists of dividing each frame by an averaged background movie (a movie with nothing on the path of the X-ray beam). ANKAphase proposes to use two background movies (one before and one after the movie being analyzed), which should be used to best take into account the slow drift of the intensity of the X-ray beam throughout time. In addition, taking background on the same duration as the movies would be much better, to account for the variation of the intensity along the heating of the scintillator. Similarly, the entirety of the acquisition duration should be systematically saved for this purpose, so that the $t = 0$ of all movies rigorously and reproducibly corresponds to the start of the heat load on the crystal. Finally, the computation of the EPL map conducted by ANKAphase appears to be corrupted by the presence of aluminum within the radiographs. This can easily be fixed by artificially removing the nozzle during the post-processing. Implementing these strategies could highly improve the quality of the radiographs and EPL maps, and could help greatly in their analyses, for instance, to retrieve the liquid core length and study the interfacial perturbations for high-speed sprays.

- The study of the fragmentation mechanisms in the near-field of two-fluid coaxial atomization led to several findings that are assumed to have consequences on the remaining spray formation processes and hence affect the resulting droplet statistics (*e.g.,* size and spatiotemporal distributions). Conducting droplet measurements in the far-field, for instance using a phase Doppler interferometer, would be interesting in particular in relation to the following aspects:

  - While the presence of membrane breakup when fiber-type atomization is also partic-

ipating to the fragmentation process may not leave a clear signature in the near-field and its contribution their remain hard to quantify, this situation is very different in the far-field, especially when analyzing the droplet size probability density functions (*i.e.,* droplet counts, and not volume). This could help confirm the domain of existence of membrane breakup and try and isolate its contribution to the spray characteristics and quantify it with respect to other mechanics (*e.g.,* fiber shedding, flapping).

  - Measurements of the droplet population in the far-field throughout the cross-section of the spray (or at least in two orthogonal directions) should be considered to assess the spatial heterogeneities in the presence of non-axisymmetric flapping. This will help assess quantitatively the measurement biases in droplet characteristic sizes and liquid flux when only one direction is measured and planar or ellipsoidal flapping occurs (the biases are expected to strongly depend on the angle between the measurement and flapping axis).
  - Similarly, the signature of the unstable crown in the far-field of the spray in potential inhomogeneities or temporal dynamics should be explored.

- Finally, the previous perspectives require the study of the gas flow topologies around primary breakup events. A first step consist in characterizing the gas flow in the absence of liquid, which was done using hotwire anemometry (Fig. 4.2). The turbulent annular gas jet properties are the ones of a round jet as early as $x \geq 5d_g$, with for instance self-similar radial profiles of mean longitudinal velocity (Pope 2000). At the exit of the atomizer, the inner boundary of the gas jet invades the region where the liquid jet is found faster than the slowdown of the jet due to entrainment. This means that the characteristic velocity in the vicinity of the liquid jet is U_g, the mean exit velocity. When probing the centerline velocity from the nozzle exit to the far field, the initial top-hat nature of the radial profiles results in an increase to a maximum at $x_{max} = 2.8d_g$, followed by a $1/x$ decrease. When using the mean liquid core length as the large scale of the near-field, one notices that the maximum values reached (Fig. 2.4, in the case of high liquid Reynolds number values) are at most $60d_l = 12d_g$, where the centerline velocity is still $0.5U_g$. In addition, in most cases, with low to moderate liquid Reynolds numbers, primary breakup is found to occur within the potential core of the gas jet.

  Further characterization of the gas jet, using particle image velocimetry for instance to study radial components, spatial correlations, and swirled jets, would be required to complete this picture. Besides, the gas flow topology is assumed to change drastically around the primary breakup events between the different morphologies of the liquid jet. This would require statistical analyses of the dynamics of the liquid structures using X-ray (and potentially of the local flow velocity inferred through the imperfect proxy of detached droplets) but a few characteristics pictures are sketched in Fig. 4.3. The well-documented case of co-flowing streams is expected to differ drastically from the case of a liquid crown due to the presence of gas recirculations that could result in strong gas velocity gradients

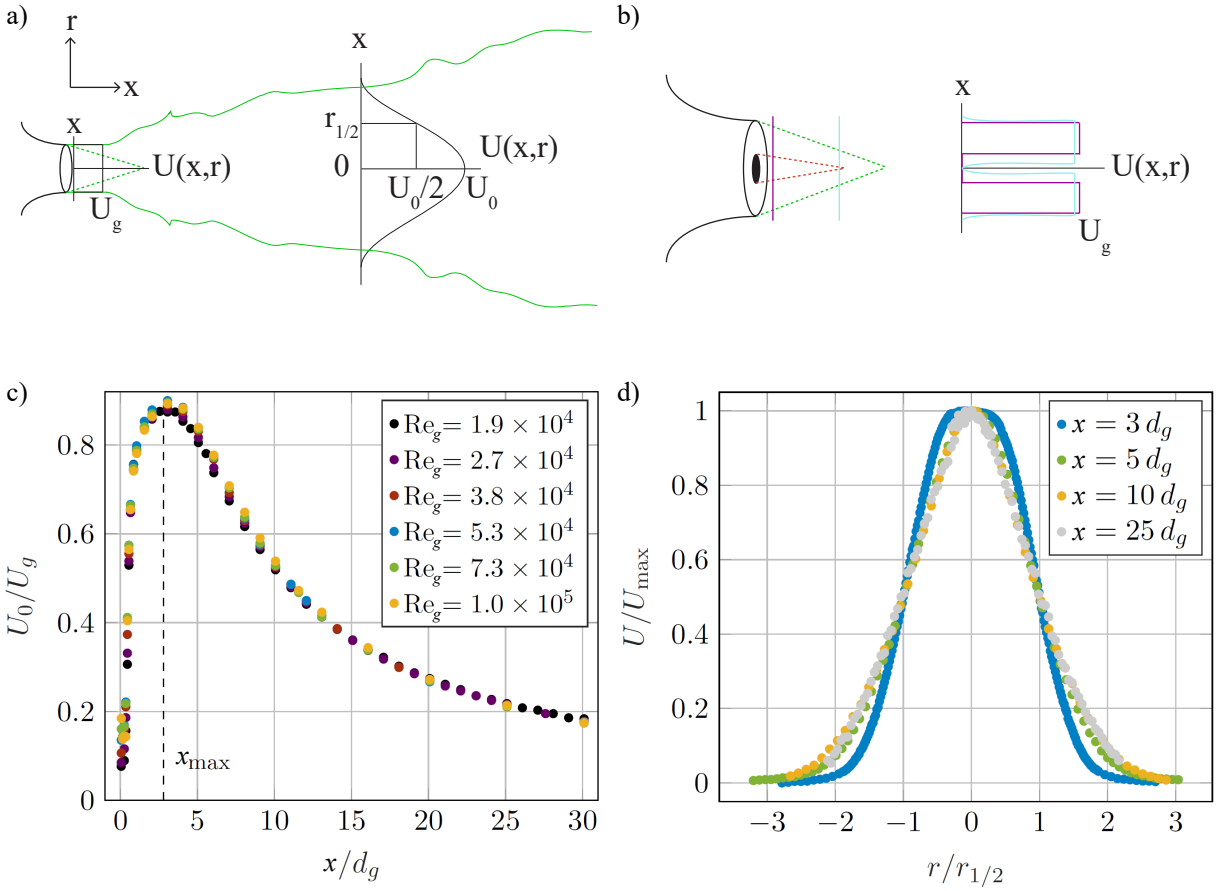

Figure 4.2: a) Schematics of a turbulent round jet, defining the centerline velocity U_0 and half-width $r_{1/2}$ of the radial profile of the mean longitudinal velocity $U(x,r)$. The transition from top-hat to self-similar profile is highlighted with the potential core in dashed lines. b) In the case of an annular gas jet, the inner boundary layers meet before the potential core vanishes, leading to a transition from a dual top-hat, to a single rounded hump, followed by the self-similar profiles. c-d) Centerline velocity at various gas Reynolds numbers and radial profiles for $Re_g = 1.9 \times 10^4$ at increasing downstream distances.

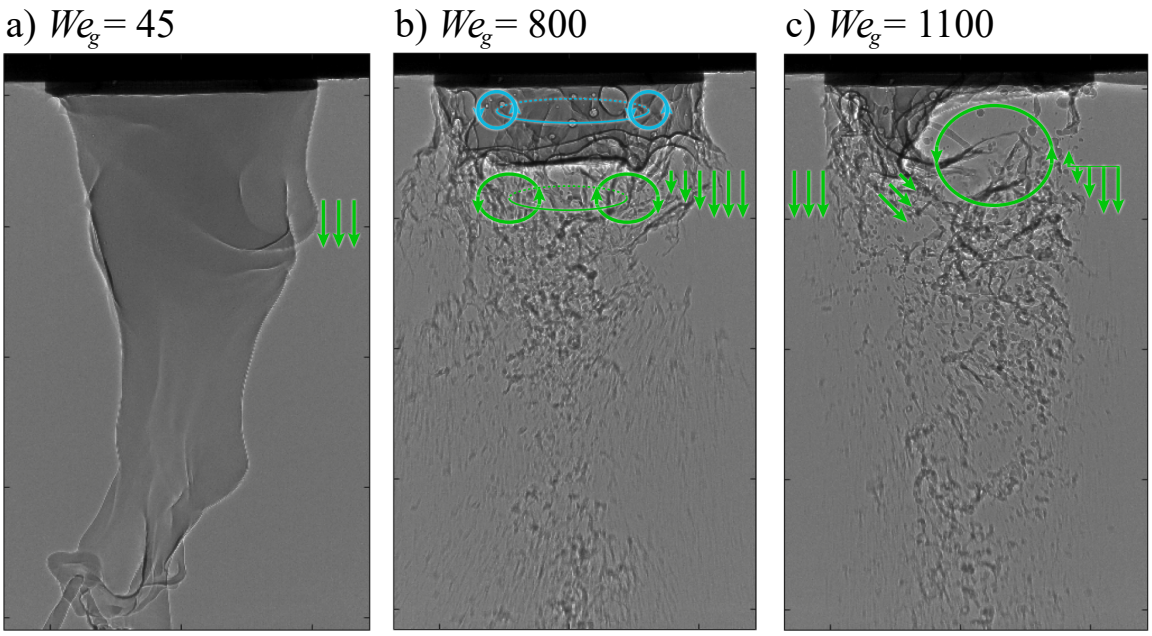

Figure 4.3: Schematics of the expected gas flow profiles around breakup regions for increasing gas Weber number in the intact core (a), crown (b), and unstable crown (c) regimes. The very stable bubbles observed in the crown regime are thought to be trapped in recirculating regions of the liquid jet that are also tentatively sketched.

around ligaments. In the case of an unstable crown, it is likely that, in addition to ligaments stretched by accelerating/curving flows, breakup in counterflows can occur as well (right part of Fig. 4.3c). In addition to changes in large-scale flow topology (from shear-driven instabilities to complex 3D structures responsible for breakup), the turbulent nature of the gas flow is also expected to change drastically between the different configurations. Since for intact core regimes primary breakup mostly occurs within the potential core of the gas jet, a low turbulence intensity (typically 1%) is found, while when gas recirculations are present in the crown and unstable crown regimes, the fast-paced overturning dynamics observed suggest a high turbulent intensity (probably in the neighborhood of the 15-20% found in wakes). Further work on the role of the flow topology (from longitudinal flows to stagnation point turbulence) could help decipher the involved breakup mechanisms involved in such situations. Beyond the possible role of a higher local turbulence intensity played on instabilities and breakup (Jiang and Ling 2021; Matas et al. 2015), the presence of pockets of gas in the liquid jet (*e.g.,* Fig. 4.3b), whether bubbles within the bulk of the liquid jet or holes nucleated in thin liquid films, poses many questions on their origin(s) and consequences on spray formation as well as what parameters drive their presence and numbers. Investigating the potential analogy to the dynamics of hole nucleation in the two-phase planer mixing layer case (Ling et al. 2017) and how this relates to ligament formation in the crown regime appears of great interest. Furthermore, in the crown regime in particular, bubbles are observed to remain remarkably stable (long lifetime and fluctuating around a stable position, without being advected downstream). This points towards the potential for recirculations being present within the liquid jet as well (Fig. 4.3b), as they would be able to entrap air bubbles in their core.

Note that studying such breakup configurations would also further our understanding of the fragmentation of a liquid jet by a swirled gas jet, even at moderate gas velocities. The swirled turbulent gas jet experiences a vortex breakdown instability which stabilizes a recirculation downstream of the liquid jet. In addition, even the formation of interfacial perturbation through Kelvin-Helmholtz instabilities, and their transport/deformation dynamics are expected to differ in such a case from what occurs when the gas jet only imposes a longitudinal shear (Fig. 4.3a), since an additional azimuthal component is present. Beyond an in-depth study of the existing X-ray imaging, such understanding may require dual (simultaneous) measurements of breakup (using back-lit or X-ray imaging) and particle image velocimetry. Due to the complexity of such setups, coming notably from the difficulty in seeding the gas flow and from the many reflections coming from the corrugated liquid interfaces, such ventures should probably first try and address moderate gas velocity cases.

Bibliography

Aliseda, A. and T. J. Heindel (2021). "X-ray flow visualization in multiphase flows." In: *Annual Review of Fluid Mechanics* 53, pp. 543–567 (cit. on p. 37).

Aliseda, A., E. Hopfinger, J. C. Lasheras, D. Kremer, A Berchielli, and E. Connolly (2008). "Atomization of viscous and non-Newtonian liquids by a coaxial, high-speed gas jet. Experiments and droplet size modeling." In: *International Journal of Multiphase Flow* 34.2, pp. 161–175 (cit. on pp. 2, 4, 5, 8).

Benzi, R. (2005). "Flow Reversal in a Simple Dynamical Model of Turbulence." In: *Physical Review Letters* 95.2, p. 024502 (cit. on p. 50).

Berhanu, M., R. Monchaux, S. Fauve, N. Mordant, F. Pétrélis, A. Chiffaudel, F. Daviaud, B. Dubrulle, L. Marié, F. Ravelet, M. Bourgoin, P. Odier, J.-F. Pinton, and R. Volk (2007). "Magnetic field reversals in an experimental turbulent dynamo." In: *EPL (Europhysics Letters)* 77.5, p. 59001 (cit. on p. 50).

Bothell, J. K., N. Machicoane, D. Li, T. B. Morgan, A. Aliseda, A. L. Kastengren, and T. J. Heindel (2020). "Comparison of X-ray and optical measurements in the near-field of an optically dense coaxial air-assisted atomizer." In: *International Journal of Multiphase Flow*, p. 103219 (cit. on p. 38).

Cai, W., C. F. Powell, Y. Yue, S. Narayanan, J. Wang, M. W. Tate, M. J. Renzi, A. Ercan, E. Fontes, and S. M. Gruner (2003). "Quantitative analysis of highly transient fuel sprays by time-resolved x-radiography." In: *Applied Physics Letters* 83.8, pp. 1671–1673 (cit. on p. 38).

Charalampous, G., C. Hadjiyiannis, and Y. Hardalupas (2019). "Proper orthogonal decomposition of primary breakup and spray in co-axial airblast atomizers." In: *Physics of Fluids* 31.4, p. 043304 (cit. on pp. 5, 10).

Charalampous, G., Y. Hardalupas, and A. Taylor (2009). "Structure of the continuous liquid jet core during coaxial air-blast atomisation." In: *International Journal of Spray and Combustion Dynamics* 1.4, pp. 389–415 (cit. on pp. 3, 8).

Chigier, N. and Z. Farago (1992). "Morphological classification of disintegration of round liquid jets in a coaxial air stream." In: *Atomization and sprays* 2.2 (cit. on p. 8).

Chiodi, R. M. (2020). "Advancement of numerical methods for simulating primary atomization." PhD thesis (cit. on p. 6).

Clanet, C. and J. C. Lasheras (1999). "Transition from dripping to jetting." In: *Journal of fluid mechanics* 383, pp. 307–326 (cit. on p. 7).

Climent, E., M. Simonnet, and J. Magnaudet (2007). "Preferential accumulation of bubbles in Couette-Taylor flow patterns." In: *Physics of Fluids (1994-present)* 19.8, 083301, pp. – (cit. on p. 50).

Constable, C. (2000). "On rates of occurrence of geomagnetic reversals." In: *Physics of the Earth and Planetary Interiors* 118, pp. 181–193 (cit. on p. 50).

Coutier-Delgosha, O., B Stutz, A. Vabre, and S. Legoupil (2007). "Analysis of cavitating flow structure by experimental and numerical investigations." In: *Journal of Fluid Mechanics* 578, pp. 171–222 (cit. on p. 58).

Delon, A., A. Cartellier, and J.-P. Matas (2018). "Flapping instability of a liquid jet." In: *Physical Review Fluids* 3.4, p. 043901 (cit. on pp. 2, 3, 8, 27, 29, 51, 54, 56).

Dimotakis, P. E. (2000). "The mixing transition in turbulent flows." In: *Journal of Fluid Mechanics* 409, pp. 69–98 (cit. on p. 20).

Djeridi, H., J.-F. Fave, J.-Y. Billard, and D. Fruman (1999). "Bubble capture and migration in Couette–Taylor flow." In: *Experiments in fluids* 26.3, pp. 233–239 (cit. on p. 50).

Dumouchel, C. (2008). "On the experimental investigation on primary atomization of liquid streams." In: *Experiments in fluids* 45.3, pp. 371–422 (cit. on p. 7).

Eroglu, H., N. Chigier, and Z. Farago (1991). "Coaxial atomizer liquid intact lengths." In: *Physics of Fluids A: Fluid Dynamics* 3.2, pp. 303–308 (cit. on pp. 3, 8).

Fong, K. O., X. Xue, R Osuna-Orozco, and A Aliseda (2022). "Two-fluid coaxial atomization in a high-pressure environment." In: *Journal of Fluid Mechanics* 946 (cit. on p. 10).

Fuster, D., J.-P. Matas, S. Marty, S. Popinet, J. Hoepffner, A. Cartellier, and S. Zaleski (2013). "Instability regimes in the primary breakup region of planar coflowing sheets." In: *Journal of Fluid Mechanics* 736, pp. 150–176 (cit. on pp. 4, 27, 33).

Ganesh, H., S. A. Mäkiharju, and S. L. Ceccio (2016). "Bubbly shock propagation as a mechanism for sheet-to-cloud transition of partial cavities." In: *Journal of Fluid Mechanics* 802, pp. 37–78 (cit. on p. 58).

Gorokhovski, M. and M. Herrmann (2008). "Modeling primary atomization." In: *Annu. Rev. Fluid Mech.* 40, pp. 343–366 (cit. on p. 2).

Grandemange, M., M. Gohlke, and O. Cadot (2013). "Turbulent wake past a three-dimensional blunt body. Part 1. Global modes and bi-stability." In: *Journal of Fluid Mechanics* 722, pp. 51–84 (cit. on pp. 39, 50).

Gutteridge, A. (2019). "An analysis of liquid jet instabilities formed from coaxial air-blast atomization of viscous fuels." University of Sydney (cit. on pp. 32, 33).

Hopfinger, E. and J. Lasheras (1996). "Explosive breakup of a liquid jet by a swirling coaxial gas jet." In: *Physics of Fluids* 8.7, pp. 1696–1698 (cit. on p. 5).

Huck, P., R Osuna-Orozco, N. Machicoane, and A Aliseda (2022). "Spray dispersion regimes following atomization in a turbulent co-axial gas jet." In: *Journal of Fluid Mechanics* 932 (cit. on pp. 7, 10).

Jiang, D and Y Ling (2021). "Impact of inlet gas turbulence on the formation, development and breakup of interfacial waves in a two-phase mixing layer." In: *Journal of Fluid Mechanics* 921, A15 (cit. on pp. 5, 64).

Jiang, D., Y. Ling, G. Tryggvason, and S. Zaleski (2019). "Impact of inlet gas turbulent intensity on the characteristics of droplets generated in airblast atomization." In: *AIAA Aviation 2019 Forum*, p. 3721 (cit. on p. 20).

Josserand, C. and S. T. Thoroddsen (2016). "Drop impact on a solid surface." In: *Annual review of fluid mechanics* 48, pp. 365–391 (cit. on p. 2).

Juniper, M. P. and S. M. Candel (2003). "The stability of ducted compound flows and consequences for the geometry of coaxial injectors." In: *Journal of Fluid Mechanics* 482, pp. 257–269 (cit. on p. 8).

Kaczmarek, M., R. Osuna-Orozco, P. D. Huck, A. Aliseda, and N. Machicoane (2022). "Spatial characterization of the flapping instability of a laminar liquid jet fragmented by a swirled gas co-flow." In: *International Journal of Multiphase Flow* 152, p. 104056 (cit. on pp. 3, 8, 10, 16, 27, 31, 48, 59).

Kastengren, A., C. F. Powell, D. Arms, E. M. Dufresne, H. Gibson, and J. Wang (2012). "The 7BM beamline at the APS: a facility for time-resolved fluid dynamics measurements." In: *Journal of synchrotron radiation* 19.4, pp. 654–657 (cit. on p. 38).

Kastengren, A. L., C. F. Powell, D. Arms, E. M. Dufresne, and J. Wang (2010). "Spray diagnostics at the advanced photon source 7-bm beamline." In: *ILASS Americas, 22nd annual conference on liquid atomization and spray systems, Cincinnati, OH* (cit. on p. 38).

Khlifa, I., A. Vabre, M. Hočevar, K. Fezzaa, S. Fuzier, O. Roussette, and O. Coutier-Delgosha (2017). "Fast X-ray imaging of cavitating flows." In: *Experiments in fluids* 58, pp. 1–22 (cit. on p. 58).

Kim, D. and P. Moin (2020). "Subgrid-scale capillary breakup model for liquid jet atomization." In: *Combustion Science and Technology* 192.7, pp. 1334–1357 (cit. on p. 6).

Kourmatzis, A and A. Masri (2015). "Air-assisted atomization of liquid jets in varying levels of turbulence." In: *Journal of Fluid Mechanics* 764, pp. 95–132 (cit. on p. 5).

Kramers, H. A. (1940). "Brownian motion in a field of force and the diffusion model of chemical reactions." In: *Physica* 7.4, pp. 284–304 (cit. on p. 50).

Kumar, A. and S. Sahu (2018a). "Liquid jet breakup unsteadiness in a coaxial air-blast atomizer." In: *International Journal of Spray and Combustion Dynamics* 10.3, pp. 211–230 (cit. on p. 10).

— (2018b). "Optical visualization and measurement of liquid jet core in a coaxial atomizer with annular swirling air." In: *Journal of Flow Visualization and Image Processing* 25.3-4 (cit. on p. 5).

— (2020). "Influence of nozzle geometry on primary and large-scale instabilities in coaxial injectors." In: *Chemical Engineering Science* 221, p. 115694 (cit. on pp. 3, 8, 14).

Ladam, Y, P.-E. Wolf, P Thibault, and L Puech (2001). "Light scattering by a liquid-gas helium spray." In: *The European Physical Journal-Applied Physics* 14.2, pp. 137–141 (cit. on p. 37).

Ladam, Y. (2000). "Atomisation et évaporation dans un jet mixte hélium liquide/hélium gazeux." PhD thesis. Université Joseph-Fourier-Grenoble I (cit. on p. 37).

Lallart, A. (2019). "Ultra cleanliness: microdroplets with nanoparticles." PhD thesis. Université Grenoble Alpes (cit. on p. 2).

Lasheras, J. C. and E. Hopfinger (2000). "Liquid jet instability and atomization in a coaxial gas stream." In: *Annual review of fluid mechanics* 32.1, pp. 275–308 (cit. on pp. 1, 8, 10, 21, 22, 24–26, 31).

Leroux, B., O. Delabroy, and F. Lacas (2007). "Experimental study of coaxial atomizers scaling. Part I: dense core zone." In: *Atomization and Sprays* 17.5 (cit. on pp. 8, 10, 14).

Li, D., J. K. Bothell, T. B. Morgan, N. Machicoane, A. Aliseda, A. L. Kastengren, and T. J. Heindel (2019). "Time-averaged spray analysis in the near-field region using broadband and narrowband X-ray measurements." In: *Atomization and Sprays* 29.4 (cit. on p. 38).

Ling, Y, D. Fuster, G Tryggvason, and S Zaleski (2019). "A two-phase mixing layer between parallel gas and liquid streams: multiphase turbulence statistics and influence of interfacial instability." In: *Journal of Fluid Mechanics* 859, pp. 268–307 (cit. on p. 27).

Ling, Y., D. Fuster, S. Zaleski, and G. Tryggvason (2017). "Spray formation in a quasiplanar gas-liquid mixing layer at moderate density ratios: a numerical closeup." In: *Physical Review Fluids* 2.1, p. 014005 (cit. on pp. 6, 64).

Ling, Y., S. Zaleski, and R. Scardovelli (2015). "Multiscale simulation of atomization with small droplets represented by a Lagrangian point-particle model." In: *International Journal of Multiphase Flow* 76, pp. 122–143 (cit. on p. 6).

Liu, Y., X. Sun, V. Sethi, D. Nalianda, Y.-G. Li, and L. Wang (2017). "Review of modern low emissions combustion technologies for aero gas turbine engines." In: *Progress in Aerospace Sciences* 94, pp. 12–45 (cit. on p. 2).

Machicoane, N., M. López-Caballero, L. Fiabane, J.-F. Pinton, M. Bourgoin, J. Burguete, and R. Volk (2016). "Stochastic dynamics of particles trapped in turbulent flows." In: *Phys. Rev. E* 93 (2), p. 023118 (cit. on p. 50).

Machicoane, N., J. K. Bothell, D. Li, T. B. Morgan, T. J. Heindel, A. L. Kastengren, and A. Aliseda (2019). "Synchrotron radiography characterization of the liquid core dynamics in a canonical two-fluid coaxial atomizer." In: *International Journal of Multiphase Flow* 115, pp. 1–8 (cit. on pp. 3, 11, 38, 41, 55).

Machicoane, N., R. Osuna-Orozco, and A. Aliseda (2023). "Regimes of the length of a laminar liquid jet fragmented by a gas co-flow." In: *International Journal of Multiphase Flow* 165, p. 104475 (cit. on pp. 10, 22).

Machicoane, N., G. Ricard, R. Osuna-Orozco, P. D. Huck, and A. Aliseda (2020). "Influence of steady and oscillating swirl on the near-field spray characteristics in a two-fluid coaxial atomizer." In: *International Journal of Multiphase Flow* 129, p. 103318 (cit. on pp. 5, 10, 14, 17, 28, 29).

Machicoane, N. and R. Volk (2021). "Transport of large particles through the transition to turbulence of a swirling flow." In: *Physical Review Fluids* 6.4, p. 044303 (cit. on p. 50).

Marmottant, P. and E. Villermaux (2004). "On spray formation." In: *Journal of fluid mechanics* 498, pp. 73–111 (cit. on pp. 2, 3, 8, 33, 35).

Marty, S., J.-P. Matas, and A. Cartellier (2013). "Study of a liquid–gas mixing layer: Shear instability and size of produced drops." In: *Comptes Rendus Mécanique* 341.1-2, pp. 26–34 (cit. on pp. 27, 33).

Masuk, A. U. M., A. Salibindla, and R. Ni (2019). "A robust virtual-camera 3D shape reconstruction of deforming bubbles/droplets with additional physical constraints." In: *International Journal of Multiphase Flow* 120, p. 103088 (cit. on p. 29).

Matas, J.-P. and A. Cartellier (2013). "Flapping instability of a liquid jet." In: *Comptes Rendus Mécanique* 341.1-2, pp. 35–43 (cit. on p. 27).

Matas, J.-P., A. Delon, and A. Cartellier (2018). "Shear instability of an axisymmetric air–water coaxial jet." In: *Journal of Fluid Mechanics* 843, pp. 575–600 (cit. on pp. 4, 8, 56).

Matas, J.-P., S. Marty, M. S. Dem, and A. Cartellier (2015). "Influence of gas turbulence on the instability of an air-water mixing layer." In: *Physical review letters* 115.7, p. 074501 (cit. on pp. 4, 5, 20, 56, 64).

Maurice, G, N. Machicoane, S Barre, and H Djeridi (2021). "Coupled x-ray high-speed imaging and pressure measurements in a cavitating backward facing step flow." In: *Physical Review Fluids* 6.4, p. 044311 (cit. on p. 58).

Maxey, M. R. (1987). "The motion of small spherical particles in a cellular flow field." In: *Physics of Fluids* 30.7, pp. 1915–1928 (cit. on p. 50).

Mayer, W. and R Branam (2004). "Atomization characteristics on the surface of a round liquid jet." In: *Experiments in fluids* 36.4, pp. 528–539 (cit. on pp. 3, 8).

Osuna-Orozco, R. (2021). "Characterization and Control of Electrostatically Assisted Two-Fluid Coaxial Atomization." PhD thesis. University of Washington (cit. on p. 7).

Osuna-Orozco, R., N. Machicoane, P. D. Huck, and A. Aliseda (2019). "Feedback control of coaxial atomization based on the spray liquid distribution." In: *Atomization and Sprays* 29.6, pp. 545–551 (cit. on pp. 7, 59).

— (2020). "Feedback control of the spray liquid distribution of electrostatically assisted coaxial atomization." In: *Atomization and Sprays* 30.1, pp. 1–9 (cit. on pp. 7, 59).

Osuna-Orozco, R., N. Machicoane, P. D. Huck, and A. Aliseda (2022). "Effect of electrostatic forcing on coaxial two-fluid atomization." In: *Physical Review Fluids* 7.7, p. 074301 (cit. on p. 7).

Owkes, M. and O. Desjardins (2014). "A computational framework for conservative, three-dimensional, unsplit, geometric transport with application to the volume-of-fluid (VOF) method." In: *Journal of Computational Physics* 270, pp. 587–612 (cit. on p. 6).

Pope, S. B. (2000). *Turbulent flows*. Cambridge university press (cit. on p. 61).

Powell, C. F., Y. Yue, R. Poola, and J. Wang (2000). "Time-resolved measurements of supersonic fuel sprays using synchrotron X-rays." In: *Journal of synchrotron radiation* 7.6, pp. 356–360 (cit. on p. 38).

Raynal, L. (1997). "Instabilité et entraînement à l'interface d'une couche de mélange liquide-gaz." PhD thesis. Grenoble 1 (cit. on p. 56).

Ricard, G., N. Machicoane, R. Osuna-Orozco, P. D. Huck, and A. Aliseda (2021). "Role of convective acceleration in the interfacial instability of liquid-gas coaxial jets." In: *Physical Review Fluids* 6.8, p. 084302 (cit. on pp. 4, 10, 27, 59).

Singh, G, K Jayanandan, A Kourmatzis, and A. Masri (2021). "Spray atomization and links to flame stability over a range of Weber numbers and pressure ratios." In: *Energy & Fuels* 35.19, pp. 16115–16127 (cit. on p. 10).

Singh, G, A Kourmatzis, A Gutteridge, and A. Masri (2020). "Instability growth and fragment formation in air assisted atomization." In: *Journal of Fluid Mechanics* 892 (cit. on pp. 2, 32).

Snow, J. T., M. Sato, and T. Tanaka (2015). "Droplet spray technique for particle removal." In: *Particle adhesion and removal*. John Wiley & Sons, pp. 313–335 (cit. on p. 2).

Tolfts, O. (2023). "Morphology, statistics, and time dynamics of the liquid jet breakup in coaxial two-fluid atomization." PhD thesis. Université Grenoble Alpes (cit. on pp. 45, 48).

Tolfts, O., G. Deplus, and N. Machicoane (2023). "Statistics and dynamics of a liquid jet under fragmentation by a gas jet." In: *Physical Review Fluids* 8.4, p. 044304 (cit. on pp. 10, 59).

Tomar, G., D. Fuster, S. Zaleski, and S. Popinet (2010). "Multiscale simulations of primary atomization." In: *Computers & Fluids* 39.10, pp. 1864–1874 (cit. on p. 6).

Torre, A. de la and J. Burguete (Aug. 2007). "Slow Dynamics in a Turbulent von Kármán Swirling Flow." In: *Physical Review Letters* 99.5, pp. 3–6 (cit. on p. 50).

Troitskaya, Y., A Kandaurov, O Ermakova, D Kozlov, D Sergeev, and S. Zilitinkevich (2017). "Bag-breakup fragmentation as the dominant mechanism of sea-spray production in high winds." In: *Scientific reports* 7.1, p. 1614 (cit. on p. 1).

Van Kampen, N. G. (1981). *Stochastic processes in physics and chemistry*. Elsevier (cit. on p. 50).

Varga, C. M., J. C. Lasheras, and E. J. Hopfinger (2003). "Initial breakup of a small-diameter liquid jet by a high-speed gas stream." In: *Journal of Fluid Mechanics* 497, pp. 405–434 (cit. on pp. 2, 4, 5, 8).

Veron, F. (2015). "Ocean spray." In: *Annual Review of Fluid Mechanics* 47, pp. 507–538 (cit. on p. 1).

Villermaux, E. (2007). "Fragmentation." In: *Annu. Rev. Fluid Mech.* 39, pp. 419–446 (cit. on p. 1).

Vu, L. (2022). "Multi-Scale Modeling and Control of Liquid-Gas Flows with a Focus on Spray Atomization." PhD thesis. Cornell University (cit. on p. 7).

Vu, L., N. Machicoane, D. Li, T. B. Morgan, T. J. Heindel, A. Aliseda, and O. Desjardins (2023). "A computational study of a two-fluid atomizing coaxial jet: Validation against experimental back-lit imaging and radiography and the influence of gas velocity and contact line model." In: *International Journal of Multiphase Flow* 167, p. 104520 (cit. on pp. 6, 7).

Wang, Y., K.-S. Im, and K. Fezzaa (2008). "Similarity between the primary and secondary air-assisted liquid jet breakup mechanisms." In: *Physical review letters* 100.15, p. 154502 (cit. on p. 38).

Weitkamp, T., D. Haas, D Wegrzynek, and A. Rack (2011). "ANKAphase: software for single-distance phase retrieval from inline X-ray phase-contrast radiographs." In: *Journal of synchrotron radiation* 18.4, pp. 617–629 (cit. on pp. 44, 45, 56).

Zandian, A, W. Sirignano, and F. Hussain (2019). "Vorticity dynamics in a spatially developing liquid jet inside a co-flowing gas." In: *Journal of Fluid Mechanics* 877, pp. 429–470 (cit. on p. 22).

Zandian, A., W. A. Sirignano, and F. Hussain (2018). "Understanding liquid-jet atomization cascades via vortex dynamics." In: *Journal of Fluid Mechanics* 843, pp. 293–354 (cit. on p. 22).

Zhao, H., H.-F. Liu, X.-S. Tian, J.-L. Xu, W.-F. Li, and K.-F. Lin (2014). "Influence of atomizer exit area ratio on the breakup morphology of coaxial air and round water jets." In: *AIChE Journal* 60.6, pp. 2335–2345 (cit. on pp. 10, 14).